Methods for plasma stabilization and control to improve antihydrogen production

by

Celeste Carruth

A dissertation submitted in partial satisfaction of the

requirements for the degree of

Doctor of Philosophy

in

Physics

in the

Graduate Division

of the

University of California, Berkeley

Committee in charge:

Professor Joel Fajans, Chair
Professor Jonathan Wurtele
Professor David Steigmann

Summer 2018

Methods for plasma stabilization and control to improve antihydrogen production

Abstract

Methods for plasma stabilization and control to improve antihydrogen production

by

Celeste Carruth

Doctor of Philosophy in Physics

University of California, Berkeley

Professor Joel Fajans, Chair

The ALPHA (Antihydrogen Laser Physics Apparatus) collaboration creates and performs precise measurements on antihydrogen to test Charge-Parity-Time (CPT) symmetry. Prior to creating antihydrogen we must prepare the antiproton and positron plasmas to have optimal and repeatable parameters. This thesis presents the development of a new method to simultaneously control the number of particles and plasma density of lepton plasmas, developments that increased our antihydrogen trapping rate, precision physics measurements performed on antihydrogen, and other plasma studies still under development. The method to stabilize the number of particles was based on a zero-temperature plasma model, which states that the plasma's on-axis self potential and density uniquely define a plasma. It is the combination of two previously existing techniques, radial compression in the Strong Drive Regime (SDR) with Evaporative Cooling (EVC), thus we called it SDREVC. Experimentally this method has proven to be very robust in delivering nearly identical plasmas, and theoretical calculations applying a finite temperature plasma model indicate that temperature effects in our operating regime are insignificant. The development took place in ALPHA's Penning-Malmberg traps, and consisted of designing and testing potential well shapes that allowed the compression and evaporation to occur simultaneously. The standard deviation in particle number of our initial load of positrons in 2016 was 24%, a fluctuation which was previously uncontrolled, but the standard deviation after SDREVC amounted to only 3%. After implementing SDREVC in our experimental routines, the stability made it possible to optimize plasma manipulations for antihydrogen production runs and increase our antihydrogen trapping rate by approximately a factor of 20. This increase in the trapping rate played a major role in our recent measurements of the hyperfine transition and 1S-2S spectroscopy of antihydrogen, and the 1S-2S spectroscopy measurement is now one of the most precise tests of CPT symmetry.

To my family: thank you for teaching me to ask questions and for continually encouraging me throughout my education.

Contents

List of Figures

Acknowledgments

I am really grateful to my advisor, Joel Fajans, who supported my research and gave me the opportunity to become a member of the ALPHA collaboration and spend nearly three years of my Ph.D. living in Switzerland while working at CERN. Thanks for encouraging me to speak up, giving me a solid research project, and always being quick to respond to my questions. Many thanks also to Jonathan Wurtele for his support in my research throughout my years at Berkeley and for continuing to make my plasma physics education a priority. I've greatly appreciated the guidance I received from both of them during my thesis research and their intensive involvement in editing the publication on the SDREVC method highlighted in this thesis.

I feel indebted to the entire ALPHA collaboration, and am fully aware that the success of this thesis research was made possible by the efforts of everyone who has helped design, build, and run the experiment. In particular I would like to thank Jeff Hangst, Will Bertsche and Niels Madsen for their leadership and organization of the experiment and personal support of my research: suggesting ideas, answering questions, and giving me time on the experiment to develop SDREVC. Tim Friesen, Chris Rasmussen, Dan Maxwell, Joseph McKenna, Chukman So, and Tim Tharp have taught me a lot regarding different aspects of the experiment and plasma calculation tools and I thank them for their patience and willingness to answer questions and teach me. I'm grateful to Matthias Reinsch who provided extensive help with writing the Mathematica code included in the appendix. I would also like to recognize and thank all those who are (or were) grad students alongside me during my Ph.D. studies for their encouragement and company. We stayed up grading Physics 111 lab reports together, discussed research opportunities and our goals, worked together to make the best routines to trap the most antihydrogen atoms, and spent many hours together on shifts. I wish to extend my gratitude to my undergraduate research and academic advisors at the University of Michigan, Myron Campbell and Jean Krisch, who encouraged me to choose to be a physicist. Finally, I would like to gratefully acknowledge the funding that enabled this research from the United States Department of Energy, Contract No. DE-FG02-06ER54904, and the National Science Foundation, Grant No. 1500538-PHY.

Chapter 1

Antihydrogen for Precision Physics Measurements

1.1 Antimatter: the missing half of the universe

The "big bang" theory describes the universe as having originated from a single point of energy, followed by rapid expansion while energy converted to mass according to Einstein's formula, $E = mc^2$. Charge-Parity-Time (CPT) symmetry requires that the conversion of energy to mass produce equal quantities of matter and antimatter, so we should observe that half of the mass in the universe is antimatter. It also requires the physical properties of antimatter, such as its charge and energy level transitions, to have the same magnitude as the properties of matter. The collision of a matter and antimatter particle results in their annihilation during which the mass converts back into energy. When electrons and positrons annihilate, gamma-rays are produced; when heavier particles annihilate, typically short-lived pions are produced which quickly decay into photons, leptons and neutrinos.

If there exists an antimatter galaxy somewhere in the universe, we expect to observe gamma-ray signals created by annihilations occurring at the boundary of the matter and antimatter, because even in the low density interstellar space there are still collisions between particles. The Alpha Magnetic Spectrometer (AMS) experiment [1] on the International Space Station detects positrons, electrons, and protons streaming from space, and specifically studies the energy spectrum of positrons. While it has found an excess of 10 GeV positrons unexplained by existing models of cosmic ray sources, the excess does not indicate a side of the universe filled with antimatter and is speculated to be caused by other sources or due to undiscovered causes. The AMS experiment [2] and the Bess-POLAR balloon experiment [3] also measured cosmic-ray antiprotons, but the number of antiprotons measured by both experiments were within the range expected from secondary sources (collisions of high-energy cosmic-ray particles with interstellar particles).

The missing antimatter indicates that a violation of CPT symmetry occurred during the conversion of energy to mass in the early stages of the universe. We call the unknown

violation process "baryogenesis," because the process preferred baryons (heavy particles including protons) over antibaryons (such as antiprotons). This is one of the biggest unsolved mysteries of cosmology and precise measurements of CPT symmetry are necessary to search for an explanation for baryogenesis.

The Antihydrogen Laser Physics Apparatus (ALPHA) collaboration at CERN performs precision measurements on antihydrogen to determine if its charge, spectroscopy, and in the future its gravitational acceleration are exactly the same as hydrogen's. These measurements tell us whether CPT symmetry correctly describes the properties of antihydrogen, and processes required to perform these measurements are the focus of this thesis.

1.2 Fundamental characteristics of antihydrogen

Antihydrogen consists of the antimatter version of particles that form hydrogen, namely an antiproton and a positron. An antiproton, being a baryon, consists of two up antiquarks and one down antiquark; a proton consists of two up quarks and one down quark. While both particles should have the same mass, one aspect of the "anti" label is that antiparticles have opposite charge of their matter counterparts: with e representing the magnitude of the charge of an electron, an up quark carries charge $+2/3e$ and an up antiquark carries charge $-2/3e$, while a down quark carries charge $-1/3e$ and a down antiquark carries charge $+1/3e$. Adding the charges gives a net charge of $-e$ for the antiproton and $+e$ for the proton. A positron carries the same mass as an electron but has charge $+e$, thus the net charge of hydrogen is zero and the net charge of antihydrogen should also be zero. Charge measurements of neutral matter atoms and molecules, including H_2, show a charge of 0 to the level of 10^{-21} [4]. The ALPHA collaboration measured the charge of antihydrogen and set an upper limit of $Q < 25 \times 10^{-9}e$, where e is the charge of an electron [5].

While positrons occur naturally as a byproduct of β^+ decays of radioactive elements, antiprotons have to be manufactured artificially. Currently the only way to artificially make antiprotons is to accelerate a proton beam to several GeV and collide it into a target, releasing energy that then forms pairs of protons and antiprotons along with other pairs of particles and antiparticles.

1.3 CPT symmetry and Antimatter

Our physical universe embodies many symmetrical properties. Symmetry can be expressed as a mirror of a particular parameter: the symmetrical portion appears identical in magnitude but may be reversed in orientation. The study of antimatter is necessary to test symmetry theories, specifically the theory of charge-parity-time (CPT) symmetry. Charge-parity-time symmetry states that if you reverse the charge of an antimatter particle, flip its left/right orientation and look at it going backwards in time, it will appear the same as a matter

particle. This is depicted by a lego woman in Figs. 1.1a-1.1e; we'll call the matter version of her Linda.

Antilinda goes up the stairs and carries her bag in her right hand; black clothes represent negative charge. Linda goes down the stairs and is carrying her bag in her left hand; white clothes represent positive charge. Following a charge conjugation event, shown in Fig. 1.1c, the black clothes change to white, but all other parameters remain the same. Following a parity transformation, Antilinda holds her bag in her left hand. Finishing with a time reversal in Fig. 1.1e, Antilinda is found to be wearing white clothes, going down the stairs, and carrying her briefcase in her left hand. Now she is in all measurable aspects identical to Linda.

The parity symmetry between matter and antimatter means that a person living in an antimatter galaxy, like Antilinda, could perform physics experiments and observe left and right-handed events being switched. Richard Feynman [6] told a story of how to communicate what "left" and "right" mean to an alien: tell him to make a physics experiment consisting of a solenoid around a piece of cold cobalt and explains that if the magnetic field points up and the emitted radiation travels down, the direction the current flows through the coil is called " right." However, an anticobalt atom would produce a positron in a decay, and the positron would go in the opposite direction, or "left." Feynman finished up the story by warning that if you agreed to meet and shake right hands but the martian (or Antilinda) puts out her left hand, as depicted in Fig. 1.2, she's made of antimatter and if you shake hands you'll be annihilated.

1.4 The Weak Equivalence Principle: precision antimatter gravitational physics

In addition to studying CPT symmetry, it is also important to test the Weak Equivalence Principle (WEP) from Einstein's theory of General Relativity [7] with antimatter, since it predicts that matter and antimatter should gravitate in the same way. Given that the gravitational force dominates over long distances in our universe, a difference in antimatter's gravitational behavior could explain why we don't observe it. If they repel or have different acceleration rates, there could be a difference in the annihilations we expect to see at the boundary between matter and antimatter. While the recent discovery of gravitational waves originating from the coalescing of two black holes by the LIGO and VIRGO collaborations [8] is a remarkable test of general relativity, it remains to be determined if matter and antimatter gravitate towards each other.

References [9, 10] and other papers argue that measurements of matter in earth's gravitational field set precise limits to antimatter's gravitational behavior in lieu of a directly measuring antimatter's sign and magnitude of acceleration in earth's magnetic field. However, other articles [11, 12] point out that such theories include assumptions about equivalent properties of matter and antimatter (aside from its gravitational behavior) which have not

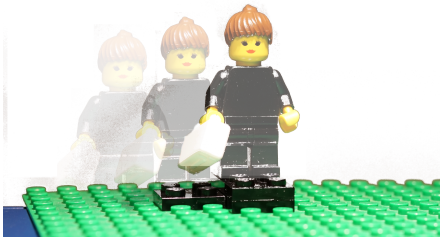

(a) Antilinda

(b) Linda

(c) Antilinda undergoes a charge transformation: she wears white clothes.

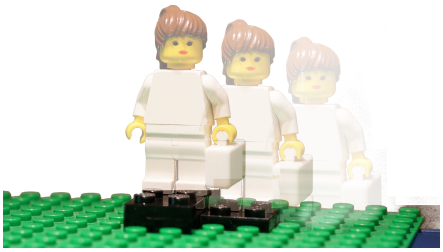

(d) Antilinda then has a parity transformation: she now holds the bag in her left hand.

(e) Antilinda then experiences time reversal: she now goes down the stairs and appears identical to Linda.

Figure 1.1: CPT transformations illustrated with legos

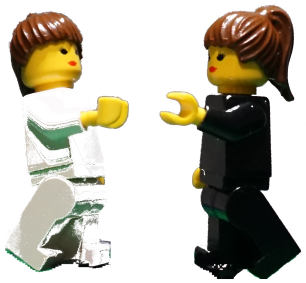

Figure 1.2: Linda and Antilinda agreed to shake "right" hands.

yet been confirmed, and a direct measurement is necessary.

Measurements of earth's gravitational pull on charged particles is practically impossible due to their acceleration in electric or magnetic fields, thus a precise measurement can only be performed on a neutral antimatter atom. It is impossible to perform an accurate and precise measurement in the horizontal ALPHA trap because the atoms, once released from the trap, annihilate against the wall of the trap before any noticeable gravitational effects can occur, and the azimuthal distribution of annihilations appears practically symmetric about the axis. The ALPHA collaboration determined that the ratio of antimatter's gravitational mass to its inertial mass must be less than 110 [13] by analyzing the vertical distribution of annihilation events, but this is a very rough measurement compared to the expected value of 1. The ALPHA collaboration is currently building a new experiment, ALPHAg, motivated by theory [14]. This new experiment will have a vertical antihydrogen trap that will enable us to measure the sign of the gravitational motion and place an upper bound on its acceleration, possibly before the end of this year. At the Antiproton Decelerator (AD) facility at CERN, the GBAR and AeGIS collaborations are also preparing different experiments to measure the sign and magnitude of antihydrogen's gravitational acceleration.

1.5 History of positrons and antiprotons, the antiproton decelerator, and current research developments

The existence of a particle with opposite charge of the electron was first predicted by Paul Dirac in 1928 [15]. In 1933 Carl Anderson observed a cosmic ray particle with the opposite charge of an electron but the same order of magnitude of mass of an electron in a vertical Wilson cloud chamber in a 1.5 Tesla field [16]. This discovery was made by observing photographic tracks of cosmic ray particles traveling through lead plates: a few tracks showed a particle with equal mass to an electron but curved in the opposite direction; this particle

was called a “positive electron,” a name shortened to “positron." An example image from the discovery is shown in Fig. 1.3a. Low-energy electron-positron annihilations result in 511 keV gamma rays traveling in opposite directions that conserve momentum. High-energy annihilations in the range of 2-20 GeV can produce mesons and hadrons [17, 18] and very high energy annihilations with center of mass energies around 90 GeV have produced the Z boson [19].

In addition to their role in physics experiments, positrons are now used widely in the medical field. The discovery of how to artificially create positron-emitting radioactive elements in 1934 [20], the development of a circular detector to track annihilations [21], and the application of computational tomography [22] led to the development of Positron Emission Tomography (PET) [23]. PET scans are widely used as a medical procedure to search for cancer, heart problems, or brain disorders. Positron annihilations with electrons produce back-to-back gamma rays, which are detected by a circular gamma ray detector that surrounds a cross-section of a person's body. The signals in the detector are then reconstructed to show the tomography of the activity [24]. This procedure requires positrons to be emitted from inside the body; this is accomplished by tagging glucose molecules with a radioactive isotope and inserting it into a patient's bloodstream. The isotope continually emits positrons while the person's body consumes the tagged glucose, and the circular detector measures the location and intensity of positron annihilations along a cross-section of the body. A series of cross-sectional measurements are then analyzed to produce a 3D image. Locally high glucose consumption, as detected by a region with high positron emission, is a sign of potential cancer or other abnormal physical condition.

The antiproton was first observed at the Bevatron accelerator by Segrè, Chamberlain, Wiegand, and Ypsilantis at the Radiation Laboratory at the University of California-Berkeley in 1955. The Bevatron was specifically designed to produce energies at the BeV (now referred to as GeV) level required to produce proton-antiproton pairs. By deflecting the beam of particles with magnets and changing the magnetic field, they performed the first measurement of the proton to antiproton mass ratio [25], and the next year the collaboration captured an antiproton annihilation event in a photographic emulsion, shown in Fig. 1.3b. In the figure, track "L" is the antiproton, "e" is a proton, "a" and "b" are pions, and the other tracks are likely either protons or α-particles [26].

From 1985-2011, the Tevatron synchrotron at Fermilab created an antiproton beam from a high-energy proton beam, and then simultaneously accelerated proton and antiproton beams to a center of mass energy of 1.6 TeV. The annihilation energy was sufficient to produce heavier particles than were possible to create at previous facilities. The highlight of the research program was the discovery of the top quark, for which candidate events were found in 1994 by the Collider Detector at Fermilab (CDF) collaboration [27] and a formal discovery at the $4.6 - 4.8\sigma$ level was announced in 1995 by the CDF and D0 collaborations [28, 29]. The Tevatron with its antiproton beam stopped operating in 2011, around the same time the larger and more powerful Large Hadron Collider (LHC) turned on at CERN; by 2015 the LHC was colliding proton beams with a center of mass energy of 13 TeV [30].

The Low Energy Antiproton Ring (LEAR) facility at CERN produced antiprotons from

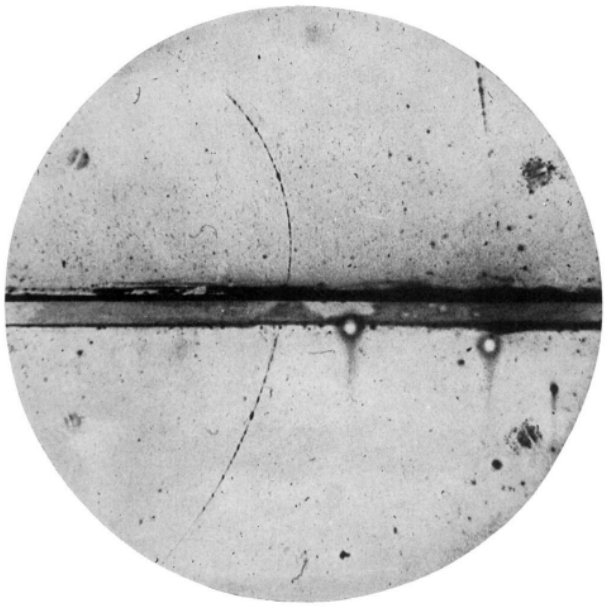

(a) A positron track that lead to its discovery. Figure from reference [16].

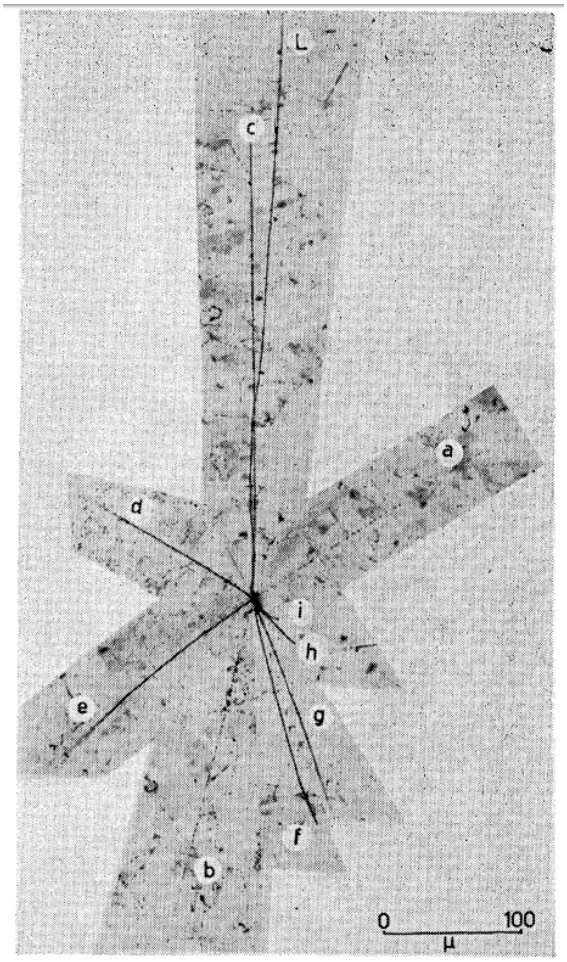

(b) Antiproton star-shaped annihilation captured in emulsion. Figure from reference [26].

Figure 1.3: Images from the discoveries of positrons and antiprotons

1982 to 1996 [31], and was home to the first antihydrogen atoms produced [32]. LEAR was followed by the Antiproton Decelerator at CERN, which turned on in 2000 and is currently the only operating facility that produces beams of cold antiprotons. The Facility for Antiproton and Ion Research in Europe (FAIR) in Germany is expected to be completed in a few years and is designed to produce a beam of antiprotons with energies of 1-15 GeV and other high energy ion beams [33].

Electron sources for plasmas

While there are multiple technologies to produce large numbers of electrons for plasmas, in ALPHA we use a thermionic electron gun inside the vacuum. In ALPHA, the electron guns contain a thin filament that heats up a metal plate in front of it, and electrons in the plate can gain enough kinetic energy to overcome the work function of the surface and escape into the vacuum. In ALPHA, the electron beam follows magnetic field lines down the beamline and into a potential well in the Penning trap. Ideally an electron gun is perfectly aligned along the beamline axis and is inside the same magnetic field as the trap, because a change in the alignment of the electron gun and the magnetic field axis by a couple of millimeters can dramatically affect the number of electrons loaded into the Penning trap. However, in ALPHA the electron guns are mounted on vertically moving sticks, and slight variations in electron gun position are likely contributing to variations in the number of particles loaded shown in chapter 4.

Another method for producing electrons for plasmas is to use a light source and photocathode to produce an electron plasma; this method has the advantage of allowing the user to make a plasma with a particular 2D cross-sectional shape, and was previously used in the Berkeley lab for plasma vortex studies [34]. An electron beam can also be created by a plasma-cathode source. Instead of using a filament, a hollow cathode inside of an axial magnetic field is used to ionize a gas into a plasma, and electrons from the surface of the plasma can be accelerated into a beam; this is used for industrial applications such as electron beam welding [35]. The ionization gas is optimal for atmospheric pressure plasmas and won't work in UHV conditions, and the photocathode method requires both a light source and photocathode to be aligned along the magnetic field axis. Electron guns are physically compact, UHV-compatible, and straightforward to control, so they are used in ALPHA and many other Penning-trap experiments.

Positron sources for plasmas

Positron plasmas require a radioactive source or a source of high-energy particles. ALPHA and other similar experiments (see Refs. [36, 37] and [38]) use a radioactive Na-22 source that emits positrons through β^+ decays at a peak rate of 75 mCi. The GBAR experiment under construction at CERN includes in its design a linear electron accelerator to produce positrons by the interaction of a 10 MeV electron beam and a thin tungsten foil [39]. The APEX experiment under development in Germany, which is preparing to study electron-

positron pair plasmas, uses a positron beam generated at the Neutron Enduced Positron source Munich (NEPOMUC) [40]. NEPOMUC produces a high flux of positrons, $10^9\,\mathrm{s}^{-1}$, through the thermal interactions of neutrons coming from nuclear reactions and platinum foils [41]. Lasers with an intensity around $10^{20}\,\mathrm{W/cm}^2$ interacting with thin metal foils can also create positron at a rate of 2×10^{10} positrons per pulse [42], but laser positron sources are an emerging field and not yet applied to Penning-trap experiments.

Advantages of β^+ radioactive sources are the smaller size and cost relative to an accelerator, nuclear reactor, or ultraintense laser. Na-22 has a half-life of 2.6 years; the source can be used for a few half-lives and still produce a few million trappable positrons in 100-150s, which is sufficient for our current antihydrogen production method. The main advantage of the accelerator source GBAR will use and the neutron-induced source for APEX's positrons is that a monoenergetic beam of positrons can be produced at a rate that is orders of magnitude greater than the rate we collect from Na-22, although the facilities are much more expensive and complicated to implement. Additionally, the shielding around GBAR's accelerator requires a lot more space in the antiproton facility than the $\approx 1\,\mathrm{m}^3$ occupied by the radioactive sodium salt and its shielding.

The Antiproton Decelerator and operations at CERN

The Antiproton Decelerator functions in many ways the opposite of the Large Hadron Collider: it slows down antiprotons instead of accelerating and colliding protons or ions. The circumference of the LHC is 26.7 kilometers and it crosses the French-Swiss border, while the AD has a circumference of 182 meters and fits inside one building inside the French border of the Meyrin site at CERN. A schematic of CERN's facilities is shown in Fig. 1.4. The LHC's proton beams and the AD's antiproton beam begin when atoms are extracted from a bottle of hydrogen gas. The hydrogen gas is ionized and the protons are collected into a beam and accelerated in the Linear Accelerator 2, then sent to the Proton Synchrotron Booster and after that the Proton Synchrotron (PS) [43, 44]. From there the protons diverge, and the beam headed for the LHC is accelerated to 450 GeV in the Super Proton Synchrotron and finally in the LHC [45]. Protons for the AD's antiproton beam are extracted from the PS at 26 GeV approximately every 120s and dumped onto an iridium target in an underground beamline next to the AD. Each year CERN's schedule has a season of experimental operation, from late spring through late fall, followed by a "year-end shutdown" for repairs and upgrades; during the operational season when the accelerators and AD are running, the facilities operate 24 hours a day and 7 days a week. Every few years CERN has a scheduled long shutdown for one or two years during which the particle accelerators and the AD are turned off in order to replace and upgrade different components. The next scheduled long shutdown will last from 2019-2020, so the measurements performed this year will be the last measurements performed on antihydrogen until 2021.

The energy released by 26 GeV protons colliding with stationary protons in the target is

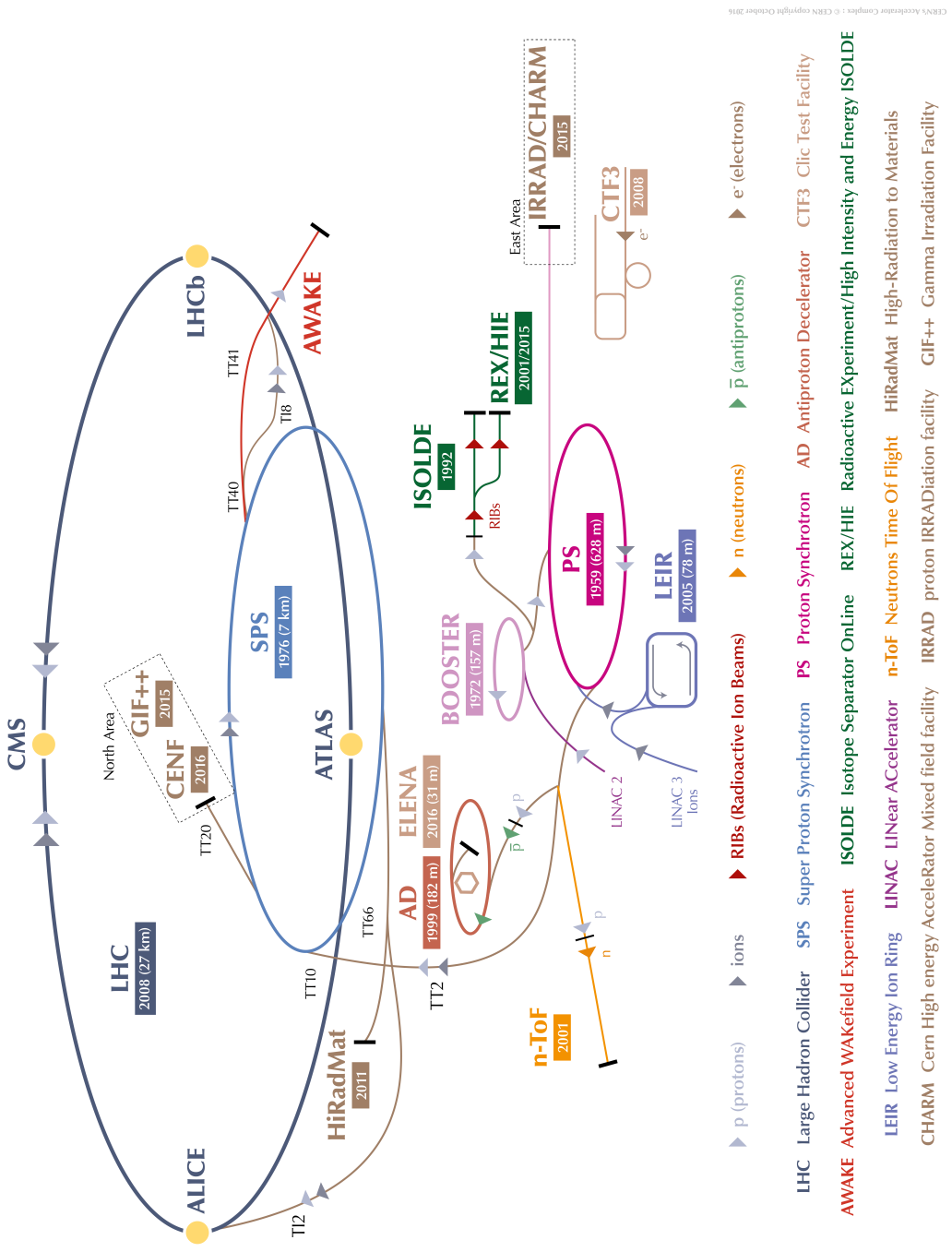

Figure 1.4: CERN's accelerator complex showing relative locations of the facilities (not drawn to scale). Figure from reference [46].

high enough to produce, among many other particles, antiproton-proton pairs.

$$p^+ + p^+ => p^+ + p^- + p^+ + p^+, \tag{1.1}$$

The antiprotons are magnetically separated from the other particles and sent to the antiproton decelerator, which slows them down from 3.57 GeV to 5 MeV. Even at 5 MeV the antiprotons are still moving at 10% the speed of light:

$$\beta = \sqrt{1 - \left(\frac{1}{\gamma}\right)^2} \tag{1.2}$$

$$= \sqrt{1 - \left(\frac{938}{5 + 938}\right)^2} \tag{1.3}$$

$$= 0.1 \times c. \tag{1.4}$$

ELENA: Extra Low ENergy Antiprotons

ELENA is a second-stage antiproton decelerator 10 m in diameter currently being installed and commissioned in the AD hall at CERN [47]. It is designed to slow the 5.3 MeV antiproton beam down to 100 keV, and it is predicted that ALPHA will be able to trap 100 times more antiprotons from the slower beam. An additional feature of ELENA is that it will be able to deliver antiprotons to all AD experiments in parallel, so that instead of having an 8-hour shift of antiprotons and not receiving antiprotons for some weeks of the year, they will be delivered continuously 24 hours a day every day. ELENA is projected to come online in 2021 after the next long shutdown.

Catching antiprotons

To further slow down the antiprotons, the beam is sent through a thin beryllium foil which moderates the beam, slowing down the particles. We trap the antiprotons in a prepared cold electron plasma in a 4.5 kV deep potential well shown in Fig. 2.11 by applying one potential barrier (the red dash-dot line) to block the antiproton beam, and just after the antiprotons arrive we quickly bring down the other barrier to create the well that traps the antiprotons (the solid orange line in the figure). The antiproton bunch will enter the one-sided potential well, bounce against the barrier on the far side, and be trapped when the second barrier (the "gate" potential) is lowered. The electrons cool the antiprotons by several orders of magnitude by coming into thermal equilibrium through repulsive coulomb collisions [48]. A full discussion of the cooling mechanisms is given in Chap. 3.

While the moderated beam energy is much lower than 5 MeV, it is still much greater than the 4.5 kV trapping well depth. The high energy of the incoming beam means most antiprotons that are created are impossible to trap; of the 50×10^6 antiprotons in the AD beam, we trap and cool approximately 10^5, an efficiency of 0.2%. To increase the efficiency

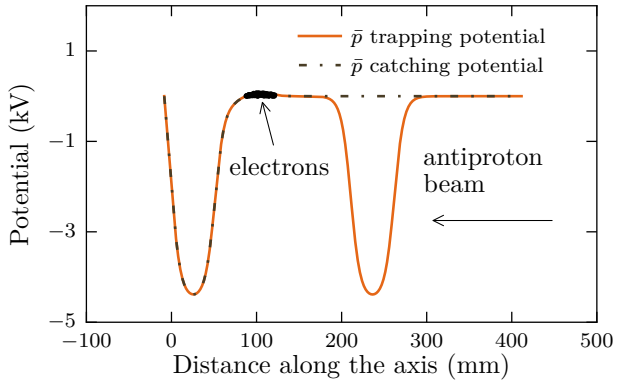

Figure 1.5: Potential well used to catch antiprotons. The brown dash-dot line shows the potential at the moment the antiprotons arrive, and the orange solid line shows the potential well that traps the antiprotons. During this process the electrons stay trapped in the slight bump in the well indicated on the figure.

by one or two orders of magnitude, we would need a lower energy beam (like we will have when ELENA is operational), or we would need to increase the potential well depth. One of the main challenges of increasing the well depth is the speed required to close the gate potential, since the amplifier driving the gate potential needs to ramp up to several kV in a very short amount of time.

Estimated cost of antiprotons and the scale of current production levels

Antiproton production is a highly inefficient process, and antimatter has been classified as the most expensive material on earth. For the sake of curiosity, using the given data from the AD we can calculate the cost per gram of antiprotons in the beams that cycle the AD. The AD reports that 1.5×10^{13} protons with momentum 26 GeV/c yield a bunch of 50×10^6 antiprotons for the AD [49]. The energy equivalence of the mass of an antiproton is 0.948 GeV, and the initial energy is $p^2c^2 = 26$ GeV, so each proton gains 25.08 GeV or 0.4×10^{-8} J in the acceleration process. This means a bunch of protons gains a total of 60 kJ=$0.01\bar{6}$ kWh per bunch.

Even in the impossible scenario that the acceleration process is 100% efficient, using the rate of 0.1477 Swiss franc (CHF) per kWh [50], the energy cost per gram of antiprotons is:

$$\frac{0.01666 \text{ kWh}}{8.3 \times 10^{-17} \text{ grams}} = 2 \times 10^{14} \text{ kWh} \tag{1.5}$$

$$2 \times 10^{14} \times 0.1477 \text{ CHF} = 2.95 \times 10^{13} \tag{1.6}$$

$$= 29.5 \text{ trillion CHF/gram.} \tag{1.7}$$

This calculation clearly does not take into account the inefficiencies in energy consumed to accelerate and then decelerate antiprotons, and significant construction and peripheral operating costs, including manpower requirements of the facilities. Note also that this is only 0.2% of the the cost per gram of trapped antiprotons given our current trapping rate.

The AD produces roughly 150,000 bunches of antiprotons a year, counting the rate of one bunch per slightly less than two minutes, with 24/7 operation lasting about 200 days of the year. Thus each year 7.5×10^{12} antiprotons cycle around the AD, amounting to 1.25×10^{-11} grams per year. A concerned science-fiction educated visitor at the AD who wonders what level of destruction would happen if the antimatter went missing can be assured that the energy equivalent of a year's supply of antiprotons produced, 1.1 kJ, is much less than the 74 kJ required to boil a cup of water. While the energy equivalence of this small amount of antimatter produced would only cost a few hundred CHF per year, due to the inefficiencies of the deceleration process and the cost salaries for the operators, the annual operating costs for the AD and incoming proton beam are expected to be in the tens of millions of CHF.

As seen from these calculations, the proposed application to use antiprotons as fuel for inter-stellar space travel [51] is still science fiction. The current prohibitive cost per gram, limitation in production rates, and the physical limitations in trapping macroscopic quantities of charged particles due to the Brillouin density limit (see Sec. 3.3) mean antiproton production and trapping facilities would need to be scaled up by several orders of magnitude.

Recent precision measurements with antiprotons by other collaborations

The Baryon Antibaryon Symmetry Experiment (BASE) collaboration at the AD is solely focused on antiproton measurements. Using a small cold Penning trap with a volume of 1.2L, the collaboration succeeded in trapping antiprotons while performing measurements on them for more than a year [52]. While most antimatter measurements are done destructively, with the annihilation providing information about the measurement, the BASE collaboration relies on highly sensitive image current detection performed by superconducting circuits that can both drive the particles and detect their image currents. The collaboration recently announced highly precise measurements of the g-factor of antiprotons at the level of 0.8 parts per million [53] and the magnetic moment of the antiproton, $\mu_{\bar{p}}$, at 1.5 parts per billion [54].

The Atomic Spectroscopy And Collisions Using Slow Antiprotons (ASACUSA) collaboration has also used antiprotons to make antiprotonic helium. This was accomplished by condensing ^{4}He gas to cryocooled walls at 1.3K, and colliding the antiproton beam with helium atoms that evaporated from the supercooled liquid. Spectroscopy was performed on approximately 2 billion short-lived $\bar{p}\mathrm{He}^+$ molecules to measure the antiproton-to-electron mass ratio to a precision of 0.8 parts per billion [55].

1.6 History of antihydrogen production

Antihydrogen was first produced by the PS210 collaboration at LEAR in 1995; a total of 11 atoms were observed [32]. In this milestone experiment, a 2 GeV antiproton beam was sent through a thin Xe-cluster target. With some small probability, an antiproton passing through the Coulomb field of a charge can create an electron-positron pair, then bond with the positron to form antihydrogen:

$$\bar{p}Z \rightarrow \bar{p}\gamma\gamma Z \rightarrow \bar{p}e^{+}e^{-}Z \rightarrow \bar{H}^{0}e^{-}Z, \tag{1.8}$$

however the positron must be moving at close to the velocity of the antiproton, as the relative energy must be equal or less than the 13.6 eV binding energy [32]. The next year, a few relativistic antihydrogen atoms were created in the E866 experiment at Fermilab by colliding an antiproton beam with a hydrogen gas jet target [56], but no further antihydrogen developments were reported by that collaboration.

In 1996, LEAR was repurposed as the Low Energy Ion Ring at CERN. To continue the antiproton physics program at CERN, the Antiproton Decelerator was built and started operating in 2000, and provided much colder antiprotons with energies of 5.3 MeV. The ATHENA collaboration reported the creation of the first cold antihydrogen [57] in 2002, as did the ATRAP collaboration a few weeks later [58]. Some members of the ATHENA collaboration later formed the ALPHA and AEgIS collaborations at CERN. In 2010, the ALPHA collaboration trapped antihydrogen atoms for the first time [59] and demonstrated longer trapping times of up to 1000s in 2010 [60]. While the ALPHA and ATRAP collaborations are focused on trapping antimatter and then performing measurements on it, the ASACUSA and AEgIS collaborations plan to do experiments on antihydrogen beams. The ASACUSA collaboration reported in 2014 that they detected 80 atoms from a beam at a distance of 2.7 m from the production region [61], and in AEgIS, antihydrogen production is still under development.

1.7 Summary of ALPHA's trapping procedure

Trappable antihydrogen is formed by mixing cold positrons with cold antiprotons. Antihydrogen atoms that are created with temperatures below 0.54 K are trapped in a magnetic trap, but the majority of atoms are too warm to be trapped and annihilate almost instantly on the walls of the trap. Each trapping cycle creates tens of thousands of atoms while typically only 15-20 are trapped. Once trapped, though, the atoms have a lifetime of approximately 60 hours [62], during which we can conduct experiments. Important fundamental studies the ALPHA collaboration has recently performed on antihydrogen include measuring its charge [5], the 1S-2S transition [62] and lineshape [63], and the hyperfine spectrum [64].

Spectroscopy experiments on matter are normally performed on at least tens of thousands of atoms at a time and rely on an emission or absorption signal from the cloud of atoms. The comparatively small number of antimatter atoms we trap means the emission or absorption

signal would be too small to measure precisely. Instead, we detect the signals resulting from annihilations of antihydrogen atoms with atom on the wall of the trap. The annihilation of the antiproton in an antihydrogen atom with a proton or neutron in a matter atom generally produces 2-5 charged pions. The pion trajectories are tracked in the silicon vertex detector used in ALPHA; this will be discussed in more detail in Chapter 2. We run experiments where we test if an applied electric field or electromagnetic radiation interacts with atoms, with the experiment designed such that an interaction causes the atom to escape the magnetic trap and annihilate on the wall. If antihydrogen interacts with a laser or microwaves at a particular frequency, we observe the strength of the interaction by counting the number of antihydrogen atoms that annihilate during the laser or microwave exposure.

In the ALPHA trapping scheme, the positrons outnumber the antiprotons by a ratio of about 30:1. Previously in the ALPHA experiment, the number of positrons varied on the order of a factor of two due to various fluctuations, and this impeded our trapping development and ability to maintain consistent trapping rates. This thesis reports on a new plasma development called SDREVC [65] that enables us to precisely produce a particular number of particles at a particular density from a plasma with varying initial conditions, with the only requirement that the initial plasma have more particles than we need. So, if we want to use three million positrons, we can load any number greater than around 3.3 million and apply this technique to produce a plasma with three million positrons.

After reducing fluctuations in the number of positrons from 24% in the initial load to around 4% after applying SDREVC, we proceeded with a new line of trapping development. This development was motivated by simulations that indicated a linear ramp of potential wells would inject more and colder antiprotons into the positron plasma than we had been achieving with autoresonant injection [66]. We increased our trapping rate by more than a factor of ten, which made it possible to perform the hyperfine study (a measurement that inherently requires many atoms to be in the trap) and achieved a much higher precision 1S-2S spectroscopy measurement than would have been possible at the previously low trapping rate.

1.8 Organization of this thesis

The collaborative nature of the work discussed in this thesis means the author had a prominent role in some developments and a contributing but less responsible role in other developments. The 24-hour operation of the experiment means work is divided into shifts, and a project started by one group of people is often continued by the next group, with each week's work coordinated daily by the run coordinator. From 2015-2018 the author usually worked three to five 8-hour shifts a week except when absent for conferences or other travel and also served as run coordinator for several weeks. The main focus of this thesis, the SDREVC method, was the author's own individual project. The author played a substantial role in the subsequent studies to improve antihydrogen production rates (section 5.1) and develop antihydrogen accumulation (section 5.3), but notes that these were collaborative efforts and

development was continued from one set of shift workers to the next. The author contributed to shifts for the other physics results cited. during part of the 2014 run prior to the charge measurement (section 5.8), and was directly involved in operating the experiment during the 1S-2S spectroscopy (section 5.10) and hyperfine spectroscopy (section 5.9) measurements.

This thesis reports on the hardware and general operational procedures for running the experiment in chapter 2, discusses non-neutral plasma theory that motivated the SDREVC method in chapter 3, and then presents the results of SDREVC in chapter 4. Other plasma studies and a discussion of the precision antihydrogen measurements are presented in chapter 5, followed by the conclusion of this thesis in chapter 6.

Chapter 2

Trapping Antihydrogen: trap hardware, procedures, and diagnostics

2.1 Trapping antihydrogen: general requirements and procedures

Synthesizing antihydrogen

Antihydrogen formation from positron and antiproton plasmas can occur via two mechanisms: radiative recombination (RR) and collisional three body recombination (TBR). In radiative recombination, an antiproton and positron combine and emit a photon that carries away the excess energy:

$$\bar{p} + e^+ \rightarrow \bar{\mathrm{H}} + h\nu. \tag{2.1}$$

This is calculated to have a recombination rate per trapped antiproton in a plasma of density n_{e^+} and temperature T [67]:

$$\Gamma_1 = 3 \times 10^{-11} \left(\frac{4.2}{T(\mathrm{K})} \right)^{1/2} \frac{n_{e^+}}{\mathrm{cm}^3} \frac{1}{s}. \tag{2.2}$$

In three body collisional recombination, two positrons collide with an antiproton at the same time and one of the positrons bonds with the antiproton to form antihydrogen while the other positron carries away the extra energy:

$$\bar{p} + e^+ + e^+ \rightarrow \bar{\mathrm{H}} + e^+. \tag{2.3}$$

TBR was calculated to have a recombination rate scaling as $T^{-4.5}$ [67, 68] for an infinite, unmagnetized plasma:

$$\Gamma_{coll} = 6 \times 10^{-12} \left(\frac{4.2}{T} \right)^{9/2} n_{e^+}^2 \, s^{-1}. \tag{2.4}$$

Three-body combination is expected to dominate the total recombination rate. For typical values $n_{e^+} = 2.5 \times 10^8\,\mathrm{cm}^{-3}$, $N_{\bar{p}} = 10^5$, and $T_{e^+} = 15\,\mathrm{K}$, $\Gamma_{RR}N_{\bar{p}} \approx 400\,\mathrm{s}^{-1}$ and $\Gamma_{TBR}N_{\bar{p}} \approx 1.2 \times 10^8\,\mathrm{s}^{-1}$, so $\Gamma_{TBR} \gg \Gamma_{RR}$. However, measurements of the recombination rate in the ATHENA trap showed the rate scaling as $T_{e^+}^{-0.7\pm0.2}$ [69], which appears much closer to the scaling calculated for RR. However, the absolute rate, 432 Hz, was much higher than the 40 Hz predicted for radiative recombination [69]. There is no analytical formula for the TBR rate in a finite length magnetized plasma, although calculations of a magnetized plasma [70] show that the TBR rate is an order of magnitude lower for a magnetized plasma than for an unmagnetized plasma. Note also that a measured recombination rate is most likely lower than the true recombination rate due to the possibility of antihydrogen atoms being created in high energy states and being reionized before they annihilate. Thus equations 2.2 and 2.4 are useful for showing the expected dominance of TBR over RR in antihydrogen synthesis but do not predict the measured synthesis rates because of the assumptions. Simulations of plasma conditions for specific trap geometry, as in Ref. [71] and [72], are the best way to calculate recombination rates. Further details on the theory of cold antihydrogen synthesis are given in Ref. [73].

A third method for creating antihydrogen relies on mixing antiprotons with positronium. The nanosecond lifetime of positronium means that it is necessary to create positronium *in situ*. The GBAR experiment proposes to make $\bar{\mathrm{H}}$ and $\bar{\mathrm{H}}^+$ ions by cooling positrons down to a few 10s of Kelvin and quickly injecting them onto a hollow tube made of mesoporous silica to form ortho-positronium with a goal of forming 10^{10} positronium in a $0.01\mathrm{cm}^3$ tube, exciting them via a laser to the 3D state, and sending the antiproton beam to the excited positronium cloud [39] and trap the resulting $\bar{\mathrm{H}}^+$ ions.

Thermal limit of trapping antihydrogen

Developing techniques to make antihydrogen took several years, and, as mentioned before, in 2010 the ALPHA collaboration succeeded in trapping antihydrogen for the first time [59]. While electrically neutral and thus insensitive to electric potential wells and barriers, antihydrogen can be trapped in a magnetic minimum Ioffe trap if the atoms are sufficiently cold and the trap is in an ultra-high vacuum (UHV). In ALPHA, a magnetic minimum trap is formed by radially confining fields of an octupole magnet and axially confining fields of mirror magnets. The magnetic field configuration has a trap depth of 0.8 T on top of a base field of 1T. Antihydrogen atoms are trapped if their kinetic energy is less than the potential energy barrier of the magnetic trap (the difference in potential energy from the confining wall of the trap to the base of the trap at 1T).

The potential energy of antihydrogen's magnetic dipole moment in a magnetic field is

$$U = -\mu_{\bar{\mathbf{H}}} \cdot \mathbf{B} \tag{2.5}$$

where $\mu_{\bar{H}} = -m_J g_J \mu_B$; m_J is the magnetic quantum number, g_J is the Landé g-factor, and μ_B is the Bohr magnetron. $\mathbf{J}$ is the total angular momentum and is the sum of the sum of

the orbital angular momentum $\mathbf{L}$ and the spin angular momentum $\mathbf{S}$.

Antihydrogen atoms are created in a large range of Rydberg energy levels but quickly decay to the ground state, where $\mathbf{L} = 0$. In the ground state, $S = \pm\frac{\hbar}{2}$, and the spin magnetic moment of particle i is defined as $\mu_{S_i} = -g_i\frac{q_i}{2m_i}\mathbf{S}$, with $g_{\bar{p}} \approx 5.6$ [54] and $g_e \approx 2$ [74]. The large mass difference between positrons and antiprotons means $\mu_{\bar{H}} \approx \mu_{S_{e^+}}$. The split of an atom's energy level based on the relative orientation of the spins of the antiproton and positron is referred to as hyperfine splitting, and a high precision measurement of this phenomenon in antihydrogen was recently performed by the ALPHA collaboration [64] and is discussed in Chap. 5. Inserting $S = \pm\frac{\hbar}{2}$, corresponding to the positron spin aligning or anti-aligning with the magnetic field, and $g_{e^+} \approx 2$ into the equation for the magnetic moment, we find that $\mu_{\bar{H}} = \mp\mu_B$. Thus the trap depth for antihydrogen is $U = \mp\mu_B B$, or in units of Kelvin and Tesla, $U(\mathrm{K}) = 0.67\Delta B(\mathrm{T})$.

The maximum velocity of a trapped antihydrogen atom can be calculated by equating a maximum kinetic energy to the potential well depth of the trap. For a trap depth of 0.8 Tesla, the maximum temperature of trapped atoms is 0.54K, or 4.66×10^{-5} eV. Equating this to $\frac{1}{2}(938 \times 10^6)\frac{v^2}{c^2}$, we find $\frac{v}{c} = 3 \times 10^{-7}$ so $v = 90\frac{\mathrm{m}}{\mathrm{s}}$. In a standard Penning trap a meter long with electrode radii less than 2 cm, an atom in the middle of the trap will annihilate against the wall within a few milliseconds of the trap magnets turning off.

Given that the antihydrogen trapping rate depends on the temperature of the antihydrogen atoms produced, the antiprotons and positrons in their plasma states must be as cold as possible. Plasma cooling methods are discussed in detail in Chap. 3. Moreover, the antiproton and positron mixing method must be finely tuned to produce the coldest antihydrogen atoms, and mixing processes can cause the particles, especially the antiprotons, to heat up substantially. Previously we autoresonantly excited antiprotons into the positron well, but this caused the antiprotons to heat up dramatically and our trapping rate was limited to about one atom at a time. However, simulations completed a few years ago (see Refs. [75] and [66]) compared the number of injected antiprotons and their temperatures for both the autoresonant excitation scheme and the linear ramp injection. The results showed that the linear potential ramp, which evaporates antiprotons and positrons toward each other, results in a higher number of antiprotons mixing with the positrons at a lower temperature than in the autoresonant injection method. Linear mixing had previously been tried but didn't produce trappable antihydrogen atoms, and it was thought that uncontrolled jitter in plasma parameters made it impossible to develop a successful trapping procedure, while autoresonance is more immune to the jitter. A key result of this thesis is the implementation (Chaps. 3, 4) of a new method to reproducibly control the number and density of lepton plasmas. This allowed for and motivated the successful development of our current linear mixing ramp which yields a trapping rate 15-20 times higher than we achieved with autoresonance. A discussion of these two trapping methods is given in Chap. 5, while this chapter continues with a description of the hardware and software components of ALPHA.

2.2 Overview of the apparatus

Figure 2.1 shows the engineering diagram of the central part of the ALPHA apparatus: the atom trap and surrounding components. The entire apparatus including the catching trap and positron accumulator is too long to show in detail in one figure, so the catching trap is shown in figure 2.2 while the positron accumulator is only described in Sec. 2.2. Key components of the apparatus are marked on the diagrams and described in the following sections:

- First-stage Penning trap: the "catching" trap (Sec. 2.2a)
- Carlsberg Magnet (Sec. 2.2b)
- Liquid helium reservoir and cooling regions (Sec. 2.2c)
- Liquid helium inlets for the cryostat and the Carlsberg magnet (Sec. 2.2d)
- Outer vacuum chamber and outer vacuum chamber heat shield (Sec. 2.2e)
- Ultra high vacuum regions (Sec. 2.2f)
- Gate valves on both ends of the experiment to separate vacuum regions (Sec. 2.2g)
- Ion pumps (Sec. 2.2h)
- Atom trap (Sec. 2.2i)
- Silicon Vertex Detector (Sec. 2.2j)
- Microwave wave guide for the hyperfine measurements (Sec. 2.2k)
- Flappers, for physically blocking radiation and particles traveling down the beamline (Sec. 2.2l)
- Laser beam paths (1S-2S and Lyman-alpha wavelengths) and laser shielding boxes (Sec. 2.2m)
- Movable sticks with an electron gun, electrode, and MCP (Sec. 2.2n)

Catching trap

The catching trap, named because its primary job is to catch and then cool antiprotons, is a cryogenic Penning-Malmberg trap with a 3 T axial magnetic field. The catching trap is cooled by a helium cryocooler which sets the temperature of the trap walls to about 6 K; a separate cryocooler is used to cool the superconducting magnet. It is separated by the antiproton decelerator by a thin metal foil moderator, which separates the higher pressure vacuum in the AD from the ultra high vacuum in ALPHA and moderates the energy of the incoming antiproton beam: when the beam passes through the moderator, the collisions of the particles result in the beam energy spreading out, and the wider distribution provides more slow antiprotons. The trap contains two high voltage electrodes that can be set to ± 5 kV which are necessary to catch the antiproton beam, and is also equipped with a movable stick with an electron gun and micro channel plate detector. The catching trap is physically separated from the atom trap by about 4 meters; the distance in between includes a section of temperature UHV beamline at room temperature with transfer magnets and the movable

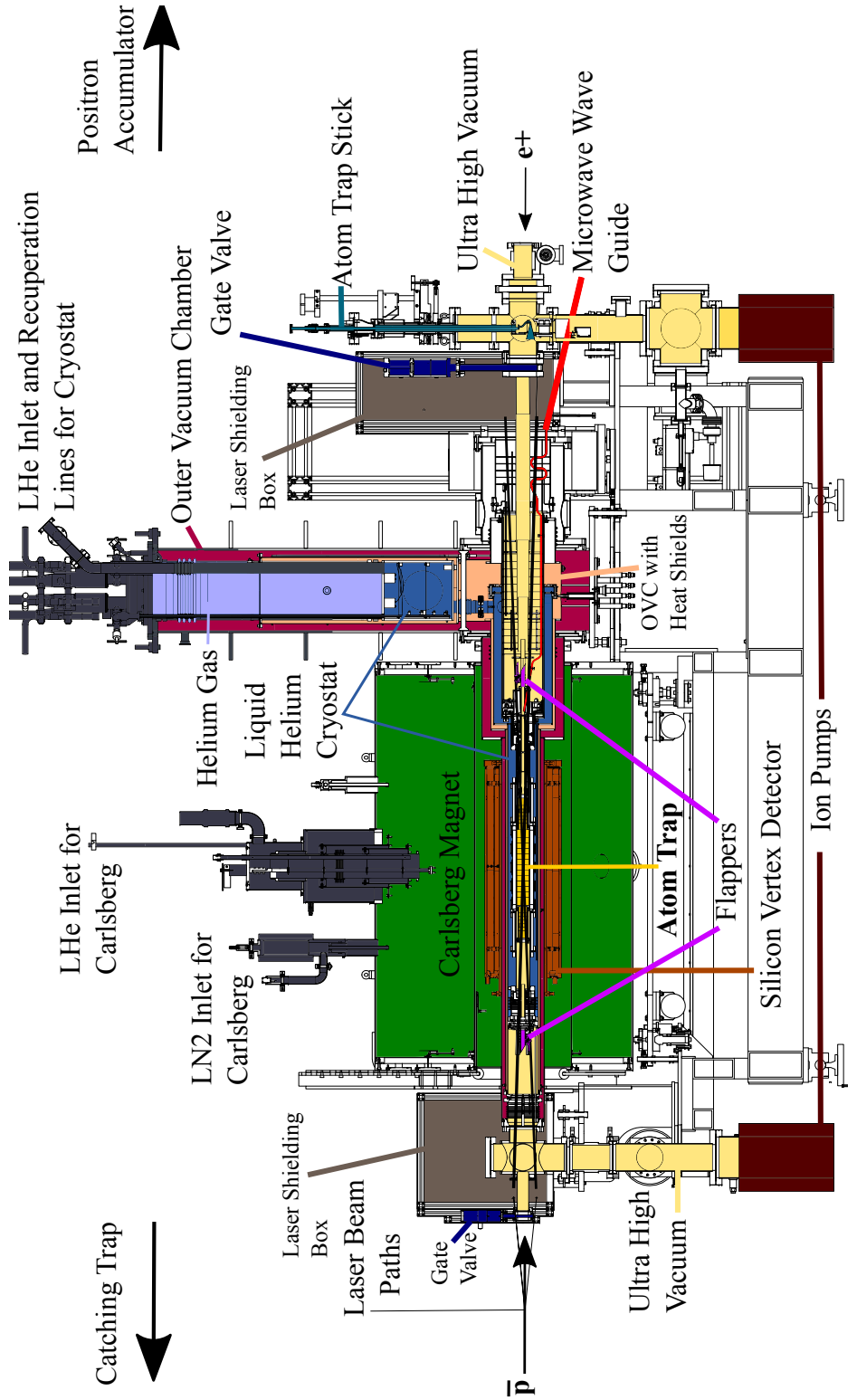

Figure 2.1: Atom trap assembly

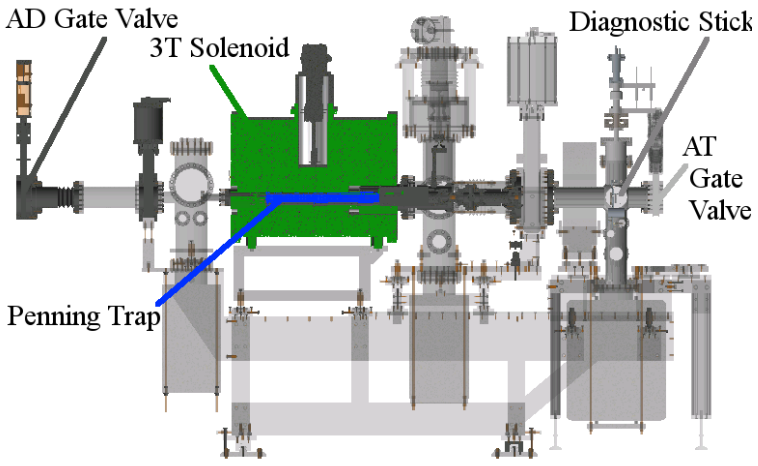

Figure 2.2: Catching trap assembly

diagnostic stick. During normal operation, the atom trap vacuum is open to the catching trap vacuum, but during thermal cycles or interventions, gate valves are closed to isolate the vacuum environments. For example, the valves on both ends of the catching trap in Fig. 2.2 can be closed to isolate the catching trap vacuum from the AD's vacuum and the rest of ALPHA's vacuum.

Carlsberg magnet

The Carlsberg magnet, named for the Carlsberg Foundation which provided the funding to build it, is a large superconducting solenoid which provides a uniform axial magnetic field over approximately 80 cm surrounding the atom trap. It has a liquid nitrogen heat shield and an inner liquid helium reservoir; while not strictly necessary, the LN_2 shield reduces the LHe consumption. We normally set the current to provide a magnetic field of 1 T, but it is capable of producing higher fields. As with all superconducting magnets, slight resistance in the magnet's closed circuit causes the current circulating through the magnet to drop over time, and in this case case at an approximate rate of $0.35\mu T$ per hour. To overcome this systematic drift, we reset the Carlsberg daily or weekly depending on the experimental program. Precise knowledge of the magnetic field is necessary for the hyperfine measurement, because, as outlined above in Sec. 2.1, the hyperfine energy levels scale with the magnetic field. When we know the precise value of the magnetic field we can collect data within a narrow window of parameters and achieve a highly precision measurement.

Resetting the magnet involves turning on the magnet's power supply and ramping up the current to a level matching the current in the magnet. We then turn on a heater that closes a superconducting switch which short-circuits the power supply current output to run in series with the magnet leads. After the current in the magnet matches the power supply current, which we observe by the magnetic field changing, we turn off the heater and wait

a few minutes for the switch to open. When the switch is open we ramp the power supply back down.

The cryogenic environment

The trap is thermally connected to a liquid helium cryostat, which cools the walls of the trap to 5-6K and ensures the trap magnets are superconducting. When cold, the experiment consumes approximately 20 liters of liquid helium an hour to keep the trap magnets superconducting and the walls of the trap cold. To continuously supply the experiment with liquid helium, a 1000 l dewer is permanently stationed next to the experiment; 500 l dewers of liquid helium are transported by crane into the experimental area (the "zone") and we connect shielded transfer lines and a helium gas pressurization line that forces liquid helium to flow into the cryostat inlet pipe and into the 1000 l dewer. Helium gas that boils off is collected in transfer lines, or "recovery" lines, that feed back into CERN's helium liquifier facility.

The cryostat does not have a liquid nitrogen shield, and only has an outer vacuum chamber (OVC) that shields radiation and insulates the cryogenic areas. The OVC functions like a vacuum-insulated thermos with cold helium gas and liquid helium cooling the inside. Inside the OVC are layers of superinsulation and tubes filled with cold helium gas that evaporates from the liquid in the cryostat. These tubes cool heat shields at the downstream end of the OVC, then travel along the top of the OVC region along the trap to the upstream end to cool heat shields there, then return along the bottom of the atom trap to the downstream end after which the gas is sent into the recovery line. At the top of the cryostat, evaporated helium gas cools the high temperature superconducting (HTS) leads that transmit current to the atom trap magnets.

The flow of liquid and gas is controlled by a series of heaters and pressure valves inside the cryostat, which are controlled by a proportional integral derivative (PID) controller. Of particular importance is the level of liquid helium in the cryostat and the temperature of the HTS leads. The rate of gas flow controls the temperature of the HTS leads, and this rate depends on the pressure of the recovery line. The recovery line pressure fluctuates due to helium transfers in any experiment in the AD, and the heaters and valves react to ensure the liquid and gas continue to flow through the right directions.

When operating the experiment, we use a labview virtual instrument program to specify the required temperatures for the HTS leads for the trap magnets and the desired level of liquid helium in the cryostat. The PID loops command the pressurization valves to open or close and heaters to turn on and off, which controls the flow of liquid helium and cold helium gas throughout the cryostat and heat shields to keep the HTS leads at the required temperatures. The program turns off and disables the trap magnets if the cryostat level or HTS lead temperatures cross a threshold.

Ultra high vacuum in the apparatus

Antihydrogen should be a naturally stable atom as is hydrogen, and thus have an infinite lifetime under ideal conditions. In matter-based experiments though, its lifetime is limited by the quality of the vacuum because any gas particle can annihilate the atom. Therefore, to trap antimatter particles for hours or days at a time, an ultra-high vacuum (UHV) and cryogenic trap is necessary. To have the best vacuum the trap must be as cold as possible, because materials inside the trap outgas much less and some of the remaining gas particles freeze to the walls of the trap. Vacuum gauges at the room temperature segments of the trap show vacuum at around 10^{-10} mbar and calculations of the antihydrogen lifetime indicate a cryogenic vacuum of $10^{-13} - 10^{-14}$ mbar [36]. The design of the trap and peripheral components thus have to be UHV and cryogenic compatible materials. During any preparation or intervention, all non-metal components that go in the UHV area have to be cleaned with isopropyl alcohol (IPA) or ethanol and metal components are cleaned with acetone followed by IPA; acetone is the best cleaner but leaves a residue, and IPA removes the residue. A compact ultrasonic cleaner is set up in the experimental area to thoroughly clean small parts with acetone and IPA, and the chemicals are stored in a designated chemical cupboard nearby. Also, it is necessary to use plastic gloves to work with clean parts as the oils in a fingerprint could ruin the vacuum; arm-length plastic gloves are used for deeper interventions.

The experiment is designed to use metal parts for as many components as possible, but some assemblies required epoxy. The epoxy we use is Stycast 2850-FT with catalyst #9, because it is compatible with UHV and cryogenic environments. The internal circuitry connected to the electrodes is a flexible circuit that is also UHV compatible.

We use scroll pumps, turbo pumps, and ion pumps at pressures below 10^{-5} mbar. Anytime we open up the UHV region, after completing an intervention and closing off the vacuum again we bake the internal trap at 80 C and the external hardware (flanges, windows, and ion pumps) at 100-120 C for at least 24 hours to boil off and pump out residual gas particles. The baking process improves the vacuum by 1-2 orders of magnitude, and once the apparatus is cold, at around 5-6K, most remaining gas particles are frozen to the wall of the trap and the pressure drops below 10^{-9} mbar. The low number of background gas particles at this pressure allows antihydrogen atoms to stay in the trap for many hours without annihilating.

As the bakeout process is required anytime the atom trap is opened to atmosphere, we bake the apparatus when we commission the experiment at the beginning of each year's run, and try to avoid doing interventions in the apparatus during the run. If we have to break the vacuum for an intervention, we first bring it up to atmospheric pressure with gaseous nitrogen to reduce the amount of water vapor that enters the trap.

Heat shields and flappers

As described above, the Carlsberg magnet has a liquid nitrogen heat shield and the cryostat has an OVC heat shield, which protect the liquid helium-cooled sections from room

temperature radiation. However, radiation still travels down the trap axis from the room-temperature regions by the sticks shown in Fig. 2.1. To minimize the axial radiation, a series of copper heat shields, disks with holes in the beamline region , are mounted on both the upstream and downstream ends.

Thermal radiation is described by the Stefan-Boltzmann law:

$$q = \epsilon\sigma_B(T_h^4 - T_c^4)A \tag{2.6}$$

where q is the total energy (in watts), $\epsilon = 0.01 - 0.02$ is the emissivity for copper in the temperature range of $150 - 300$ K [76], $\sigma_B = 5.67 \times 10^{-8}$ W/(m^{2}K^4) is the Stefan-Boltzmann constant, T_h is the temperature of the warmer body that radiates, T_c is the temperature of the colder body that absorbs radiation, and A is the surface area of the radiating object. It is obvious here that a material with low emissivity will radiate less energy to a cold surface than one with a high emissivity. Copper has one of the lowest emissivity values so it is commonly used as a heat shield. Using a series of heat shields further reduces the thermal radiation down the beamline.

Figure 5.10a shows the beamline and the first of a few copper heat shields on the upstream end. The flapper is in the cryogenic region of the trap, at a temperature of around $6 - 7$ K, and the narrow tube in the center of the image is part of the flapper, a CAD model of which is shown in Fig. 5.10b. The diameter of the tube is designed to be just large enough to let plasmas be transferred through it. and when the door closes radiation and particles should be blocked from entering the trap down the beamline, except for what propagates through small openings offset from the beamline axis for the laser beams. The flappers were implemented in ALPHA with the hope of reducing the minimum equilibrium temperatures of the plasmas by blocking the thermal radiation. Note that the thermal contraction rates of its titanium and silver parts had to be designed to ensure it would still mechanically operate at the cryogenic temperature and wouldn't be frozen closed by physical contractions. To close the door we send about 250 mA of current through the coil mounted on a long tongue that rotates on a hinge; the other side of the tongue is the door of the flapper, which blocks the beamline when closed. The current flowing through the coil creates a magnetic field that opposes the surrounding 1 T field from the Carlsberg magnet. The motion is similar to how an analog meter works: current flows through a coil in the field of a permanent magnet, and the magnetic force causes the needle to move in an amount proportional to the current. When a strong enough current goes through the coil of the flapper, the magnetic force overcomes the force of gravity and makes the door close. As soon as the current turns off, gravity pulls the door open. A discussion of measurements taken with the flappers closed is in Sec. 5.7.

Atom trap: a Penning-Malmberg trap with mirror magnets and an octupole magnet

The core of the atom trap is a one meter long cryogenic Penning-Malmberg trap and an array of trap magnets inside of the Carlsberg magnet's constant 1T field. Figure 2.5 shows the

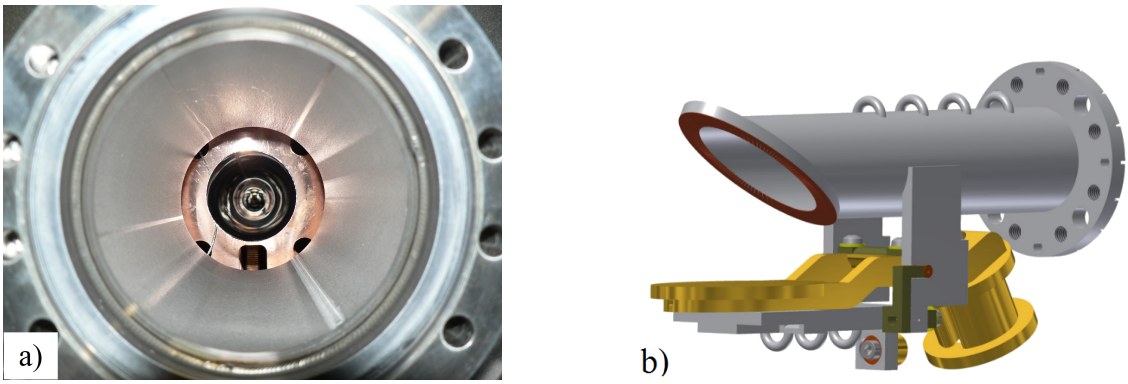

Figure 2.3: a) Photo looking down the beamline, showing the beam pipe, copper heat shields, with the flapper appearing as the small circle farther down the beamline. b) CAD design of the flapper.

arrangement of the trap electrodes, trap magnets, and the silicon vertex detector. Different trap electrodes have different properties: the electrodes at the center of the trap need to be set to precise voltages and are controlled by low-noise amplifiers and have a voltage range of $\pm$ 72 V, while the outer electrodes require less precision and can be set to $\pm$140 V.

To confine antihydrogen in three dimensions, radial and axial fields are required. Five solenoid mirror magnets create the axial magnetic trapping field on top of the base 1T solenoid field. A radially increasing field is produced by a multipolar magnet; the field for multipole order l scales as r^{l-1}. $l = 2$ is a quadrupole, $l = 3$ is a sextupole and $l = 4$ is an octupole. Figure 2.4a shows the normalized fields as a function of radius. Calculations [77] showed that a quadrupole field is not flat enough for sufficient trapping in Penning-Malmberg traps, and ultimately an octupole magnet was chosen for the trap.

The octupole windings are visible underneath the electrically insulating kapton film in the photograph of the trap in Fig. 2.4b. We use very thin electrodes and install the octupole magnet as close as possible to the outside radius of the electrodes because the depth of the trap is defined by the difference in magnetic fields at the wall of the trap and the axis of the trap.

To find the depth of the trap for the combination of the trap magnets, we first have to find the maximum and minimum of the magnitude of the combined magnetic fields from the following equation:

$$\vec{B} = \vec{B}_{\text{Carlsberg}}(z) + \vec{B}_{\text{mir}}(r, z)) + \vec{B}_{\text{oct}}(\theta, r, z). \tag{2.7}$$

Then, the trap depth is, ΔB, is as follows [36]:

$$\Delta B(\text{T}) = \sqrt{B_r^2 + B_z^2} - B_z, \tag{2.8}$$

where the the radial octupole inside the magnet is defined as B_r and the axial mirror fields constitute B_z. The magnet currents are chosen in ALPHA to produce a 0.8 T field depth.

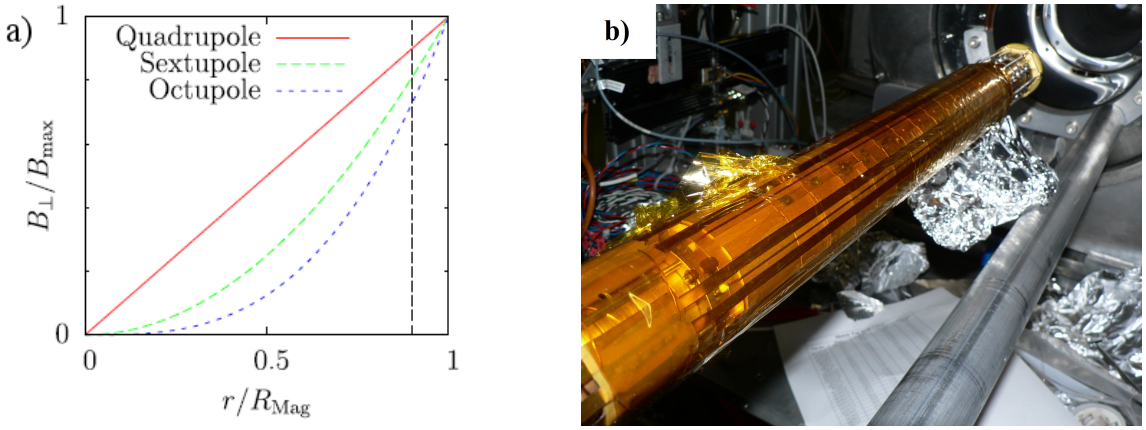

Figure 2.4: a) Radial Multipole Fields, where R_{MAG} is the radius of the magnet. Image from Ref. [78]. b) Photo of octupole magnet mounted over atom trap, with assembly wrapped in insulating kapton film.

A deeper trap depth would improve the trapping rate, but it would be difficult to manufacture an octupole that could carry higher current. Additionally, the inhomogeneity in the azimuthal magnetic field caused by the octupole field induces positron heating, and a stronger field would induce more heating which could negatively affect the trapping rate.

Silicon Vertex Detector and annihilation analysis

Our antihydrogen physics results are based on studies counting individual atoms by their annihilation events. The ability to detect single atom events allows us to make precise measurements with fewer atoms than are typically used in traditional spectroscopy measurements on matter atoms. As previously mentioned, rather than detecting the light emitted by excited atoms falling back to the ground state or a dip in an absorption spectrum, we design experiments where atoms are excited, escape the trap, and almost immediately annihilate with atoms on the wall of the trap. This means that the proof of an interaction between an externally applied signal and the antihydrogen atoms is their annihilation, and our first 1S-2S spectroscopy result was obtained by measuring annihilations of only a few hundred atoms [62].

The Silicon Vertex Detector (SVD) has 72 hybrid silicon modules arranged in three radial layers and detects these individual events. Simultaneous triggers in the detector are reconstructed into tracks [79]. If the tracks can be extrapolated to a single point inside the trap, and if they don't form a single straight line which would indicate a cosmic ray background event, the tracks are likely the result of an annihilation. Analysis code applies a number of cuts to time-coincident tracks to differentiate antihydrogen annihilations from cosmic rays.

Each e^+e^- annihilation event produces two γ rays while $\bar{p}p$ and $\bar{p}n$ annihilation events

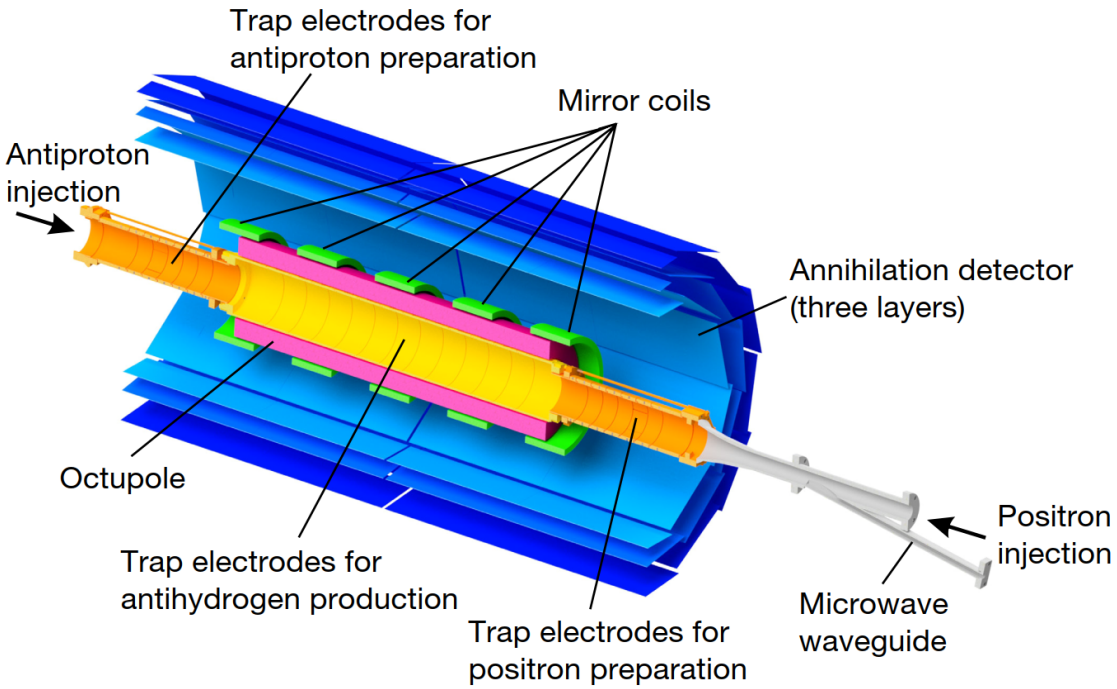

Figure 2.5: Schematic of the atom trap electrodes, microwave access, magnets, and three-layer silicon vertex detector. Figure from Ref. [64]

.

produce pions. Charge conservation requires that $\bar{p}p$ annihilation events produce equal numbers of π^+ and π^- particles and additional π^0 particles, while $\bar{p}n$ annihilation events produce an extra π^- particle along with $\pi^+\pi^-$ pairs and π^0 particles. The SVD is only sensitive to charged particles so we reconstruct events based on the π^+ and π^- particles created in antihydrogen annihilation events. Branching ratios represent the probability for different particle combinations resulting from a decay or interaction. For $\bar{p}p$ annihilations, $\bar{p}p \rightarrow \pi^+\pi^- N\pi^0$ has a branching ratio of 42.6% for N=$\{0, 4\}$ and $\bar{p}p \rightarrow \pi^+\pi^+\pi^-\pi^- N\pi^0$ has a branching ratio of 45.8% for N=$\{0,3\}$ [80]. Annihilation events producing a larger number of charged pions are possible but carry much lower probabilities. The branching ratio for $\bar{p}n \rightarrow \pi^-\pi^0$ events is 16.9%, for $\bar{p}n \rightarrow \pi^-\pi^-\pi^+ N\pi^0$ events is 59%, and for $\bar{p}n \rightarrow \pi^-\pi^-\pi^-\pi^+\pi^+ N\pi^0$ events is 22% [81]. If two charged pions are emitted back-to-back, they will appear in the detector like a single track from a cosmic ray and the event will be rejected; a two-track event is counted as an annihilation event only if the tracks have a noticeable angle between them [82]. The higher probability of events with three charged pions combined with the tracks of three particles easily differentiable from a cosmic ray leads to a high majority of reconstructed events having three charged pions. Since we don't accept events with only a single charged particle, the $\pi^-\pi^0$ events are ignored.

A "mixing trigger" is an event where some number of silicon modules record a signal at the same time, indicating there was possibly an annihilation event, while a "passed cut"

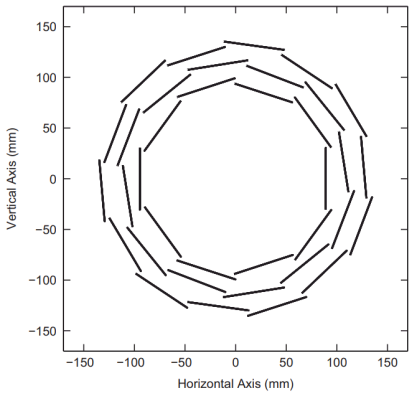

(a) Diagram of silicon modules in the silicon vertex detector. Figure from reference [36].

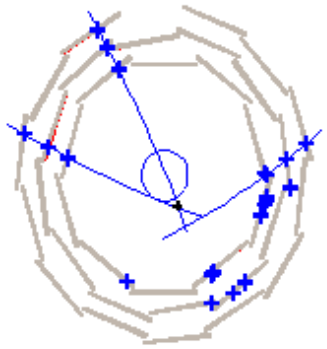

(b) Reconstructed tracks of three charged pions that hit the detector at the same time. Two or more time-coincident tracks that originate from a single point but pass the analysis cuts are counted as an annihilation event and called a "passed cut."

event is one where the the tracks in a triggered event pass the analysis cuts that differentiate between annihilation events and cosmic ray background events. This analysis is performed using multivariate analysis (MVA) software [83, 84]. When we run repeated experiments on antihydrogen over several days, the cosmic ray background rate is measured during free time when there is no antimatter in the experiment in order to track the daily background rate.

The optimization of the cut parameters depends on the length of observation of antihydrogen atoms. The cosmic background rate is constant at about 10 Hz [64], but the signal rate varies substantially for different measurements, depending if the measurement causes antihydrogen atoms to escape the trap and annihilate rapidly or over several minutes. Using more stringent cut parameters decreases the cosmic background but also reduces the efficiency of detecting antihydrogen [85]. For example, in the recent characterization of the 1S-2S transition [63], the signals were measured in observation windows of 1.6s, 32s, and 300s. The cut optimizing the signal for the 1.6s observation gave a background rate of 0.19 Hz and an efficiency of 85% annihilations per detector trigger, meaning that if we measured 85 annihilation events there were 100 annihilation events that occurred, 15 of which were rejected by the analysis. The optimization for the 32s window suppresses the background to 0.033 Hz and an efficiency of about 80%, and the optimization for the 300s window gave a background rate of 0.001 Hz and an efficiency of 47%.

Microwave source

The microwaves are produced by an Agilent 8257D PSG frequency synthesizer and Miteq AMF-4B amplifier [64] and fed into the experiment through a vacuum feedthrough and down a waveguide into the Penning trap. Microwaves are used in ALPHA to drive the hyperfine transition in antihydrogen (Sec. 5.9) and drive electron plasmas at the ECR mode frequency to determine the magnitude of the magnetic field (Sec. 2.4).

Lasers

The 1S-2S transition in antihydrogen is excited by simultaneous interaction with two photons of half the transition frequency; the use of two photons cancels the first order Doppler shift. After the photons interact with the atom, the 2S state atom is no longer trapped and quickly annihilates on the trap wall. To create the photons, an extended cavity diode laser (ECDL) creates 972-nm light which is then processed by a Toptica TA-FHG pro laser system in a small laser laboratory next to the apparatus. The light is then transmitted into the experimental zone and sent through windows in the apparatus to a high finesse cavity inside the cryogenic region of the experiment to produce 150 mW of 243 nm light [63]; inside the cavity the power builds up to approximately 1W. It is not possible to align the cavity exactly along the beamline axis but the cavity mirrors are close to the beamline and angled so that the laser beam crosses the axis of the trap at an angle of only a few degrees in order to maximize its chance of interacting with the trapped antihydrogen atoms. The 1S-2S spectroscopy experiment is discussed in Sec. 5.10.

Diagnostics and electron guns

The long beamline structure in ALPHA requires us to use movable sticks in order to have a microchannel plate (MCP), an electron gun, and an empty "passthrough" electrode that are aligned with the beam axis at different times. There are movable sticks installed in the beamline for the atom trap and the catching trap, as indicated in Figs. 2.1 and 2.2. A CAD diagram of the atom trap stick is shown in Fig. 2.7. Each stick can be moved to the egun position to provide electrons for an electron plasma, then moved down to the passthrough electrode or microchannel plate to transfer particle or diagnose the plasma. These sticks are located along the room-temperature beamline segments of the apparatus and at magnetic fields a factor of 90-100 lower than in the center of the traps. The large gradient in the magnetic field creates a magnetic mirror that blocks a fraction of electrons emitted by the electron gun and causes the plasma to expand when traveling from its potential well to the MCP.

The number of particles is measured with a Faraday cup, the plasma radial density profile is inferred from pictures of the fluorescence of the plasma on the MCP, and the plasma temperature is found by measuring the number of particles escaping the trap as a

function of the potential well depth. These measurements are destructive, as they require dumping the plasma onto the detector.

Faraday Cup

A Faraday Cup (FC) is used to count the total number of charges in the plasma. If we know the capacitance (C) of a metal plate, we can measure the voltage (V) across it from the charged particle beam and determine the charge (Q) by the equation $Q = CV$. A background measurement of the voltage on the plate without a plasma is subtracted from the voltage induced by the plasma, and the integration of the background-subtracted charge distribution as a function of time gives us the total charge. For measurements of plasmas in the catching trap, the moderator for the antiproton beam is used as a Faraday cup. For measurements of plasmas coming from the atom trap, we use a Faraday cup mounted on the catching trap stick.

Micro-channel plate

The Micro-channel plate (MCP) we use in ALPHA is a 40 mm diameter Photonis MCP with a P46 phosphor screen [36]. The MCP is a circular plate with a slanted honeycomb lattice of glass channels, and the front is biased 500-1100 volts higher than the back, creating a very high electric field [86]. The emissive surfaces in the honeycomb lattice and the large electric field induce an avalanche of accelerating charges proportional to the initial number of incident charges, and the charges produce fluorescence on the phosphor screen, which we normally bias to 4700 or 5000V. For a discussion of antiproton, electron, and positron MCP calibration methods and gain settings used in ALPHA, see Ref. [87]; for a general reference regarding MCP detectors, see Ref. [88]. With the high gain in signal, it is possible to detect a single charged particle. To image positrons, the front of the MCP is negatively biased at -100V and to image electrons and antiprotons, the MCP is biased at +100V. Antiprotons produce a much brighter fluorescence because the pions from the annihilation also leave a signal on the phosphor screen. We dump a plasma by putting it into a well about a centimeter long and tens of volts deep, then suddenly bring down the voltage of the trapping electrode to flatten out the well. To ensure all the charges go in the direction of the MCP, the remainder of the well is slanted and a blocking potential is applied on the side opposite the MCP camera. The fluorescence of the phosphor screen is imaged by a CCD camera and shows us the radial profile of a plasma as in Fig. 2.8.

We fit the intensity distribution of the image to a generalized gaussian function:

$$f(r) = ae^{-(r/b)^{\alpha}} + c \tag{2.9}$$

where a is the line-integrated density, b is the plasma radius, and $\alpha \approx 2$ describes the scale of the drop-off region in Fig. 2.8 and indicates how close the plasma density distribution is to a true gaussian where $\alpha = 2$. The normalized net intensity (NNI) calculated by the fit can

be calibrated to the number of particles by preparing identical plasmas and measuring the NNI and the number of particles on the FC and finding the factor to convert between the two. We can increase the fluorescence by increasing the MCP gain, which we do for certain measurements on a few hundred or thousand particles. If the MCP image is saturated, which is indicated by the line-integrated density being above a threshold or by a sharp drop-off over the radius, we decrease the gain.

Anytime the camera is physically moved we need to measure the pixel-to-mm calibration. To do this, we take an image of the edge of the MCP, use software to fit the edge of the MCP to a circle with diameter 40 mm and calculate the conversion factor. The final piece of information we need to determine the plasma parameters are the values of the magnetic fields at the location the plasma was in just prior to being dumped to the MCP and the magnetic field at the MCP; as particles follow along field lines, the plasma expands radially by a "fringe factor" of $\sqrt{B_{\text{trap}}/B_{MCP}}$ when traveling through the magnetic field gradient form the high-field region in the trap to the low-field region at the MCP. For example, if a plasma was in a 1T field in the trap and the MCP is at a 0.01T field, the fringe factor is 10, meaning that the radius is 10 times larger at the MCP than it was in the trap.

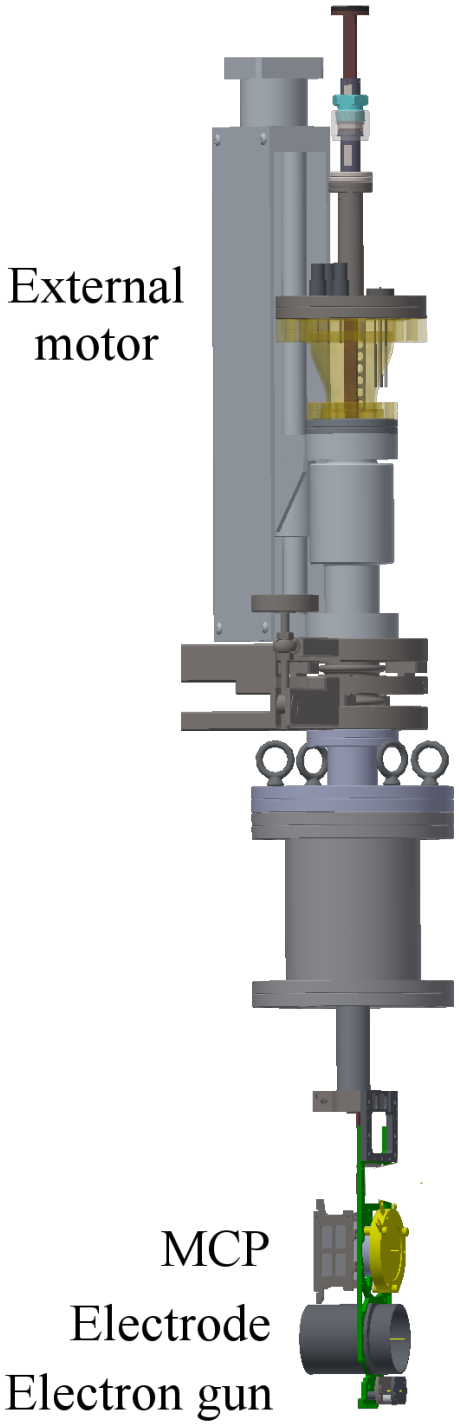

Figure 2.7: The atom trap "stick" with vertically stacked elements: an MCP and phosphor plate assembly, an electrode, and an electron gun.

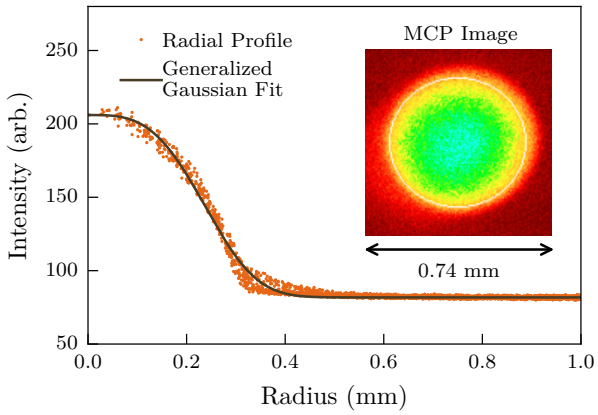

Figure 2.8: Image data (orange circles) and generalized Gaussian fit (brown line) of the intensity as a function of radius corresponding to the inset MCP image of an electron plasma. Figure from reference [65].

Plasma temperature diagnostic

We generally assume that particles in plasmas are in thermal equilibrium with each other and that the parallel and perpendicular temperatures of particles are equal. To measure the parallel temperature of the plasma, we measure the number of particles escaping and map it to the depth of the potential well it was in: particles must have energy $E = q(\phi_w - \phi_c)$ where ϕ_w is the blocking potential applied by the electrode and ϕ_c is the self-potential of the plasma. Following the discussion in [89], we assume the parallel temperature of the plasma is Maxwellian. While ϕ_c will change as the plasma is dumped, we can approximate it as a constant while the first few particles escape the well, and then define $E = q(\phi_e)$ where $\phi_e = \phi_w - \phi_c$ at the moment the plasma starts to escape.

Thus, since a Maxwellian distribution F scales with the number N:

$$F(E) \propto \exp\left[-\frac{E}{k_B T}\right], \tag{2.10}$$

$$\rightarrow N(q\phi_e) \propto \exp\left[-\frac{q\phi_e}{k_B T}\right]. \tag{2.11}$$

Experimentally, we map the 20ms dump time to the simultaneous ramp voltage of the potential well and measure the number of particles escaping as a function of time. Instead of only using a Faraday cup, we use an MCP to amplify the signal and the phosphor screen as an FC to record the voltage (from which we calculate the charge) as a function of time. We fit a semi-log line to the first few number measurements as a function of the blocking potential to calculate the temperature:

$$T(E) = \frac{\ln(N(E))}{q\phi_e k_B}. \tag{2.12}$$

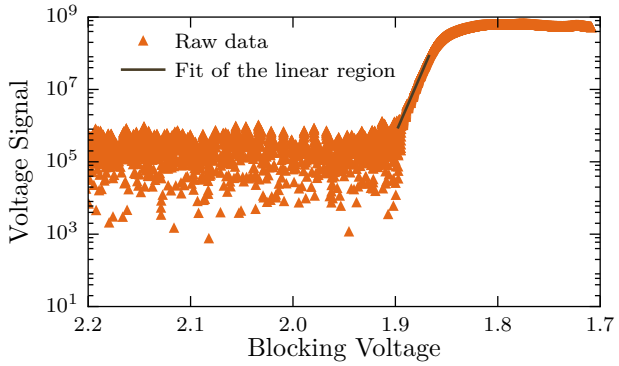

Figure 2.9: Temperature data recorded from a plasma at 81K calculated from the exponential fit.

The positron source and accumulator

The radioactive Na-22 source emits positrons in β^+ decays. The moderation and accumulation process is described in [36] and summarized in this section. In order to create a beam of cold positrons with nearly the same energy, the positrons pass through a solid neon moderator. Following ionizing collisions inside the moderator, approximately 0.5% of the initial number of positrons emerge as a beam of positrons at about 80 eV. This energy is set by the bias voltage of the moderator and the band-gap energy of solid neon [90]. In order to freeze the neon, the source and the moderator are cooled to about 5 K with a cold-head cryocooler. Periodically, on the order of a few weeks, the number of positrons transferred into the atom trap drops, which is a sign that the moderator is not moderating the beam well enough and needs to be regrown. It is unknown why the moderator fails, but possible reasons are that the neon ice sublimates or becomes contaminated. To regrow a moderator, heaters turn on to raise the cold-head temperature to 30-40K so that the neon sublimates, and then the cold-head is cooled back down. Once cold, neon gas is flowed into a small chamber around the moderator, and a thin layer freezes onto a thin metal window just below the source and becomes the new moderator.

In ALPHA, we use a Surko-type positron accumulator [91], and our accumulator's Penning-Malmberg trap is surrounded by a 0.14 T axial magnetic field created by a non-superconducting copper magnet. This type of accumulator includes a trap with three stages of nitrogen buffer gas cooling at different pressures, and each stage of buffer gas cooling is 500-650mm long.

In the first stage, the positrons enter a long single electrode and mix with N_2 gas at 10^{-3} mbar. Positrons emitted by the source can cool by transfering kinetic energy to an electron in an N_2 molecule during an inelastic collision, or can annihilate with an electron in the molecule and form positronium:

$$e^+ + N_2 \rightarrow e +^+ N_2^* \tag{2.13}$$

or

$$e^+ + N_2 \rightarrow Ps + N_2^+; \tag{2.14}$$

it is expected that about 30% of the positrons from the beam cool in the nitrogen gas are not annihilated, and are captured in the first stage of the accumulator [91].

The second stage has a lower gas pressure at around 10^{-4} mbar and a single electrode biased to a lower voltage (creating a deeper well than in the first stage) and the third stage has the lowest gas pressure at 10^{-6} mbar and a series of four electrodes that are used to create the final trapping well. To obtain the gradient in pressures in a Surko-type accumulator, the diameter of the electrodes is increased with each stage and gas is let into the first stage electrode and pumped out of the middle electrode, with an additional vacuum pump at the end of the final stage. All of the gas is pumped out prior to opening a gate valve that separates the accumulator vacuum and the trap vacuum and transferring the positrons into the atom trap. The transfer efficiency in ALPHA is low, possibly because of mirror magnetic fields blocking particles. Even when a few tens of millions of positrons are trapped in the accumulator after 100s, during the 2016 run we only caught 4-6 million in the atom trap.

2.3 Experimental protocols and procedures

Programming the apparatus

In ALPHA, almost all hardware devices are controlled by labview. The electrode potentials and other hardware commands are written in individual routines called "macros," while multiple potential well manipulations and other hardware procedures are programmed sequentially in "sequences." The top-level software is called the "master controller" which compiles and runs the macros, sending control bits to all the connected hardware components. A sequence to trap antihydrogen has hundreds of thousands of individual commands; a simple procedure such as shifting a plasma from being trapped in one well to the neighboring well is typically done by ramping voltages over 1-10 thousand steps to avoid heating or disturbing the plasma.

For example, to load an electron plasma in the catching trap and count the number of particles, one loads a sequence into the catching trap section of the master controller and highlights the settings that tell the stick to move into the position of the electron gun, turn on the electron gun, prepare a potential well in the trap that catches electrons, turn off the electron gun, and morph the potential well to dump the particles onto the faraday cup. One can use the same sequence and change the settings to instead dump the particles onto the microchannel plate, or load up an additional sequence that controls the potentials in the atom trap and highlight the settings to transfer the plasma from the catching trap to the atom trap. Almost all developments of the plasma operations involve creating entirely new sequences or editing existing ones. A substantial amount of the experimental work that went into this thesis research was spent developing, testing, and optimizing new sequences.

Online monitoring logs and the electronic logbook

We record experimental procedures and informally summarize results in an electronic logbook called the elog, and track experimental conditions (vacuum pressure, temperature, etc.) in MIDAS, an automatic online database of sensor data. These online monitoring tools are part of an open-source software package developed at PSI and TRIUMPH [92]. MIDAS has preset thresholds for normal operating values, and if a sensor reads a value out of range a warning is displayed on the main page and a verbal warning is automatically generated and played over the speakers of any computer looking at the main page of MIDAS. These online databases and the automatic warnings are essential for safely operating the experiment and enable us to to look up experimental conditions at any time in the past. Additional database entries are also automatically generated and uploaded to the elog containing information about sequences executed, other experimental settings, and antihydrogen trapping analysis results.

2.4 Electron cyclotron resonance measurements as a magnetic field diagnostic

While Hall probes are installed in various points in the experiment, the most precise way of measuring the magnetic field *in situ* is by measuring the electron cyclotron resonance (ECR) frequency of the plasma [93]. This method and its implementation in the ALPHA experiment are described in detail in reference [94] and summarized here.

Some aspects of the collective behavior of a plasma can be characterized by the azimuthal mode number ℓ. The three most common modes are the sloshing mode when $\ell = 0$, diocotron mode when $\ell = 1$, and the quadrupole mode when $\ell = 2$. In the sloshing mode, the center of mass of the plasma oscillates inside the trap. In the diocotron mode, the plasma exhibits bulk rotation about the center of the trap; this is observed on MCP images where repeated measurements of plasmas show the plasma center moving around a circle. In the quadrupole or "breathing" mode, the plasma expands and contracts radially, alternating in perpendicular directions.

Electrons and positrons rotate in a magnetic field at the cyclotron frequency,

$$f_c = \frac{|e|B}{2\pi m_e}; \tag{2.15}$$

at 1 Tesla, $f_c = 28$ GHz. Electron plasmas in Penning traps oscillate at the electron cyclotron mode frequency, which is shifted slightly from the single particle ECR frequency due to the mode behavior described above. The ECR mode frequency is defined as $f_{c,\ell} = f_c + \Delta f_{c,\ell}$. $\Delta f_{c,\ell}$ is defined as:

$$\Delta f_{c,\ell} = \left[\ell - 1 - \left(\frac{r_p}{r_w}\right)^{2\ell}\right] f_r, \tag{2.16}$$

where r_p is the plasma radius, r_w is the radius of the wall, and f_r is the rotation frequency. Normally we expect the plasma to be in the $\ell = 1$ (diocotron) mode.

When the plasma is cold and in thermal equilibrium,

$$f_r = f_{E\times B} = \left(\frac{E_r}{2\pi r_p B}\right). \tag{2.17}$$

For $\ell = 1$, the frequency is down-shifted from the single-particle ECR frequency by an amount $\Delta f_{c,1} = -(r_p/r_w)^2 f_{E\times B}$.

Our methods for determining the ECR frequency of the plasma are based on measurements of the relative temperature, as the plasma will heat up the most when driven at the resonant ECR frequency [93]. One method is to observe the plasma quadrupole mode frequency; this frequency is approximately linearly dependent to the plasma temperature. To perform this ECR measurement, we drive the plasma at a range of frequencies near the expected ECR frequency, for example 16 frequencies in the range of 27.9-28.1 GHz, in 4μs pulses at an amplitude of 2 dBm. Each pulse is separated by few seconds to allow the plasma to cool down. At the same time we drive the quadrupole mode with one electrode and pick up the image charge that appears due to the quadrupole oscillations on the neighboring electrode. We make a plot with the quadrupole mode frequency versus the approximately 28 GHz microwave frequencies and find the peak quadrupole mode frequency. We read from the plot the microwave frequency that was applied that drove the peak; this frequency is the ECR plasma frequency.

An ECR frequency measurement can also be made by sequentially loading, driving, and dumping dozens of small plasmas to directly measure their temperatures as a function of the applied GHz frequency. This method was developed by the Fajans' group at Berkeley [95] as part of the thesis work of Eric Hunter and was implemented by him in the ALPHA experiment in 2017. A "reservoir" of electrons is loaded with tens of millions of electrons, from which ten thousand to a million particles are extracted, moved to the desired location for a magnetic field measurement, allowed to cool for a few seconds in the magnetic field, driven by microwaves at 80 different frequencies near the expected ECR frequency, and dumped in a temperature dump (see Sec. 2.2). The peak temperature corresponds to the ECR mode frequency; see Fig. 2.10. We use a 1 ms microwave pulse for this method because the density of the small plasma is lower, meaning the collision rate is smaller and it takes longer to reach thermal equilibrium. When driving at a longer pulse length we must reduce the amplitude to not heat the plasma (or trap electrodes) too much, so we use an amplitude of -2 dBm. We drive each small plasma at a range of microwave frequencies as used in the quadrupole mode measurement, and make a plot of temperature versus microwave frequency to similarly determine the resonant ECR frequency.

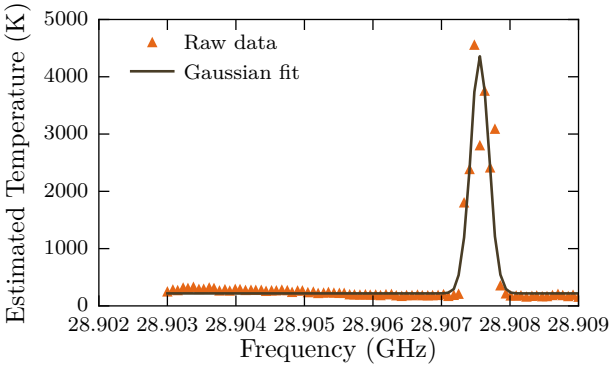

Figure 2.10: Plasma temperatures as a function of microwave frequency; the peak corresponds to the plasma ECR frequency and is used to directly determine the magnetic field.

2.5 Antihydrogen trapping: sequence of plasma manipulations

Load electrons and then antiprotons into the catching trap

Antihydrogen production begins upstream in the catching trap. First, the Egun is moved into position while we wait for a trigger that goes high a specific amount of time before the antiproton bunch arrives. After receiving the timing trigger, the Egun is turned on, around 110×10^6 electrons are loaded into the trap and then, using the SDREVC method described in chapter 4, reduced to 92×10^6 electrons. A high-voltage electrode is triggered by a second trigger from the AD and closes the potential well immediately after the antiprotons are trapped; the well is shown in Fig. 2.11. We then cool the antiprotons for 20 seconds with the large electron load, and release antiprotons that are too hot by turning off the 5 kV potential in a process called a "hot dump," retaining only the particles that were cold enough to stay trapped in a 75V well, usually about 70%. Following the hot dump we divide the potential well to extract 20% of the cold antiprotons and dump them in order to measure how many antiprotons we have in that mixing cycle; this is called the "fifth dump." We cool the remaining of the antiprotons with the electrons (Sec. 3.4), and apply a rotating electric field (Sec. 3.3) to compress the plasma. Repulsive coulomb collisions between the particles ensure the antiprotons and electrons are in thermal equilibrium while the rotating wall compresses the mixed plasma [96]. The antiproton plasma is compressed such that its radius is generally the same as radius of the electron plasma, even though the two species typically exhibit centrifugal separation [97]. SDREVC is applied to the combined plasmas to reduce the electron load to around 23×10^6 particles; a small fraction of the antiprotons also evaporate during this SDREVC process, but not enough to noticeably affect the trapping rate. Following another compression cycle, we then eject the electrons and either transfer the antiprotons to the atom trap, or take a diagnostic measurement by dumping the cold

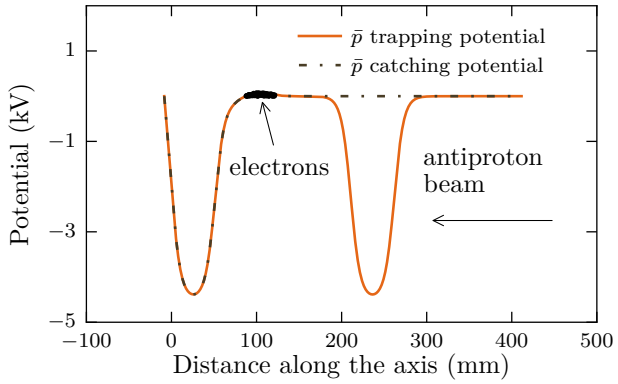

Figure 2.11: The 4.5 kV voltage catching potential with a small 75 V well that initially holds the electron plasma. The brown dashed line shows the one-sided catching potential while the orange solid line shows the trapping potential, after the high voltage barrier (gate potential) on the right is lowered immediately after the beam arrives.

antiprotons to the MCP to record the plasma's radial profile or temperature.

Kicking out electrons: ekicks

Ejecting the electrons while retaining the antiprotons can be accomplished by negatively biasing the potential well and quickly opening up one end of it for a few nanoseconds, then closing it again; this procedure is called an "ekick." The large mass difference allows the electrons to quickly escape before the antiprotons move out of the well, but the antiprotons are heated by collisions with the accelerating electrons. To reduce the amount the antiprotons heat up, we eliminate the electrons in a series of three ekicks, each with the gate opening up deeper, until all of the electrons are gone; during the first ekick we can eject 90% of the electrons, pause for about 20s to let the remaining electrons re-cool the antiprotons, then during the 2nd ekick reduce remainder by 99% and finally with the 3rd ekick get rid of all the rest of the electrons. The deepest ekicks would cause the antiprotons to heat the most as the electrons accelerate the most, but by cooling after the first ekick and doing the deepest ekicks on about 20 thousand electrons instead of 20 million electrons or more, the antiprotons are not substantially heated. The catching trap preparation cools the antiprotons by five orders of magnitude from 4.5×10^3 eV to approximately 0.045 eV.

Preparing positrons and antiprotons in the atom trap

Following the last ekick in the catching trap, the antiprotons are ejected from the catching trap and transferred down the beamline to the atom trap where they are caught and mixed with another electron plasma. Two solenoids provide local 3T fields at both ends of the atom trap, and the trap magnets are on to create a 0.8 T deep magnetic well in the center of the

trap. A few seconds after the antiprotons are transferred, the positrons are transferred from the accumulator into the atom trap, in the end opposite the antiprotons. The antiproton preparation in the atom trap is similar to the preparation in the catching trap, including a hot dump (but no fifth dump), compressing and cooling stages in a 3T field, and three ekicks with an intermediate cooling stage until the antiprotons are at cryogenic temperatures and all the electrons are gone. Inside the other end of the trap, the positrons are cooled in a 3T field, then potentials are applied to heat and remove ions from the positrons. SDREVC is applied to the positrons to produce a uniform number, 3×10^6 Following SDREVC the positrons are put in a deep well that axially compresses them. After cooling for 10s, the plasma is transferred to a shallow and longer well next to the antiprotons. In this step the positrons expand along the axis and adiabatically cool (see Sec. 3.4). Sequences using this adiabatic cooling procedure instead of evaporative cooling yielded the highest antihydrogen trapping rate.

The positron temperature after adiabatic cooling is usually in the range of 15-25 K while the antiproton temperature is in the range of 70-100K. Finally, the antiprotons and positrons are mixed to form antihydrogen. See Sec. 5.1 for a discussion on previous and current trapping methods. After the synthesis is complete, the potentials are ramped in a way to release and accelerate remaining charged particles down the axis. This pushes out remaining charged particles in order to ensure only antihydrogen atoms are trapped. Since the SVD detector is sensitive to antiproton annihilations, it is particularly important to ensure no antiprotons remain in the trapping region during our measurements on antihydrogen. The trapped antihydrogen atoms are then ready for experiments, and have a lifetime of 60 hours or longer [63]. When a measurement or set of measurements finishes, the trap magnets are turned off and electrode potentials are set to zero.

Chapter 3

Plasma Physics in ALPHA

3.1 Particle behavior in the plasma regime

In the single particle regime particle dynamics are dominated by externally applied forces. In this regime, a particle exhibits cyclotron motion while rotating in a circle perpendicular to $\vec{B}$ and longitudinal oscillation in the electrostatic potential well. The effects of self-fields, for example particle interactions via the coulomb force, are negligible. In the plasma regime, however, the collective behavior of particles significantly affects the particle dynamics. This thesis presents a new method to control plasmas and make them reproducible regardless of the effect of initial collective forces and plasma parameters, and this chapter presents the theory behind the experimental developments.

Characteristics of plasmas

In a plasma, a collection of charged particles produces an electric field that shields the applied electric field (this is one of the definitions of a plasma). This shielding is termed "Debye shielding", and the distance over which the plasma shields the applied potential by a factor of $1/e$ is the debye length λ_D:

$$\lambda_D = \left(\frac{k_B T_e}{4\pi n e^2} \right)^{1/2}. \tag{3.1}$$

The number of particles in a sphere with radius of a debye length depends on the plasma's density:

$$N_D = \frac{4}{3}\pi \lambda_D^3, \tag{3.2}$$

and, finally, in order for electric and magnetic interactions to dominate interactions with neutral particles, the plasma frequency, $\omega_p = (4\pi n_0 e^2/m)^{\frac{1}{2}}$, must be large compared to the collision frequency, $\nu_{coll.} = (\pi e^4)/(m_e^2 v^3)$.

A collection of ionized particles exhibits collective behavior and is called a plasma if three conditions are met: if the shielding occurs within the length of the plasma, meaning that $L \gg$

λ_D; if the density of particles is such that $N_D \gg 1$; and if the particles' oscillation frequency satisfies $\omega_p \gg \omega_{coll.}$. Note that these parameters are all relative to the overall conditions and are not absolute thresholds. Comparing plasmas found in nature, the temperature ranges from 100 K in the aurora borealis to 10^7 K in the core of the sun, and the density ranges from 10^6 cm^{-3} in the intergalactic medium to 10^{36}cm^{-3} in the core of the sun. The wide range of plasma parameters contributes to the fact that more than 99% of the observed and understood universe is in the plasma state. Due to the high ionization energy required to transform a gas into a plasma, the only naturally occurring plasmas on earth are in lightning bolts, while aurora borealis is a plasma in the upper atmosphere.

Most plasmas are created from a neutral gas, for example by heating the gas until it ionizes. This is the process that occurs inside neon plasma light signs, in lightning bolts, inside the sun, and in plasma fusion reactors. These are called neutral plasmas since the total sum of the charges is approximately zero. The electrons and ions behave very differently due to their large mass difference, and calculations of plasma dynamics usually require approximations, for example approximating the sum of the electron and ion masses as equal to the ion mass, or approximating the velocity of ions as zero when studying the motion of electrons.

Non-neutral plasmas consist of particles with the same charge. Due to the strong repulsive coulomb force present in this type of plasma, collective dynamics are present at lower densities than required for collective behavior in a neutral plasma. For either neutral or non-neutral plasmas, the self-potential of the plasma must play a prominent role in the particle dynamics. This self-potential, ϕ, is the electric potential seen by the particles on the center of the axis, and $\phi_c \equiv \phi(r = 0)$ can be found by integrating the electric field from $r = 0$ to $r = r_w$. To understand the utility of the new technique presented in this thesis, we briefly calculate for future reference the expression for ϕ_c for a long cold ($T = 0$) plasma :

$$\phi_c = -\int_{\infty}^{0} \vec{E} \cdot \vec{dl} \tag{3.3}$$

$$= -\int_{r_w}^{r_p} E dr - \int_{r_p}^{0} E dr \tag{3.4}$$

$$= -\frac{enr_p^2}{2\epsilon_0} \ln(r)\Big|_{r_w}^{r_p} - \frac{enr_p^2}{4\epsilon_0}\Big|_{r_p}^{0} \tag{3.5}$$

$$= \frac{enr_p^2}{2\epsilon_0} \ln\left(\frac{r_w}{r_p}\right) + \frac{enr_p^2}{4\epsilon_0} \tag{3.6}$$

$$= \frac{enr_p^2}{4\epsilon_0}\left[1 + 2\ln\left(\frac{r_w}{r_p}\right)\right], \tag{3.7}$$

where r_w is the radius of the electrode, r_p is the radius of the plasma, and n is the plasma density (assumed to be uniform). The zero-temperature approximation comes from the assumption that the temperature of the plasma is small compared to ϕ_c. In ALPHA, typical plasma temperatures are less than 0.05 eV. Typical space charge values are a few volts, so

this assumption is reasonable. An analytical calculation of the relationship between ϕ_c, N and n at non-zero temperatures is given in section 4.5. Equation 3.3 shows that for an infinite length plasma, the variables ϕ_c, the line density $n = N$ particles per unit length, and the number of particles N uniquely define the plasma. Controlling any two of the three variables will set the value for the third variable; the significance of this will be discussed later in this chapter.

3.2 Trapping leptons, ions and plasmas

Two standard trap configurations for single (or non-interacting) charged particle confinement are quadrupole Paul traps and Penning traps, both of which were invented in the 1950s. Wolfgang Paul invented the quadrupole radiofrequency ion trap [98, 99]. Inspired by Paul's developments and also Frans Michel Penning's ion gauge, Hans Dehmelt then built a trap with static electric potentials and an axial magnetic field [100]. Normally, Paul traps have hyperbolic electrode surfaces, but there is a linear Paul trip where the quadrupole RF field is generated by driving a set of four hyperbolically-shaped rods oriented around the axis [101]. The Nobel prize in physics 1989 was awarded half to Paul and Dehmelt "for the development of the ion trap technique" and half to Norman F. Ramsey for a separate discovery, "the invention of the separated oscillatory fields method and its use in the hydrogen maser and other atomic clocks" [102]. In addition to antihydrogen production, ion traps are used for for mass spectrometry [103], ion crystal formation [104, 105], positron-electron pair plasmas [40], and atomic clocks [106].

These traps can be at room temperature or cryogenic. For laser-cooled trapped ion experiments the trap is not required to be cryogenic, naturally, but most other experiments require cryogenic traps in order to have good confinement. Laser-cooling of ions is usually performed in a Paul trap because there is no applied magnetic field around the trapping region. Non-superconducting solenoids can be used for fields up to a few kilogauss, but the 1-5 T fields usually used in Penning trap experiments require a superconducting magnet.

Penning traps come in two variations: traditional Penning traps use hyperbolically-shaped electrodes with ring end caps more suitable for single charged particles, while Penning-Malmberg traps have cylindrical electrodes that allow plasmas to be transferred in and out along the axis. The static quadrupole electric potentials trap charged particles axially and the axial magnetic field traps them radially. Planar surfaces are also being studied as a type of Penning trap [107]. Paul traps are generally used to trap small numbers of charged particles, for example in ion crystal experiments, while Penning-Malmberg traps are suitable for both single particle and plasma experiments. A portion of the Penning-Malmberg trap used in ALPHA is illustrated in Fig. 3.1.

The gaps between the electrodes are electrically isolated with either ruby or sapphire balls, and potentials up to 5 kV can be applied to the electrodes. The stability of trapped non-neutral particles or plasmas allows them to be confined for days at a time in an ultra-high vacuum and cryogenic trap, and, as previously mentioned, the BASE collaboration reported

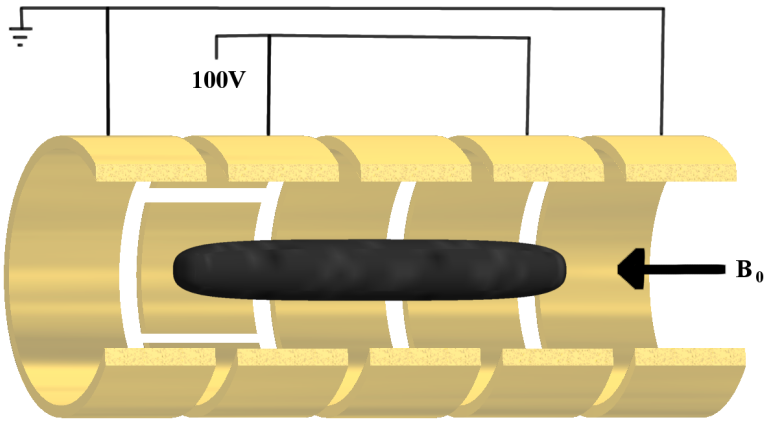

Figure 3.1: Example of a plasma trapped in a Penning-Malmberg trap with a segmented rotating wall electrode.

trapping a small number of antiprotons for more than a year [52]. Excellent introductions to further properties of non-neutral plasmas are given in Refs. [108] and [109].

3.3 Overview of plasma manipulations performed in ALPHA prior to antihydrogen synthesis

Plasma confinement using a rotating wall

With any trapped plasma, the plasma will slowly expand and hit the wall of the trap. In Penning or Penning-Malmberg traps, axial confinement is assured by the electric potential barriers, but the radial magnetic confinement is not perfect so radial expansion and eventually radial particle loss occurs. O'Neil derived an upper bound on the particle loss from the conservation of angular momentum and conservation of energy equations for an electron in a Penning trap [110]; a summary is given here. Following his derivation, under normal trapping conditions, the angular momentum reduces to a summation over r^2:

$$L \approx -\sum_i m\Omega r_i^2/2 \tag{3.8}$$

where L is the angular momentum, $\Omega = eB/m$ is the cyclotron frequency, and r_i is the radius of the i'th electron. If a is the plasma RMS radius,

$$\sum_i r_i^2(0) = Na^2. \tag{3.9}$$

If the system is azimuthally symmetric, this sets an upper limit on the loss of particles:

$$(\Delta N) r_w^2 \leq \sum_i r_i^2 = Na^2. \tag{3.10}$$

As long as the plasma radius is small relative to the wall radius, r_w, the plasma should be well-confined inside the trap. However, experimental and theoretical studies have shown that error fields and collisions with neutral gas particles in the trap change the angular momentum and drive particles to the wall. Thus for confinement time of hours or days it is necessary to actively compress the plasmas.

Plasma compression

A plasma in a cylindrical Penning trap is ellipsoidally shaped but is often approximated as a long cylinder. The radial self-electric field, E_r, of a cylindrical non-neutral plasma with uniform density n, and radius r_p and length $L \gg r_p$ is:

$$E_r = \left(\frac{er}{2\epsilon_0}\right) n. \tag{3.11}$$

In a magnetic field, the combination of the axial magnetic field and radial electric field cause a non-neutral plasma with uniform density to rotate around its axis at the $\vec{E_r} \times \vec{B}$ drift frequency:

$$f_{E\times B} = \left(\frac{E_r}{2\pi r B}\right) \tag{3.12}$$

$$= \left(\frac{|e|}{4\pi\epsilon_0 B}\right) n. \tag{3.13}$$

The relationship between the $\vec{E_r} \times \vec{B}$ frequency and the plasma density is an essential plasma characteristic we manipulate to eliminate the particle loss described in the previous section. Huang et al. [111] developed the "rotating wall" technique that drives a rotating electric field along the axis of the plasma, which applies a torque to the plasma and changes its angular momentum. If the RW drive frequency is greater than plasma rotation frequency, the torque from the drive increases L, makes the plasma spin faster, and compresses the plasma; if the RW frequency is less than the plasma rotation frequency, the drive decreases L, makes the plasma spin slower, and expands the plasma. This technique was applied to a magnesium ion plasma in 1996 [112] and an electron plasma in 1998 [113]. A plasma trapped in a RW field can be confined for weeks at a time [112] and a range of densities can be controlled by the rotating wall drive.

To produce a rotating electric field, we apply phase-shifted and time-varying sinusoidal voltages to a segmented "rotating wall" (RW) electrode, shown in Fig. 3.2. These RW electrodes are divided azimuthally into an even number of segments, usually 4, 6, or 8; in ALPHA we use RW electrodes with six segments in both the catching trap and atom traps. For a RW electrode with n segments, we apply to the j'th electrode the voltage

$$\phi_j = A\cos[m(2\pi \mathrm{f}_{\mathrm{app}} t \pm \theta_j)], \tag{3.14}$$

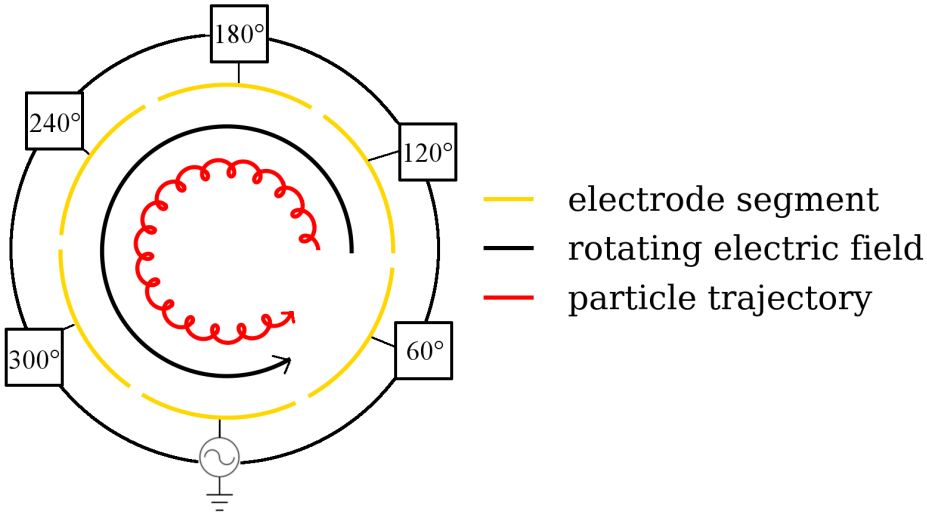

Figure 3.2: Trajectory of a particle with $E \times B$ motion combined with cyclotron motion in a rotating electric field. The phase of the voltage applied to each electrode is indicated in the boxes.

with A the amplitude of the voltage, f_{app} the rotation frequency, $\theta_j = 2\pi j/n$ and m corresponding to the plasma mode number. The direction of rotation corresponding to $\pm\theta_j$ must be chosen with respect to the sign of charge of the particles and the direction of $\vec{B}$. A larger number of segments produces a rotating field with fewer harmonics, and can drive more modes; for example a 4-segmented electrode can only effectively drive the dipole mode ($m = 1$), while a 6-segmented electrode can drive the quadrupole mode ($m = 2$).

There is a limit to the maximum stable density of a non-neutral plasma, the Brillouin limit, n_B [114]:

$$n_B = \frac{m\epsilon_0\Omega_c^2}{2q^2} \tag{3.15}$$

$$= \frac{B^2}{2\mu_0 mc^2} \tag{3.16}$$

which is the energy density of the magnetic field divided by the rest energy of electrons. For electrons in a 1T field, this limit is $4.9 \times 10^{24}\,\mathrm{cm}^{-3}$. This limit means we cannot apply an arbitrarily high frequency rotating wall and achieve an arbitrarily high density. In practice no lepton plasma has been compressed to anywhere near this limit, while a laser-cooled Mg^+ ion plasma has been compressed up to 20% of the Brillouin limit [112].

The rotating electric field heats the plasma, and a hot plasma doesn't sync as well to the RW frequency. As discussed later in section 3.4, electrons and positrons cool in a strong magnetic field by emitting cyclotron radiation, so the heat added by the rotating wall is radiated away within a few seconds after the rotating wall turns off, but rotating wall

compression of an ion plasma requires either laser cooling for positive ions or sympathetic electron cooling for negative ions.

Trivelpiece-Gould (TG) modes are thermally excited modes accessible by a long electron (or positron) plasma in a Penning-Malmberg trap, and Anderegg et al. at UC San Diego demonstrated that Trivelpiece-Gould modes can be excited by applying a rotating wall [113] or by modulating one of the trap electrode voltages at RF frequencies [115]. The modes are observed by driving the plasma at resonant MHz frequencies. The temperature, which peaks at resonant modes, can be measured either by dumping the plasma or by measuring the plasma's thermal emission absorbed by the electrodes. The dispersion relation for TG modes for an electron plasma with mode number $m_\theta > 0$ is [116, 115]:

$$\omega_m \approx \omega_p \left(\frac{r_p}{r_w}\right)(r_w k_z)\left[\frac{1}{2}\ln\left(\frac{r_w}{r_p}\right)\right]^{1/2}\left[1+\frac{3}{2}\left(\frac{\vec{v}}{v_\phi}\right)^2\right], \tag{3.17}$$

where as before r_w is the radius of the wall, r_p is the plasma radius, $v_\phi = \omega_m/k_z$, and $\vec{v} \equiv (k_b T_p/m_e^{1/2})$ gives the dependence on the plasma's temperature T_p. We note that ω_{TG} is always smaller than ω_p.

The Strong Drive Regime

The strong drive regime is a particular implementation of the rotating wall drive wherein the rotation frequency of the plasma synchronizes with the frequency of the applied field, resulting in a linear relationship between the frequency applied and the density of the plasma; see discussion of Fig. 4.8 in Sec. 4.3. This method was discovered by Danielson and Surko at UC San Diego in 2005 [117] and further characterized in 2006 [118]. It was found to work on electron plasmas several centimeters long and over frequencies from a few hundred kHz to 8 MHz [118].

Accessing the strong drive regime can be difficult, as it requires a very close alignment between the magnetic field axis and the plasma axis, and the orientation of the plasma with respect to the rotating wall electrode is important. In November 2015, after scanning many parameters, we developed the procedures to drive plasmas in the strong drive regime in the ALPHA experiment with linearity between density and drive frequencies over the range of 100 kHz to approximately 1 MHz. We don't know yet why the linearity stops at 1 MHz. One possibility is that the internal filters feeding the sinusoidal voltages to the trap alter the phase of high frequency signals on the different sectors of the electrodes so that they are no longer 60° apart.

Analysis of plasma shape and density

The main plasma analysis tool used by ALPHA assumes a cold plasma and solves for the plasma shape and density. It takes as inputs N the number of particles in the plasma, and the outputs of the line-integrated density a, calibrated radius b, and an additional factor n

produced by the Gaussian fit applied to the radial profile imaged on the MCP (refer to Sec. 2.2), along with the shape of the potential well the plasma was confined in. This calculation uses the waterbag method, and is done in a Labview program that calculates the plasma self potential, density profile, bounce frequency, and $E \times B$ drift frequency; the program was updated with the geometry of ALPHA's traps as part of Chukman So's thesis [66] and has been slightly improved as part of the work for this thesis. The results of the self-potential calculation are essential for designing and tuning wells where the plasma's self potential is expected to fill up the well, for example in the shallow wells used for antihydrogen synthesis. A brief summary following the detailed description of the waterbag solver in Ref. [66] is given in this section. We note that in the ALPHA experiment plasmas typically have N in the range of $10^5 - 10^8$ particles, n in the range $10^7 - 10^8 \mathrm{cm}^{-3}$, radii b in the range of $0.3 - 1.5$ mm, and potential well lengths in the range of $0.5 - 5$ cm.

The self-potential of a plasma as a function of radius is defined by Poisson's equation: $\nabla^2\phi(r) = \rho(r)/\epsilon_0$ where $\rho(r)$ is the charge density of the plasma and $\phi(r_w) = V$ is specified by the potentials applied to the walls at radius r_w. The solver assumes azimuthal symmetry, and solves for potentials that are constant along field lines at every radius inside the plasma. To analyze the plasma parameters of a cylindrical plasma, the water bag solver divides the potential into the vacuum potential, which is the potential as a function of radius in the absence of a plasma, and the self-potential which is the potential of the plasma in the absence of externally applied potentials. The algorithm takes as input the trap geometry and electrode potentials and solves for the plasma parameters at different radii of the plasma along the z axis. The solution usually takes about five minutes to complete on a standard desktop computer.

3.4 Cooling Mechanisms for antiprotons, positrons and electrons

Cyclotron Cooling

A non-relativistic charged particle in a magnetic field rotates at the cyclotron frequency ω_c in a circle perpendicular to the magnetic field, illustrated in Fig. 3.3, and radiates energy in the form of photons. The particle's rotation frequency is independent of the particle's velocity and is constant in a static magnetic field:

$$\omega_c = \frac{qB}{m}. \tag{3.18}$$

The particle's larmor radius, or gyroradius, r_L is linearly proportional to the perpendicular velocity $v_\perp$:

$$r_L = \frac{mv_\perp}{qB} = \frac{v_\perp}{\omega_c} \tag{3.19}$$

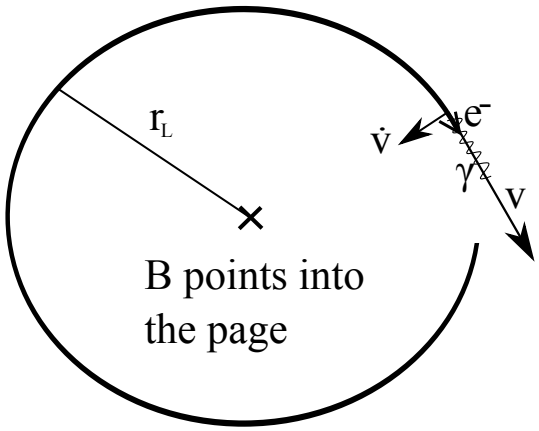

Figure 3.3: Cyclotron motion and radiation of an electron rotating clockwise in a magnetic field pointing into the page.

and it radiates power (P) at the rate given by the Larmor Formula [119]:

$$P = \frac{e^2 a^2}{6\pi\epsilon_0 c^3}, \tag{3.20}$$

where a is the centripetal acceleration of the particle,

$$a = \frac{v_\perp^2}{r} = \frac{qB}{m} v_\perp. \tag{3.21}$$

Cyclotron cooling of a non-neutral plasma was first proposed and analyzed by O'Neil in 1980 [110] and was first achieved experimentally by Malmberg et al. in 1988 [120]. As cyclotron cooling occurs when particles radiate more energy than they absorb from their environment, a cryogenic trap is required to cool a lepton plasma to cryogenic temperatures. Through cyclotron cooling a plasma will approach thermal equilibrium with the trap, at which point the energy radiated matches the blackbody radiation of the trap. Experimentally, however, the plasma temperatures are always at least a few kelvin higher due to other heat sources.

The acceleration of a charged particle in a magnetic field is proportional to its charge-to-mass ratio. Because the power emitted is proportional to the square of the acceleration, an electron radiates power at a rate 4×10^6 times as fast as a proton. The amount of power emitted by an electron in 5 seconds in a 1T field is the same amount emitted by a proton in about 230 days, thus cyclotron cooling is a very useful tool for lepton plasmas but, unless an electromagnetic cavity is employed (as described in the following section), it is a highly impractical method for cooling antiproton or ion plasmas.

Cavity cooling

To calculate the free-space electron cyclotron cooling rate, we start by substituting $v_\perp^2 = 2k_b T/m_e$ into Eq. 3.20 (the Larmour formula) and multiply it by 2/3 to account for collisional

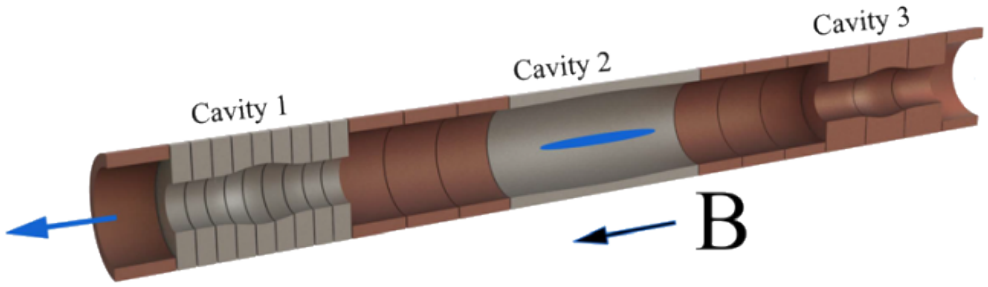

Figure 3.4: Cavity electrodes interspersed with standard cylindrical electrodes in the Penning trap used in the Berkeley experiment. Figure from reference [123].

cooling into the axial degree of freedom by the two perpendicular degrees of freedom:

$$P = \frac{e^2\omega_c^2 k_b T}{3\pi\epsilon_0 c^3 m_e} \tag{3.22}$$

$$P = -\frac{\partial k_b T}{\partial t} \tag{3.23}$$

$$k_b \frac{\partial T}{\partial t} = -\Gamma_0 k_b T, \tag{3.24}$$

$$\rightarrow \Gamma_0 = \frac{2}{3}\frac{e^2\omega_c^2}{3\pi\epsilon_0 m c^3} \tag{3.25}$$

$$\approx 0.26\left(\frac{B}{1\mathrm{T}}\right)^2 \frac{1}{\mathrm{s}} \tag{3.26}$$

with B in units of Tesla.

Purcell demonstrated that theoretically a plasma in resonance with an electromagnetic cavity mode in the trap will have a higher cooling rate [121] Γ defined as:

$$\frac{\Gamma}{\Gamma_0} = \frac{3Q\lambda^3}{4\pi^2 V}, \tag{3.27}$$

with V the volume in which the resonance occurs, λ the wavelength of radiation (approximately 1 cm in a 1T field) and Q the quality factor. A collaboration between the Fajans' group in Berkeley and Hardy and Evetts at the University of British Columbia designed and tested an electromagnetic cavity that resulted in an enhanced cooling rate of $\Gamma = 6\,s^{-1}$ for an electron plasma in a 1T field [95, 122]. Subsequent research by the Fajans' group at Berkeley has demonstrated the ability to effectively cool plasmas via cavity modes at much lower magnetic fields [123]. While the experiment at Berkeley has electrodes specifically designed to hold high-quality cavity modes, shown in Fig. 3.4, it is also possible to find cavity modes at a particular magnetic field strength in a standard cylindrical Penning trap.

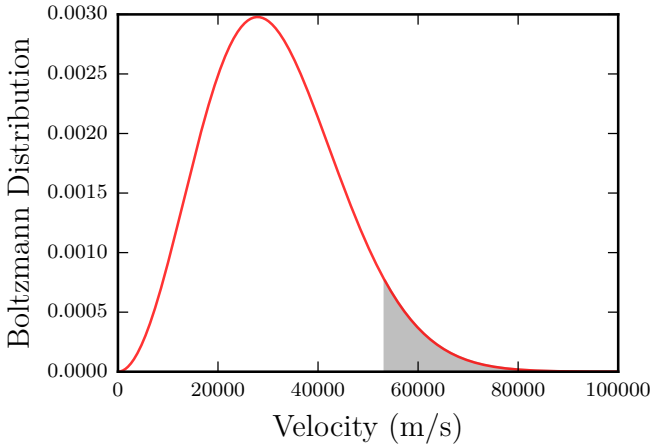

Figure 3.5: Normalized 3d Maxwell-Boltzmann distribution. The shaded region represents 6.3% of the particles that together constitute about 20% of the total energy.

A description of a search for an inadvertant cavity resonance near the center of the ALPHA atom trap is given in chapter 5.

Evaporative cooling

Evaporative cooling (EVC), illustrated in fig 3.6, operates on the Maxwell-Boltzmann distribution of the plasma's temperatures,

$$f(v) = \left(\frac{m}{2\pi k_B T}\right)^{\frac{3}{2}} 4\pi v^2 e^{-\frac{mv^2}{2k_B T}}. \tag{3.28}$$

In the Maxwell-Boltzmann distribution, plotted in Fig. 3.5, there is a long tail where a small percentage of the particles have very high energy. If you remove the particles in the tail, the particles will rethermalize at a lower mean temperature; as an example, in Fig. 3.5, removing 6.3% of the particles would remove 20% of the total energy of the ensemble. Evaporative cooling was first applied to magnetically trapped rubidium-87 atoms by Wieman and Cornell's group [124] and to sodium atoms by Ketterle's group [125] to cool them to the sub-millikelvin temperatures necessary to achieve Bose-Einstein Condensates in 1995. For this achievement they were awarded the 2001 Nobel Prize in physics

For trapped charged particles, evaporative cooling is controlled by lowering at least one side of a potential well barrier until particles escape: the most energetic particles escape first while the least energetic particles remain in the bottom of the trap. Particles escaping along the axis results in cooler axial temperatures; collisions between particles then redistribute the energy to the perpendicular direction while evaporation continues. In ALPHA, evaporative cooling is done over a few hundred ms and the collision time between particles is much

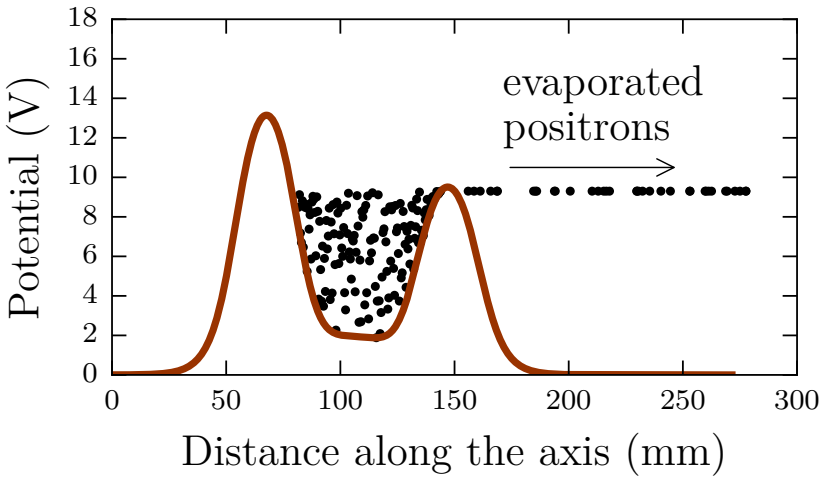

Figure 3.6: An example potential well design to evaporatively cool positrons. The vertical axis, V, is the voltage applied to the electrodes, while the horizontal z-axis is the beamline. The solid brown line shows the uneven potential well used for evaporative cooling in ALPHA and the black dots represent particles.

shorter. Evaporative cooling of antiprotons was developed by the ALPHA collaboration in 2010 [126] and has been used in antihydrogen trapping procedures, along with evaporative cooling of positrons.

There are two main drawbacks of using evaporative cooling as part of antihydrogen synthesis. At the end of the cooling, you have fewer particles with which to make antihydrogen; and second, the density decreases during the evaporation by an amount dependent on the initial conditions. Much time has been devoted on the experiment to find optimal evaporation parameters to give colder antiproton and positron plasma that yield the highest antihydrogen trapping rate. During our 2017 run, we found it was preferable to synthesize without evaporative cooling; we obtained a higher trapping rate with twice as many particles with temperature a few Kelvin higher than we did with plasmas after evaporative cooling. After ELENA is operational in 2021, evaporative cooling may become important again due to the substantially larger number of antiprotons available.

Adiabatic cooling

Adiabatic cooling of an ensemble of particles occurs when the particles are allowed to expand in a way that conserves action, thereby connecting spatial stretching with velocity shrinking. In a slowly varying square well in 1D, $L_m v_m$ =constant, where L_m is the length of the well and v_m the magnitude of the bouncing particle's velocity. To adiabatically cool a plasma, the volume of the potential well confining the plasma must increase. One benefit of adiabatic

cooling is that no particles are lost; however, over time, it was observed that, on the order of a minute or two, the plasma returns to its initial temperature [127]. Adiabatic cooling is thus most effective as a final cooling step just before synthesizing antihydrogen. In the 2017 run, we adiabatically cooled positrons in one dimension just before producing antihydrogen by trapping the positrons in a narrow, deep well for several seconds to have a cold but axially compressed plasma, and then moved them into the "mixing" well. In this shallow well they adiabatically cool by expanding by a factor of three or four along the axis.

Sympathetically cooling antiprotons

Adiabatic cooling and evaporative cooling are methods that work similarly well for leptons and baryons, but neither method is capable of cooling antiprotons from the 5 keV energies we trap them at to the few meV energies needed to synthesize trappable antihydrogen. To provide the majority of the cooling, it is necessary to sympathetically cool the antiprotons by bringing them into thermal equilibrium with cold particles.

Electron cooling of trapped antiprotons was first developed by Gabrielse et al. in 1989 [48] using antiprotons from the Low Energy Antiproton Ring (LEAR), the predecessor to the AD. Electron cooling is suitable for antiprotons because the different particle species have the same charge and thus repel each other by the Coulomb force, allowing them to come into thermal equilibrium via repulsive Coulomb collisions. Due to the large mass difference between electrons and antiprotons, to sympathetically cool antiprotons with electrons with a cooling time on the order of a few seconds, we initially use 90×10^6 electrons to cool approximately 10^5 antiprotons.

Chapter 4

Developing controllable and reproducible non-neutral plasmas

Due to many complications in plasma dynamics, certain plasma systems are hard to precisely control and reproduce. A particular problem for the ALPHA experiment has been the variation in numbers of electrons or positrons; this arises from the challenge of collecting the same number of particles in magnetic and electric fields when experimental conditions fluctuate. For example, the alignment of the electron gun with the magnetic field axis affects how many electrons are transferred into the trap, and as our electron gun is on a vertically moving stick and changes positions between loading plasmas, this orientation can fluctuate. The transfer of positrons from the accumulator to the atom trap is inefficient, with only about 10% of positrons surviving the transfer, and the number transferred also fluctuates on a shot-to-shot basis along with slow drifts tied to the radioactive half-life of the source and efficacy of the moderator. We needed a method to start with a variable number of particles at a variable density and measure out a particular number at a particular density in order to have a reproducible recipe for antihydrogen production. The development detailed in this chapter was motivated by the following theory, and the experimental results were published in [65]. This work comprises the key results of this thesis.

4.1 Conceptual theory for reproducible non-neutral plasmas

As described in the previous chapter, in the zero-temperature limit, a cylindrical non-neutral plasma in a magnetic field rotates at the $E \times B$ frequency f:

$$f = \left(\frac{e}{4\pi\epsilon_0 B}\right) n, \tag{4.1}$$

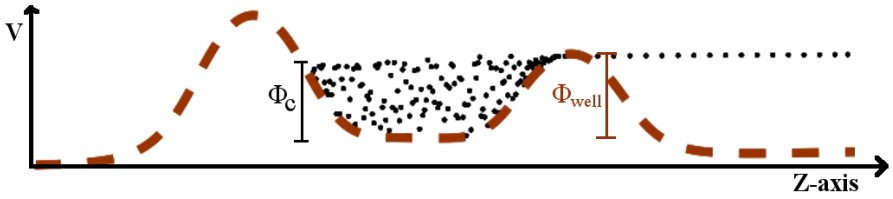

Figure 4.1: When evaporation begins to occur, the space charge ϕ_c is limited by the depth of the potential well ϕ_{well}.

and the self potential of the plasma, ϕ_c is given by (Eq. 3.3):

$$\phi_c = \frac{ner_p{}^2}{4\epsilon_0}\left[1 + 2\ln\left(\frac{r_w}{r_p}\right)\right]. \tag{4.2}$$

We approximate the plasma as a cylinder of radius r_p filled with N charges at density n:

$$N = \pi n r_p^2 L \rightarrow r_p^2 = \frac{N}{\pi L n}. \tag{4.3}$$

Substituting this into Eq. 4.2, we solve for ϕ_c in terms of N and n:

$$\phi_c = \frac{Ne}{4\pi\epsilon_0 L}\left[1 + \ln\left(\frac{r_w^2 n\pi L}{N}\right)\right]. \tag{4.4}$$

We observe in equation 4.2 that the number of particles, the plasma density and the space charge are a unique set of plasma parameters. This means if we control two of these parameters the third parameter will be uniquely defined. As described in the discussion on evaporative cooling, the plasma begins to evaporate when the potential well is too shallow to hold all of the plasma.

If we load more particles than we need, for example 4-6 million particles when we desire 3 million, we reduce the self potential to an exact level by making the potential well shallow enough that the plasma begins to evaporate. As soon as evaporation occurs we know that the magnitude of the self-potential ϕ_c of the plasma equals the depth of the well, indicated in Fig. 4.1. Thus to control the plasma parameters we use evaporative cooling to set the space charge, with emphasis on " evaporation" not "cooling."

4.2 Developing SDREVC

As mentioned in the previous chapter, the Strong Drive Regime (SDR) is an excellent way to control the density of a plasma. To control the set of plasma parameters we have to simultaneously control the density and the space charge; this was the main developmental challenge of this thesis. Because it is the simultaneous application of the strong drive regime and evaporative cooling we called this stabilization process SDREVC. The experimental

hardware requirements to access SDREVC are a Penning trap with a rotating wall electrode with at least four and preferably (see Sec. 3.3) six sectors, suitable electrode lengths to allow fine modifications of the well shape (for example, electrodes with length equal to the radius), at least a 1T magnetic field aligned with the axis of the trap (and hence the axis of the plasma), ultra-high vacuum conditions inside a cryogenic trap, and, of course, a source for electrons or positrons.

The first step in developing SDREVC was to find an appropriate well shape in which the plasma was in the strong drive regime. We tried a range of well lengths with the rotating wall electrode at one end until we accessed the strong drive regime at frequencies up to nearly 1 MHz. To determine if the plasma was in the strong drive regime we looked for two conditions: first we required a linear relationship between the line integrated density of the image of the plasma and the frequency at which we drive the rotating wall, and second we required the waterbag solver's calculated rotation frequency of the plasma to be within approximately 10% of the driving frequency. The difference in the applied and the actual rotation frequencies is referred to as the "slip," and ideally is kept as minimal as possible. To determine if evaporative cooling was happening at a particular well depth, we only had to compare the number of particles at the beginning of the step and the number at the end; if we lost particles, the plasma had clearly evaporated.

While SDR and EVC can be performed at the same time, tuning the potential well can be difficult as they have competing side effects. The rotating walls heats the plasma, while evaporative cooling lets the hottest particles escape. Additionally, evaporative cooling causes the density to decrease, while for SDREVC to work the rotating wall needs to control the plasma density.

Figure 4.2 is an example of the magnetic field and the initial and final electric potentials used to perform SDREVC on our positron plasmas, resulting in about 3 million positrons at the end. We ramp the potential well from its initial to final state in 10-20 seconds while continuously applying the rotating wall. Naturally, wells that let particles evaporate must be biased; in this case the well is raised up, as positrons will fall down to the ground potential after evaporating from a positive bias. Worth noting is that SDREVC worked even while the plasma was in a gradient magnetic field; there is a gradient field in this case because in the atom trap, while there is a static 1T field provided by the Carlsberg magnet, we ramp up additional solenoids temporarily to increase the field to 3T, but the length of the 3T field is limited.

Tuning the well, for example the one shown in Fig. 4.2, involves adjusting the length of the well, the axial distance from the rotating wall electrode (the rotating wall electrode should overlap with the end of the plasma), the depth of the well and the overall shape of the well. The initial potential well should be such that the plasma is in the strong drive regime. The well should be modified so that the well as more shallow but still contains the whole plasma. Next, one side of the well should be lowered until the plasma starts to evaporate; at this point one has to pay close attention to whether the density of the plasma is still in the strong drive regime or not; this can be found by taking data points at three different frequencies and checking the linearity of the densities. The first SDREVC potential well had

to be modified dozens of times before a satisfactory well was found. During the first attempts to simultaneously drive the plasma in the strong drive regime while evaporating the plasma, all of the plasma disappeared, and subsequent attempts produced results that varied between controlled density and no evaporation and evaporation but uncontrolled expansion. After many trial-and-error measurements and modifications, an optimal well design was found.

The shallow wells needed when we want only a few million particles, as in Fig. 4.2, are particularly sensitive to slight differences in the well shape or distance from the rotating wall electrode. SDREVC wells for 10 million particles or more are relatively straightforward to find: usually after finding a well where the plasma is in the strong drive regime, if we lower one side of the well the plasma will be in the SDREVC regime. Typically we lower the side opposite the rotating wall electrode although it also worked when we lowered the potential on the rotating wall electrode. As the strong driver regime is accessible in plasmas with a variety of lengths, SDREVC is also accessible in plasmas with a variety of lengths. The combination of the potential well shape, axial displacement with respect to the rotating wall electrode, and amplitude and frequency of the rotating wall drive determine the success (or failure) of SDREVC; these parameters remain to be fully explored.

4.3 Characterizing the reproducibility of SDREVC

Once an appropriate well shape and suitable rotating wall parameters were obtained, we tested whether SDREVC gives us reproducible plasmas for a large range of initial plasma conditions. The original goal was to develop a procedure that creates plasmas with specific densities and numbers of particles regardless of the initial conditions, so we prepared plasmas with a large range of initial numbers of particles and densities and applied SDREVC for 20 seconds at a particular well depth and RW frequency. We prepared the plasmas with different numbers by loading a large number of electrons and then using the ekick method described in Chap. 2 to reduce the number of particles. We prepared plasmas with different densities by driving the plasma in the strong drive regime at different frequencies before starting SDREVC. For comparison, we also measured the final conditions if we only evaporated the plasma without applying a rotating wall. The results are shown in Figs. 4.3 and 4.4; each data point represents the average of twenty measurements, and for these plots the error bars were within the size of the data point markers.

The number of particles were measured with a Faraday cup and the density is the line-integrated density of the gaussian fit of MCP images, as discussed in Chap. 2. The numerical densities, calculated with the waterbag solver, are on the order of 10^{-8}cm^{-3}; calculated densities are not plotted here due to the large number of data points averaged over in the plots and the relative unimportance of the absolute value of the density. Our antihydrogen production methods are typically optimized empirically, thus relative changes in density are important and the absolute density is not very important.

We observe in Fig. 4.3 that the number of particles and density after SDREVC is consistent for a wide range in the initial number of particles, and in Fig. 4.4 that the density

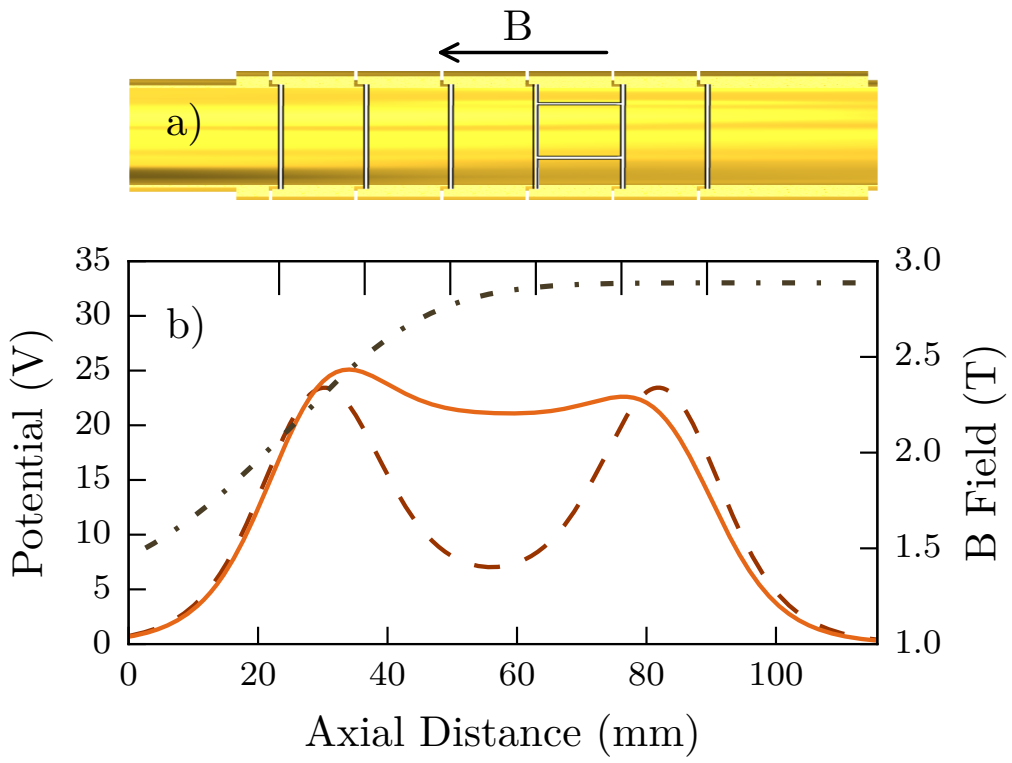

Figure 4.2: a) Partial schematic of one of ALPHA's Penning-Malmberg traps, showing the axial magnetic field **B**, seven of the electrically-isolated cylindrical electrodes, and one rotating wall electrode (fifth in from the left) with six isolated azimuthal sectors; the inner radius of the electrodes is 14.8 mm. b) Typical initial (dashed) and final (solid) electrostatic potentials used in the stabilization procedure, and the axial magnetic field (dot-dash). Figure from reference [65].

after SDREVC is consistent for a wide range of initial densities. We noticed in some circumstances though that if the initial density was too high, too many particles are evaporated at the beginning of SDREVC before the plasma settles at the density assigned by the rotating wall. In cases where the initial particle load is too dense, we apply a preliminary rotating wall to the plasma for a few seconds before turning on SDREVC.

An additional test of the stability was to compare the fluctuations over the different initial particle loads with the noise of the FC detector. The noise was measured by triggering the Faraday cup detecter 20 times and finding the average and standard deviation of the measurements. Figure 4.5 shows that the fluctuation in post-SDREVC values is at the noise floor of the detector.

We further compared the results from SDREVC with the results from performing SDR and EVC sequentially, as summarized in Fig. 4.6. Repeatedly applying SDR and EVC

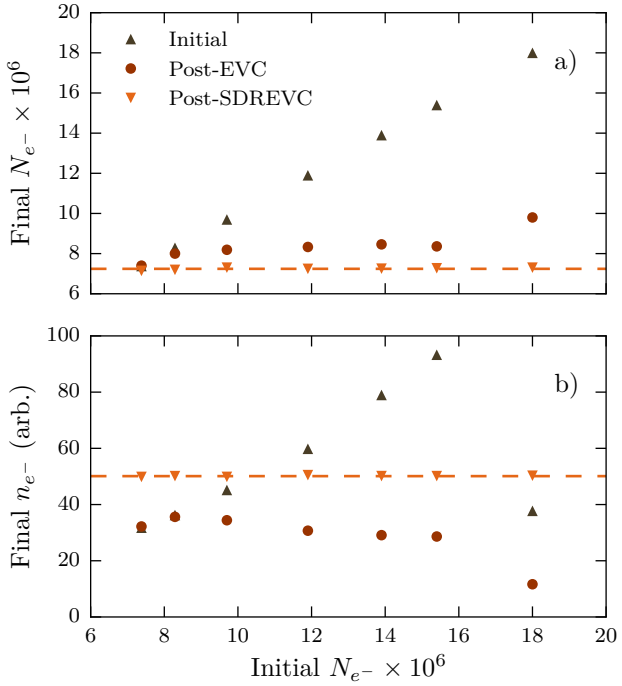

Figure 4.3: Initial (▲), post-EVC (●), and post-SDREVC (▼) measurements of the number of particles (a) and plasma density (b) as a function of the initial number of electrons; the orange dashed lines mark the average post-SDREVC values. Figure from reference [65].

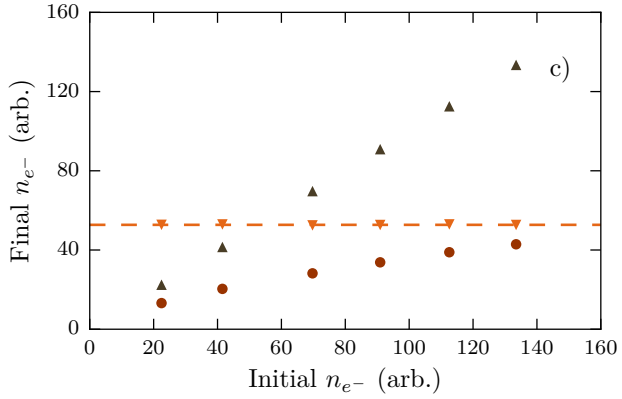

Figure 4.4: Initial (▲), post-EVC (●), and post-SDREVC (▼) measurements for the final plasma density as a function of the initial density. The density refers to the results of an axially-integrated MCP diagnostic and has arbitrary units. The orange dashed line marks the average post-SDREVC value. Figure from reference [65].

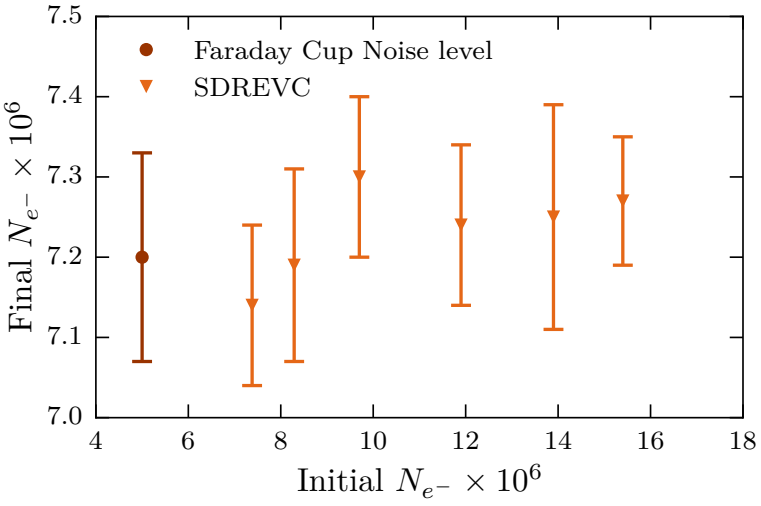

Figure 4.5: Magnified plot of the number of particles with SDREVC (▼) and the noise level of the Faraday cup detector (●).

sequentially brings the plasma closer to equilibrium than just applying one and then the other, but the final N_{e^-} and n_{e^-} are noticeably susceptible to changes in the initial conditions. Only the simultaneous application of both techniques can uniquely specify the parameters in equation 4.2. The data was taken by alternating the measurements starting with EVC and those starting with the SDR. Each of the sequential measurement data points are the average of five measurements.

Having confirmed that SDREVC produces a stable plasma for a wide range of initial conditions, the next step was to probe the range of numbers and densities we can obtain after SDREVC. These ranges are shown in Figs. 4.7 and 4.8. As previously mentioned, in the ALPHA apparatus the strong drive regime is accessible up to only 800 kHz, which limits the range of densities we can control. We haven't yet found a limit to the maximum number of particles that can be stabilized via SDREVC; a technical limit for characterization studies when searching for the maximum number is that a plasma with hundreds of millions of particles may extend beyond the edge of the Faraday Cup or MCP and not be accurately counted. For these plots, Figs. 4.7 and 4.8, the final numbers and densities are in the ranges of $7 \times 10^6 < N_{e^-} < 70 \times 10^6$ and $10^{14} < n_{e^-} < 1.3 \times 10^{15}\,\mathrm{cm}^{-3}$.

We also calculated how the plasma parameters should scale according to equation 4.2. At constant density $n = n_0$, the number of particles N, normalized at some arbitrary value

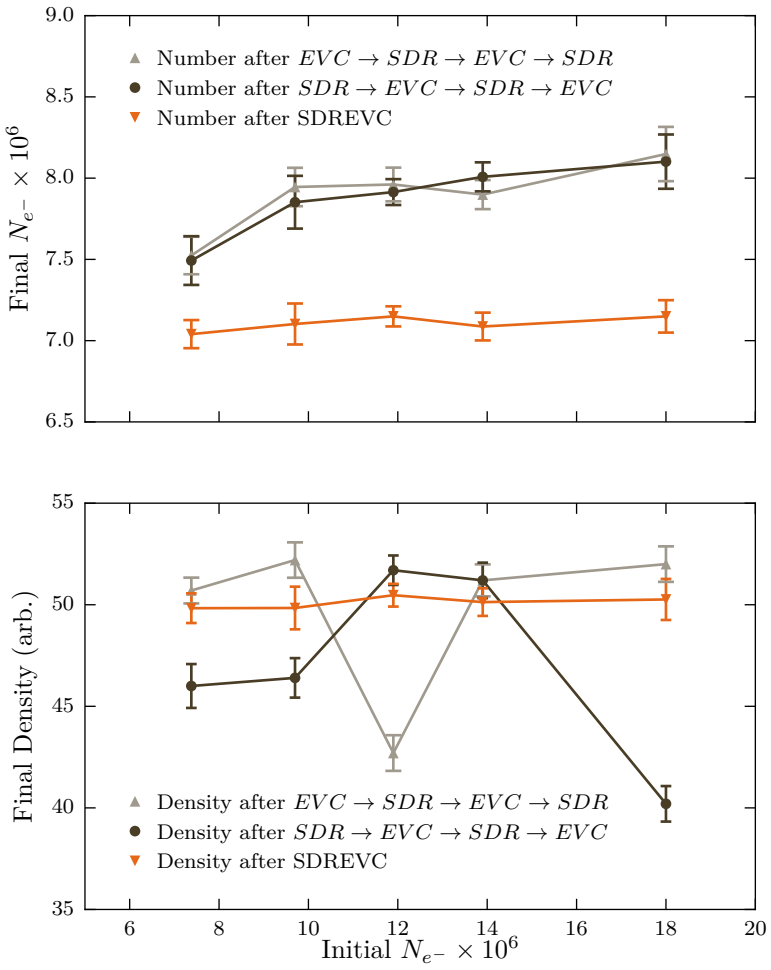

Figure 4.6: Sequential EVC and SDR repeated twice (▲), Sequential SDR and EVC repeated twice (●), and SDREVC (▼) measurements for a range of initial numbers of particles. Only the simultaneous SDREVC process set both the final number and density to values independent of the initial values. Figure taken from Ref. [65].

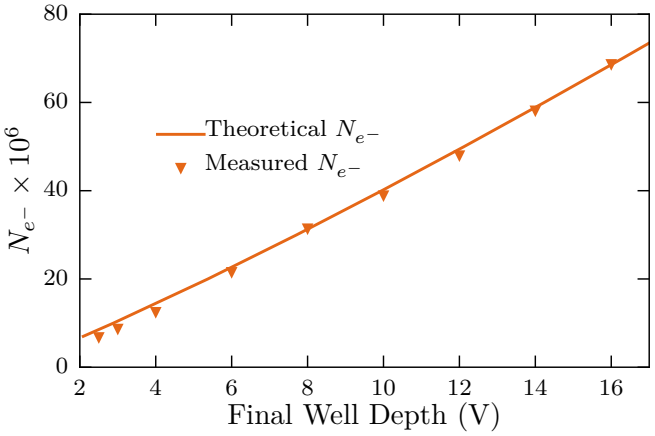

Figure 4.7: Measured number of electrons N_{e^-} (▼) retained in different well depths when driven with a 700 kHz rotating wall. The theoretical line corresponds to Eq. 4.8 with ϕ_c normalized at 8V. Figure from reference [65].

$N_0 = n\pi L r_{p_0}^2$, scales with the space charge ϕ_c, normalized at a corresponding ϕ_{c_0}:

$$\phi_c = N\left(1 + \ln\left(\frac{R_w^2 n\pi L}{N}\right)\right) \tag{4.5}$$

$$= N\left(1 + \ln\left(\frac{R_w^2}{r_{p_0}^2}\frac{N_0}{N}\right)\right) \tag{4.6}$$

$$\phi_{c_0} = N_0\left(1 + \ln\frac{R_w^2}{r_{p_0}^2}\right) \tag{4.7}$$

$$\phi_c = \phi_{c_0}\left(\frac{N}{N_0}\right)\left(\frac{1 + \ln\left(\frac{R_w^2}{r_{p_0}^2}\frac{N_0}{N}\right)}{1 + \ln\left(\frac{R_w^2}{r_{p_0}^2}\right)}\right). \tag{4.8}$$

The logarithmic contributions in equation 4.8 are small relative to N/N_0 so the relationship is expected to be close to linear. This was observed experimentally and is plotted in Fig. 4.7.

We studied the behavior of SDREVC as a function of the initial number of particles, plasma radius, and density with a range of rotating wall frequencies. These are summarized in Fig. 4.8. The frequency dependency of r_p is the solution to the differential equation (from Eq. 4.2):

$$\frac{\mathrm{d}r_p}{\mathrm{d}f} = -\frac{r_p}{2f}\left[1 + \frac{1}{2\ln(R_w/r_p)}\right], \tag{4.9}$$

but, as before, the logarithmic contribution is small so the solution r_p scales as

$$r_p = r_{p_0}\sqrt{f_0/f}. \tag{4.10}$$

The solution plotted for r_p in Fig. 4.8b is normalized at one of the central data points along the linear slope, at $f_0 = 450$ kHz and $r_{p_0} = 0.33\,\text{mm}$.

The number of particles can be scaled theoretically by inserting the solution for r_p into Eq. 4.3 along with the value for n scaled by Eq. 4.1:

$$N = r_{p_0}\sqrt{\frac{f_0/f}{n}}L \tag{4.11}$$

$$= r_{p_0}\sqrt{\frac{f_0/f}{L}}\left(\frac{4\pi\epsilon_0 B f}{e}\right). \tag{4.12}$$

This is plotted in Fig. 4.8a with the same normalization values used for the plot for r_p : $f_0 = 450$kHz, $r_{p_0} = 0.33$ mm, and $n(450\text{kHz}) = 8 \times 10^{14}\text{cm}^{-3}$. The length is constant as the only parameter that changes is the rotating wall frequency. The density in Fig. 4.4c is linear with the frequency up to about 800 kHz in agreement with Eq. 4.1: $n \equiv C \times f$ with fundamental constants and the magnetic field represented by C.

The flexibility in selecting a particular number or density makes SDREVC a versatile tool for any Penning-trap based cold electron or positron experiment. When we try to optimize our antihydrogen production schemes, we often want to vary the number of particles or the density. Usually we use SDREVC at a particular well depth to determine the number of particles, and if a different density is desired we apply a separate rotating wall potential to the plasma in the strong drive regime after finishing SDREVC. As it is relatively easy to vary the well depth of an SDREVC well, we can efficiently scan different numbers and densities with the assurance that whatever optimal parameters we find, we can continue to make plasmas with the same parameters indefinitely.

Long-term stability of plasmas after SDREVC

SDREVC was implemented in our standard antihydrogen trapping sequences within a few weeks of being discovered. When running the experiment, we repeat a set of "baseline" measurements on an almost daily basis. After SDREVC was developed, we included measurements just after loading the particles, pre-SDREVC, and post-SDREVC in the set of baseline measurements. The brown triangles in Fig. 4.9a show the large variation in number of particles for electrons in the catching trap before SDREVC was implemented, and the orange triangles show the remarkable stability in the number post-SDREVC. In the case, the number of particles loaded pre-SDREVC, which would be marked by brown triangles, was too high to include on the plot. Figures 4.9b and 4.9c also show a large variation in the number of particles pre-SDREVC, again marked with brown triangles, and a high level of stability post-SDREVC. As mentioned in the caption, the arrows point to two occasions where the positron moderator failed, which lowered the pre-SDREVC count too much which inevitably lowered the post-SDREVC numbers. The numbers of particles pre-SDREVC and post-SDREVC recovered to their normal levels after a new moderator was grown (see Sec. 2.2 for a discussion on the moderator).

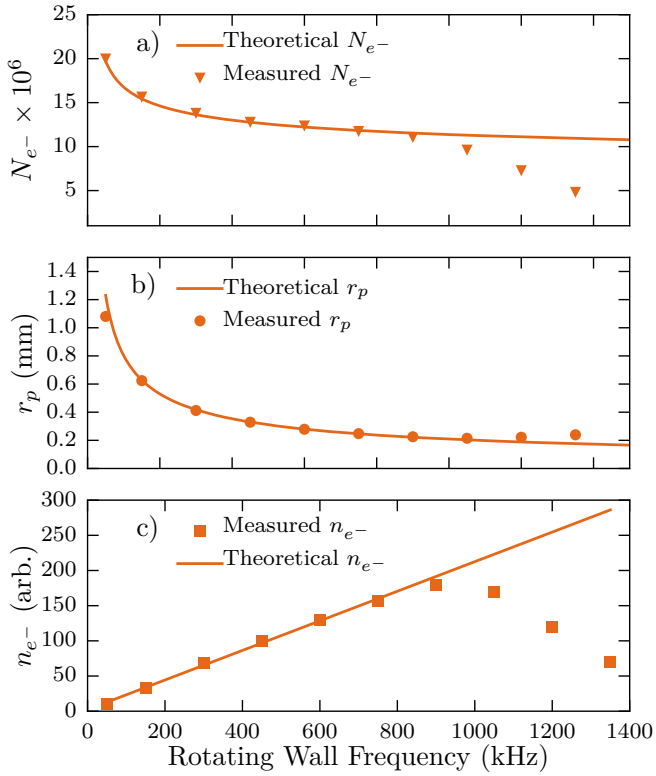

Figure 4.8: Measured numbers N_{e^-} (▼), densities n_{e^-} (■), and radii r_p (●); predicted values, normalized at 450 kHz, are indicated by the lines calculated in equations 4.8, 4.1, and 4.10 respectively. a) Number of electrons retained in different well depths when driven with a 700 kHz rotating wall; b) plasma radius and plasma density; and c) number of electrons retained in a 4V potential well as a function of the rotating wall frequency. Figure from reference [65].

Figure 4.9 shows that we can load different plasmas every day for several months and process it with SDREVC to get a nearly identical plasma every time. It was also observed the next year, after an intervention on the experiment, that the results after SDREVC were also the same. The long-term stability of SDREVC means that with it, as long as we begin with at least 10% more particles than we need after SDREVC, we can apply SDREVC and obtain the same plasma parameters we had during the previous month or year.

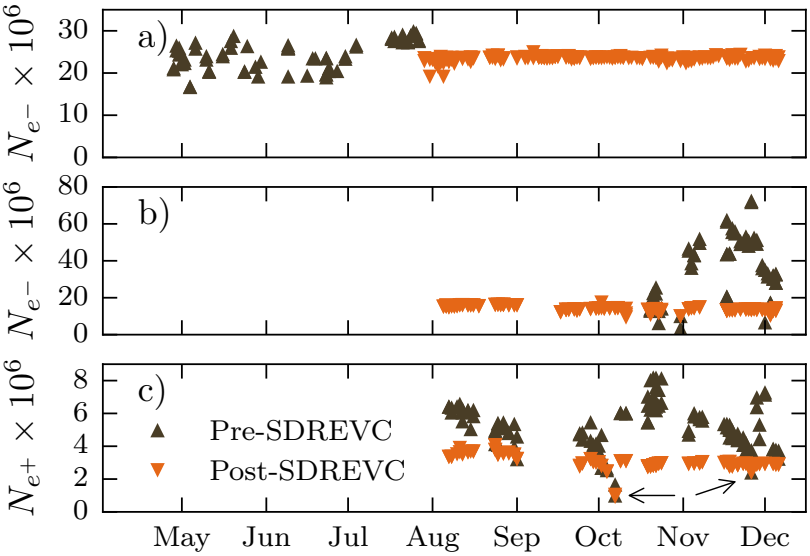

Figure 4.9: Pre- (▲) and post- (▼) SDREVC measurements: a) plasma electron number N_{e^-} in the catching trap; b) plasma electron number N_{e^-} in the atom trap; and c) plasma positron number N_{e^+} in the atom trap. SDREVC was implemented at the end of July 2016, so only pre-SDREVC data are shown prior to that date. Beginning in August, the pre-SDREVC numbers in a) are off scale. The arrows in c) indicate instances where the positron moderator efficiency decreased and the number of pre-SDREVC positrons dropped below the desired post-SDREVC value; the number was recovered by regrowing the moderator. Figure and caption taken from [65].

4.4 Theoretical and Experimental Relationship between variations in particle numbers and plasma density during SDREVC

In the theoretical study of the relationship between a variation in the particle number and the plasma density, we start with equation 4.4:

$$\phi_c = \frac{Ne}{4\pi\epsilon_0 L}\left[1 + \ln\left(\frac{R_w^2 n\pi L}{N}\right)\right]. \tag{4.13}$$

SDREVC is not perfect, meaning that there will be some variation in the final number of particles or final density, so we wish to find the scaling between the fractional change in the number of particles and the fractional change in the density:

$$\frac{\Delta N}{N} = x \times \frac{\Delta n}{n}. \tag{4.14}$$

To find this we solve for $\Delta\phi_c$ by solving for $f(N+\Delta N, n+\Delta n) - f(N,n)$. For simplicity, set $A = \frac{e}{4\pi\epsilon_0 L}$ and $D = R_w \pi L$ so that equation 4.1 reads

$$\phi_c = AN\left[1 + \ln\left(\frac{nD}{N}\right)\right], \tag{4.15}$$

then calculate $\Delta\phi_c$:

$$\Delta\phi_c = A(N+\Delta N)\left(1 + \ln\left(\frac{(n+\Delta n)D}{N+\Delta N}\right)\right) - AN\left(1 + \ln\left(\frac{nD}{N}\right)\right) \tag{4.16}$$

$$= A(N+\Delta N)\left(1 + \ln(n+\Delta n) + \ln B - \ln(N+\Delta N)\right) - AN\left(1 + \ln\left(\frac{nD}{N}\right)\right) \tag{4.17}$$

$$= A(N+\Delta N)\left(1 + \ln\left(1+\frac{\Delta n}{n}\right) - \ln\left(1+\frac{\Delta N}{N}\right) + \ln\frac{nD}{N}\right) - AN\left(1 + \ln\frac{nD}{N}\right) \tag{4.18}$$

$$\approx A(N+\Delta N)\left(1 + \frac{\Delta n}{n} - \frac{\Delta N}{N} + \ln\frac{nD}{N}\right) - AN\left(1 + \ln\left(\frac{nD}{N}\right)\right) \tag{4.19}$$

$$= A(N+\Delta N)\left(\frac{\Delta n}{n} - \frac{\Delta N}{N}\right) + A\Delta N\left(1 + \ln\frac{nD}{N}\right) \tag{4.20}$$

$$\approx AN\left(\frac{\Delta n}{n} - \frac{\Delta N}{N}\right) + A\Delta N\left(1 + \ln\frac{nD}{N}\right). \tag{4.21}$$

The value of ϕ_c is determined by the EVC part of SDREVC, so we set $\Delta\phi_c = 0$. Hence:

$$\Delta N\left(1 + \ln\frac{nD}{N}\right) = \Delta N - N\frac{\Delta n}{n} \tag{4.22}$$

$$\frac{\Delta N}{N}\ln\frac{nD}{N} = -\frac{\Delta n}{n} \tag{4.23}$$

$$\frac{\Delta N}{N} = -\frac{1}{\ln\frac{nD}{N}}\frac{\Delta n}{n}. \tag{4.24}$$

Inserting in experimental values of $r_w = 16.8$ mm and $r_p = 0.33$ mm,

$$\ln\frac{nD}{N} = 2\ln\left(\frac{R_w}{r_p}\right) \tag{4.25}$$

$$= 7.86, \tag{4.26}$$

$$\frac{1}{7.86} = 0.13, \tag{4.27}$$

thus,

$$\frac{\Delta N}{N} = -0.13\frac{\Delta n}{n}. \tag{4.28}$$

Frequency	Number	density (arb.)
50	20×10^6	10.4
300	13.8×10^6	68.2

Table 4.1: Parameter values from figure 4.8.

To compare this estimated theoretical dependence with experimental data, we selected data points from Fig. 4.8 at 50 kHz and 300 kHz. These data points correspond to the same potential well depth (respecting the $\Delta\phi_c = 0$ condition) for our experiment.

We calculate if the change in number matches the prediction for $\Delta N/N$:

$$< N > = \frac{20 + 13.8}{2} = 16.9 \tag{4.29}$$

$$\Delta N = 20 - 13.8 = 6.2 \tag{4.30}$$

$$< n > = \frac{10.8 + 68.2}{2} = 40 \tag{4.31}$$

$$\Delta n = 10.8 - 68.16 = -57.4, \tag{4.32}$$

then we calculate the scaling factor between $\Delta n/ < n >$ and $\Delta N/ < N >$:

$$\frac{\Delta n}{n} = -1.435 \tag{4.33}$$

$$\frac{\Delta N}{N} = 0.11 (\text{experiment}) \tag{4.34}$$

$$-0.144 \times (-0.6) = 0.19 \, (\text{theoretical scaling factor}) \tag{4.35}$$

$$\frac{\Delta N}{N} = 0.37 \, (\text{experimental scaling factor}) \tag{4.36}$$

We see that the experimental variation in the number of particles matches the predicted variation to within a factor of two. Considering a jitter in post-SDREVC density, even if the plasma's rotation rate varies by 10% from the applied rotating wall field, the number of particles at the end of SDREVC will only vary by about 2%. The plasmas have been observed to not synchronize exactly with the RW due to other forces that drive its expansion, but we see that fluctuations in the number are much smaller than fluctuations in the density, so density fluctuations should have a negligible effect on the post-SDREVC number.

4.5 SDREVC theory extrapolated to non-zero temperatures

Non-zero temperature theory for non-neutral plasmas in Penning traps

Stabilization by applying SDREVC was motivated by the model described in Chap. 3 for a non-neutral plasma in the zero-temperature limit. Its success in experiments with non-zero temperatures suggests that temperature effects are negligible up to a certain point. Our goal in this section is to first compute analytically whether the number of particles or plasma density will change substantially at non-zero temperatures. Experimentally, we measured plasma temperatures in the range of 100-300K after doing SDREVC. The plasma temperature is something we do not control, and it is important to know if variations in plasma temperatures will result in variations in the density or the number of particles. We compare existing theories for zero-temperature and non-zero temperature non-neutral plasmas to understand at what temperature the models deviate from each other; the following derivations comprising equations 4.37-4.43 are taken from Prasad and O'Neil's paper [128], followed by additional calculations completed as part of this thesis.

The distribution function for an electron plasma trapped in a conducting cylinder is given by

$$f(n) = n_0\Big(\frac{m_e}{2\pi k_b T}\Big)^{\frac{3}{2}} \exp\Big[-\frac{1}{k_B T}\Big(\frac{m_e v^2}{2} - e\phi(r,z) - \omega p_\theta\Big)\Big], \tag{4.37}$$

where ϕ, $m_e, -e$, and $\vec{v}$, correspond respectively to the electric potential, electron mass, charge, and velocity.

Substituting $\Omega = \frac{eB}{m}$ and $p_\theta = mv_\theta r - \frac{er^2B}{2}$, we obtain

$$f(n) = n_0\Big(\frac{m_e}{2\pi k_b T}\Big)^{\frac{3}{2}} \exp\Big[-\frac{1}{k_B T}\Big(\frac{m_e}{2}(\vec{v_e} - \omega r\hat{\theta})^2 - e\phi(r,z) + \frac{m_e}{2}\omega(\Omega-\omega)r^2\Big)\Big]. \tag{4.38}$$

The assumptions given in Ref. [128] are that the diamagnetic contributions are inconsequential due to the small ratio of v/c, that the electrode radius is much larger than the plasma radius, and that $\phi(r,z)$ is zero at the origin. We notice that in a large magnetic field (and hence large Ω), the exponential dependence of $-\frac{1}{k_b T}\omega(\Omega-\omega)r^2$ causes $f(n)$ to fall off as r increases.

Applying Poisson's equation,

$$\nabla^2\phi = \rho\epsilon_0, \tag{4.39}$$

to equation 4.38 and integrating over $\vec{v}$ assuming spherical symmetry, we have,

$$\frac{1}{r}\frac{d}{dr}r\frac{d\phi}{dr} + \frac{d^2\phi}{dz^2} = \frac{e}{\epsilon_0} \times n_0 \exp\Big[-\frac{1}{k_B T}\Big(-e\phi(r,z) + \frac{1}{2}m_e\omega(\Omega-\omega)r^2\Big)\Big]. \tag{4.40}$$

To simplify the expression $f(n)$, we substitute:

$$\begin{aligned}
\psi &= \frac{e\phi}{k_B T} - \frac{m\omega(\Omega-\omega)r^2}{2k_B T} \\
\rho &= \frac{r}{\lambda_D} \\
\xi &= \frac{z}{\lambda_D} \\
\lambda_D &= \left(\frac{\epsilon_0 k_b T}{n q_e^2}\right)^{\frac{1}{2}} \\
\gamma &= \frac{2\epsilon_0 m_e \omega(\Omega-\omega)}{n_e q_e^2} - 1
\end{aligned} \tag{4.41}$$

Thus, in terms of ψ, Poisson's equation is now:

$$\frac{1}{\rho}\frac{d}{d\rho}\rho\frac{d\psi}{d\rho} + \frac{d^2\psi}{d\xi^2} = e^{\psi} - 1 - \gamma. \tag{4.42}$$

Variables that we assume are known are: $n_1, T_1, \omega_D, \Omega_c, B, r_w$, and ϕ_c. We ignore the z dependence in equation 4.42 by assuming an infinitely long plasma (plasma lengths are usually at least 50 times their radii), which gives the equation

$$\frac{1}{\rho}\frac{\partial}{\partial\rho}\left(\rho\frac{\partial\psi}{\partial\rho}\right) = e^{\psi} - 1 - \gamma. \tag{4.43}$$

We then have to solve the system of equations

$$\begin{aligned}
\frac{\partial\psi}{\partial\rho} &= \alpha \\
\frac{\partial\alpha}{\partial\rho} &= e^{\psi} - 1 - \gamma - \frac{\alpha(\rho)}{\rho}
\end{aligned} \tag{4.44}$$

with initial conditions $\psi(0) = 0$ and $\alpha(0) = 0$.

To find a value for the central density n_0 in a non-zero temperature plasma, we first rearrange the equation for γ in equation 4.41 to obtain the density as a function of γ and the frequency:

$$n(\gamma, f) = \frac{2\epsilon_0 m_e 2\pi\Omega - 2\pi f}{(\gamma+1)q_e^2} \tag{4.45}$$

we insert the value of ϕ_c from equation 4.2 in place of ϕ in the ψ equation (see Eq. 4.41). Let the result be denoted $\psi_{desired}$:

$$\psi_{desired} = \frac{e\phi_c}{k_B T} - \frac{m\omega(\Omega-\omega)r^2}{2k_B T}. \tag{4.46}$$

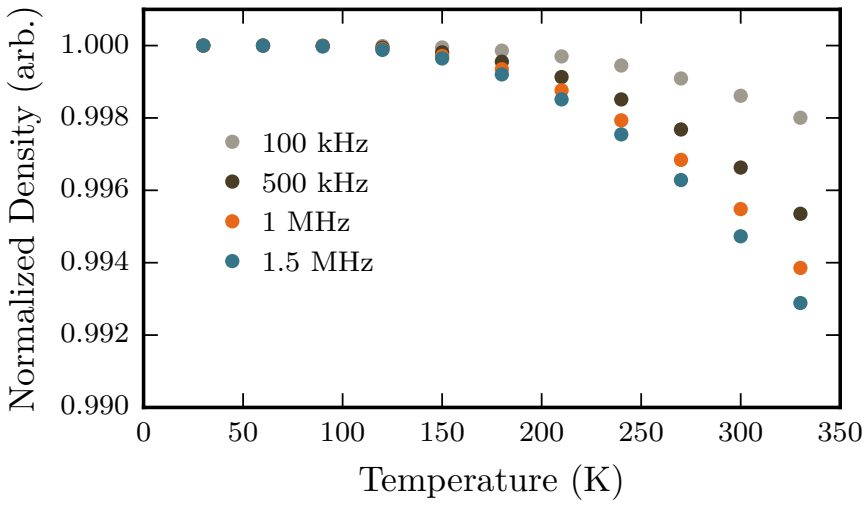

Figure 4.10: Electron plasma density is plotted as a function of temperature for different rotating wall frequencies.

Mathematica Calculation

We evaluated these functions in Mathematica to find the density and number of particles at different temperatures; example code is included in the appendix. The author notes that Dr. Matthias Reinsch at Berkeley offered extended help in implementing this calculation in Mathematica and resolving evaluation errors. First we defined a function whose output at a particular T, f, γ is the solution to equation 4.44, found by the NDSolve function in mathematica. We then define $\psi_{desired}$ as equal to the solution for ψ in the differential equation 4.44 at the wall of the trap, for a plasma with specific density n_0, T, and ϕ_c:

$$\psi_{desired} = -\frac{e^2 n_0 r_p^2}{4\epsilon_0 k_B T}\left(1 + 2\ln\frac{R_w}{r_p}\right) - \frac{m\omega(\Omega-\omega)r_p^2}{2k_B T}, \tag{4.47}$$

and used the FindRoot function in Mathematica to find the value of the density γ and from there calculate the finite-temperature density distribution. The FindRoot function searches for a numerical root of the function within a given range; in this case we search for gamma in the range of -15 to $+15$. In this case we used 10^γ to search for the root, because of the exponential nature of the differential equation.

The value of γ which solves 4.43 is then used in the density equation 4.45 along with some given frequency. We plotted the variation in the plasma density for $30 < T < 300$ for rotation frequencies of 100 kHz, 500 kHz, 1 MHz, and 1.5 MHz, shown in Fig. 4.10. We observe that at higher rotation frequencies, the density is more sensitive to variations in the temperature, but even over this temperature range the change was insignificant, less than 1%.

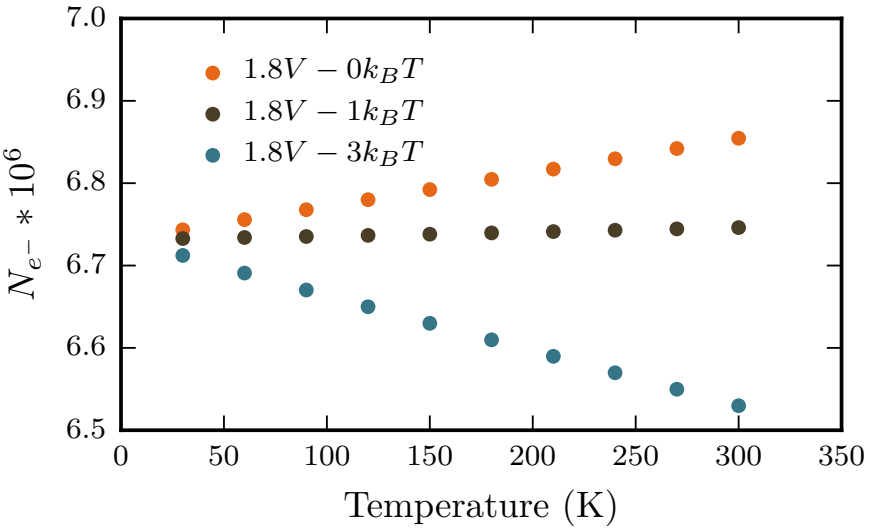

Figure 4.11: The calculated numbers of electrons, Ne^-, is plotted as a function of temperature The curves corresponds to different values of thermal energy kT.

We also integrated over the density distribution out to the wall of the trap to calculate the total number of particles remaining in the plasma, taking into account that ϕ_c may not completely fill up the well: the actual ϕ_c may be a few factors of k_BT below the depth of the well. We considered a well depth used for positron SDREVC and plotted the variations in number as a function of temperature for $\phi_c = 1.8V, \phi_c = 1.8V - k_BT$, and $\phi_c = 1.8V - 3k_BT$, in Fig. 4.11:

Curiously, for the case of $\phi_c - k_BT$, the effect of increasing the temperature is mostly canceled by the shallower well depth, and the number of particles remained constant. For the other cases, the number at $300K$ remained within 3% of the number at $30K$, so the effect of temperature variations on N is also insignificant for parameters relevant to this study.

The finite temperature calculations demonstrate that temperature fluctuations have an insignificant effect on the plasma density and number of particles during SDREVC in the temperature ranges relevant to our experiment.

Chapter 5

Precision measurements on antihydrogen and related plasma physics studies

5.1 Increasing the trapping rate by a factor of ≈ 20

ALPHA's higher trapping rate and accumulation success are described in reference [129]. This section outlines the plasma-related developments that contributed to the higher trapping rate.

Autoresonant antihydrogen synthesis

At the beginning of the 2016 experimental run at ALPHA, our average trapping rate was usually slightly less than 1 atom per trapping cycle, with each cycle lasting about six minutes. Physics measurements were obtained by repeating the same measurement many times, but the drifts in experimental parameters, such as the magnetic field, combined with the desire for high precision required a larger number of trapped antihydrogen atoms. The measurements of antihydrogen's charge neutrality [5] and the first measurement of the hyperfine transition [130] were obtained and a rough limit on antihydrogen's gravitation was also determined using very small numbers of atoms. Measurements like the hyperfine spectroscopy [64], however, require multiple atoms to be trapped simultaneously (see Sec. 5.9 for details).

Optimizing the trapping rate is an ongoing project in the ALPHA collaboration. We perform a wide range of parameter scans to search for an improved trapping rate. The SDREVC process (see Chap. 4) allows us to reproduce plasma parameters independent of the initial conditions, and plasma manipulation settings selected during optimization studies continue to be reliable for months at a time. Prior to SDREVC, a setting that might be optimal for the positron plasma preparation one day might not be optimal for the different plasma parameters the next day.

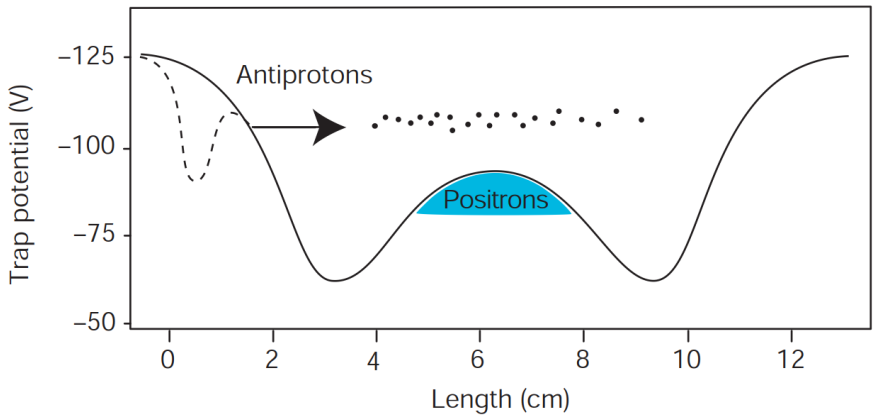

Figure 5.1: Potential wells used to mix antiprotons and positrons in ATHENA. The dashed line shows the antiproton well just before mixing, while the solid line shows the potential well where the antiprotons were released. Figure from Ref. [57].

The antihydrogen atoms produced by ATHENA in the early 2000s were the result of mixing the antiprotons and plasmas by evaporating the antiprotons in the direction of the positrons in a nested well structure, such that the antiprotons would bounce back and forth through the positrons and some collisions could form antihydrogen [57], shown in figure 5.1. While this method produced antihydrogen atoms, these atoms were too warm to be trapped. Jitter in the plasma parameters made it difficult to tune the mixing process, so trapping was not successful using the potential well method. The first trapped antihydrogen was produced by the ALPHA collaboration 2010 by the autoresonance excitation method [60], in which an autoresonant signal was applied to one of the electrodes trapping the antiprotons and excited the antiprotons at their bounce frequency until they had enough energy to escape their potential well and mix with the positrons [131, 75]. This first trapping success and the subsequent physics results were exciting, but despite significant efforts to scan different plasma and potential well parameters, between 2010 and 2016 the collaboration was unsuccessful in increasing the trapping rate beyond an average of one per trapping cycle. This was thought to be due to the high injection energy of the antiprotons due to the excitation process [75].

A closer look at positron plasma stability with SDREVC

A look into the daily measurements we took on ALPHA shows the variations in positron numbers just after loading and just before mixing them with the antiprotons without SDREVC in 2015 and with SDREVC in 2016, shown in Figs. 5.2 and 5.3. In both years, there were large variations in the initial number of positrons, indicated by the brown upward-pointing triangles. In 2015, after loading the plasma the number was reduced by dividing the potential well and releasing some fraction of the particles, and in 2016 the number was reduced

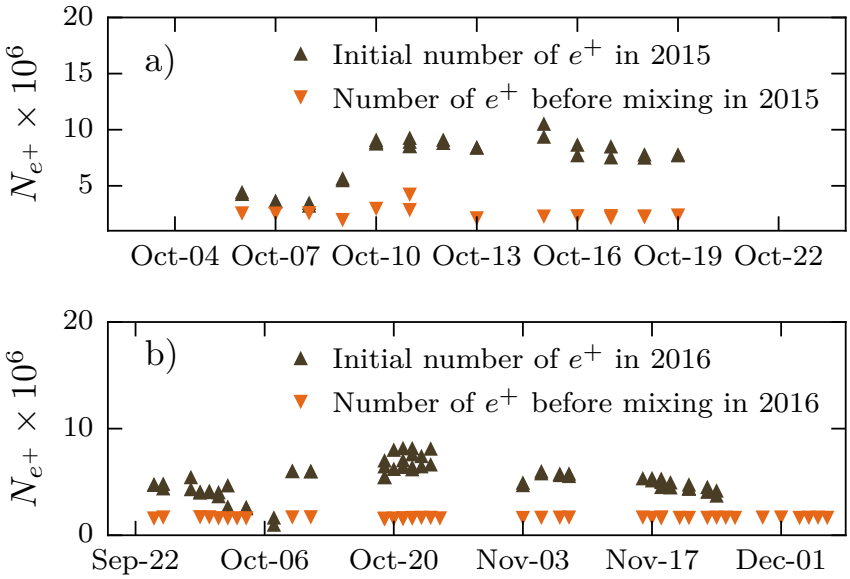

Figure 5.2: Measurements of the initial number of positrons and the number just before mixing in (a) 2015 and (b) 2016 . The brown upward-pointing triangles show the initial number and the orange downward-pointing triangles show the number after EVC, just before mixing in 2016. In Fig. (a), the variation before mixing is 22% over just a two-week period while in Fig. (b) the variation is reduced by SDREVC to 3% over a period of months.

to an absolute number (not a fraction) by SDREVC. In 2015 the number before mixing (indicated by the orange triangles) was partially stabilized by EVC. The data in Figs. 5.2a and 5.3a only covers a 2-week span because we frequently changed the sequences in 2015 to try to improve our trapping rate and the 2-week span was the longest found where we used the same plasma preparation steps; Figs. 5.2b 5.3b cover a two-month range during which we used the same operating parameters. The average number of positrons before mixing in figure 5.3a was 2.5×10^6 with a standard deviation of 5.4×10^5 or 22%. The average of the number of particles before mixing in Figs. 5.2b and 5.3b is 1.6×10^6 and the standard deviation is 4.9×10^4 or 3.1%.

In summary, SDREVC stabilized the number of particles at the 3% level over two months compared to the 20% level achieved with only EVC over two weeks. The only substantial difference in the plasma preparation between the two plots was the implementation of SDREVC, so we attribute the substantial improvement in the reproducibility of the positron plasma parameters just prior to mixing to SDREVC. Any optimization study requires reproducible conditions, otherwise a fluctuation in an uncontrolled parameter can give a false result when searching for a trend. While an incomplete study of positron number versus the trapping rate discussed in section 6.2 indicates that our current trapping scheme is robust to $\pm$ 20 % variations in the number of positrons, SDR and SDREVC are essential to set the density

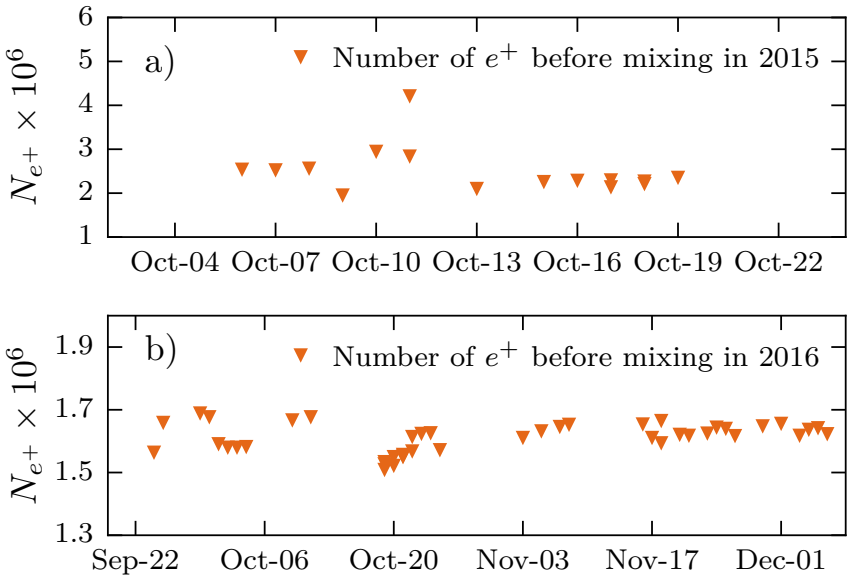

Figure 5.3: Measurements of the number of positrons just before mixing in (a) 2015 and (b) 2016, the same data as in Fig. 5.2 but magnified to show more detail.

and number of particles in our continued optimization studies.

5.2 "Smerge" trapping

Simulations of antihydrogen trapping finished in 2014 indicated that a slow merge of the antiproton and positron potential wells would produce more trapped antihydrogen than the autoresonant method [66]. However, as discussed, the previous attempts to trap antihydrogen by merging antiproton and positron potentials were unsuccessful. During the summer of 2016, after SDREVC was implemented giving us stable plasma parameters, we continued to try to find more optimal settings for autoresonant mixing but our trapping rate didn't increase much above 1 atom per cycle. During a week of night-long antiproton shifts in August 2016, we (in particular Tim Friesen) tried again to mix using a slow merge of potentials (herafter referred to as "smerge") and this time we immediately achieved increased trapping rates. Initially the rate was 1-3 per attempt but optimization brought an average of 21 trapped antihydrogen atoms per attempt during the last few weeks of the experimental run in 2017.

Smerge differs from autoresonance in that instead of injecting extra energy into the antiprotons to drive them out of their potential well and mix with the positrons, we lower the potential barrier between the positrons and antiprotons and the plasmas evaporate towards each other. Different steps of the smerge procedure are shown in figure 5.4. Following the

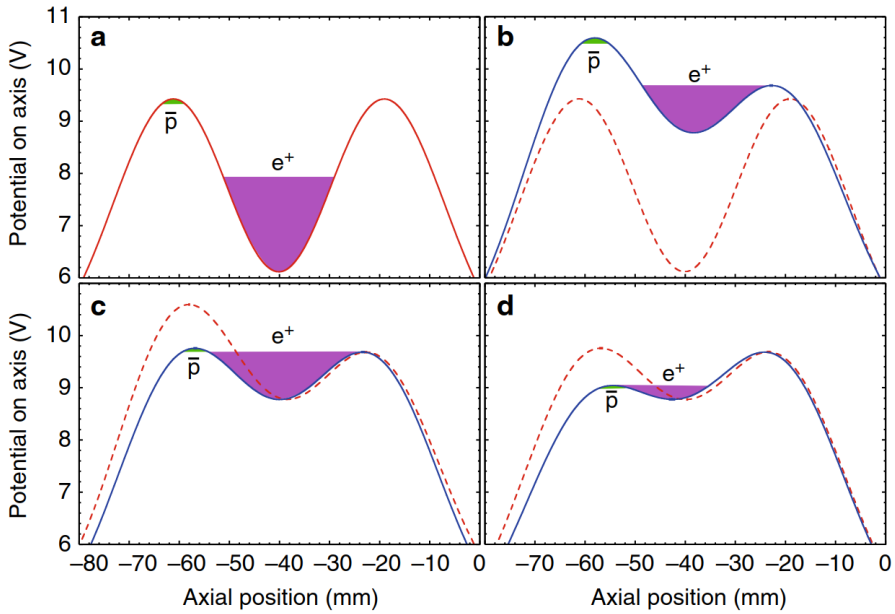

Figure 5.4: Sequence of potential wells applied to evaporate positrons into the antiproton plasma. Figure from Ref. [129].

sympathetic cooling of antiprotons and cyclotron and adiabatic cooling of positrons, they are brought to adjacent wells near the center of the atom trap, as in Fig. 5.4a. In Fig. 5.4b, the potential wells are more positively biased while the barrier on the right of the positrons is lowered; while this was used in 2016 we no longer include this step in smerge. We obtained the highest trapping rate by performing a fast ramp of potentials from Fig. 5.4b (or 5.4a) to the levels in Fig. 5.4c. Finally, antihydrogen synthesis occurs in the potential well transition from Fig. 5.4c to Fig. 5.4d. Plasmas with different densities or numbers of particles will fill up the wells differently, so when we tune smerge to match a particular plasma we vary the depth of the wells in parts 5.4c and 5.4d. After the antihydrogen synthesis finishes, we dump the remaining positrons to measure their temperature. We found that the trapping rate wasn't noticeably affected by retaining the small number of positrons shown in Fig. 5.4d; we had a similar rate if we completely flattened the wells and dumped all the particles. The temperature dump is the only direct measurement we perform on the positrons during an antihydrogen mixing cycle, and it gives us information about the plasma conditions we can track and compare between mixing cycles.

During the 2017 run we also ran a scan of the trapping rate as a function of the antiproton density. This was accomplished by applying a rotating wall to the antiproton/electron mixture in the atom trap at different frequencies, ejecting the electrons in a series of ekicks and proceeding to smerge. The surprising result was that the higher trapping rate occurred when the antiproton density was lower, so for the rest of the run we applied a low-frequency rotating wall on the electron-antiproton mixture in the preparation stage to lower the density.

Increasing the antiproton catching and cooling efficiency

We also achieved a factor of two increase in our antiproton cooling efficiency, from around 33% to 72%, which further improved the antihydrogen trapping rate. The cooling efficiency is defined as:

$$\text{Cooling Efficiency (\%)} = \frac{\text{(Number in cold dump)}}{\text{(Number in hot dump)+(number in cold dump)}}. \tag{5.1}$$

The cooling efficiency can be increased by increasing the number of electrons, but it is still necessary to eject the electrons. We found that we could apply SDREVC to the antiproton/electron plasma and reduce the electron load from 90 to 23 million without losing many antiprotons, and then remove the rest of the electrons with ekicks and proceed with trapping as normal. The larger number of antiprotons directly contributed to the increase in trapping rate reported in 2016 [129].

Trapping development with consecutive beams of antiprotons

In addition to increasing the cooling efficiency, we developed trapping sequences that caught consecutive bunches of antiprotons from the antiproton decelerator. To catch multiple beams of antiprotons, we would catch the first beam in a large cloud of electrons, cool for 20s and do the hot dump, then apply a rotating wall to the plasma until shortly before the next beam arrives, then erect the catching potentials again and catch the next stack, and proceed with trapping as normal. Using twice the number of antiprotons gave us a maximum of 33 pass cuts, the record we have achieved in a single antihydrogen trapping cycle. However, because we were already taking physics measurements with a standard load of one bunch of antiprotons, development time was limited and for the sake of operational consistency we did not make substantial changes to the trapping routine at this time. We plan to perform more studies of the trapping rate with multiple bunches of antiprotons in the future.

Trapping studies with different numbers of positrons

Another optimization study initiated was a parameter scan of positron numbers and densities. To begin with we changed the SDREVC well depth to make plasmas with 2×10^6, 3×10^6, and 4.3×10^6 positrons, with 3×10^6 being the nominal load we used in the 2017 trapping run. In a preliminary study with a few measurements of three different numbers of positrons shown in Fig. 5.5, we did not observe much difference in the mixing trigger rates or pass cut rates (see section 2.2 for terminology). However, these were not optimized trapping procedures, as the smerge well was not tuned exactly for each set of plasma parameters. There was not enough time to devote many shifts to the positron trapping development studies since there were important CPT physics measurements to be performed. We plan to continue this trapping optimization study in the future.

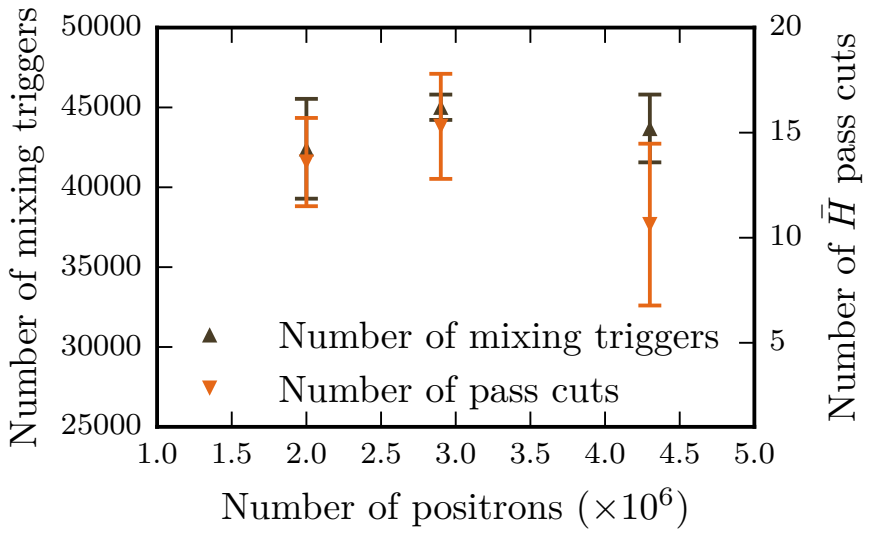

Figure 5.5: Mixing triggers and trapped antihydrogen atoms (the number that passed cuts in the detector analysis) for different numbers of positrons.

In summary, the optimizations we completed and implementation of the smerge method produced an antihydrogen trapping rate 20 times higher than we achieved when using autoresonance.

5.3 Antihydrogen accumulation

We extended the benefits of the higher trapping rate by developing a new method to accumulate antihydrogen over multiple trapping cycles [129]. Accumulating allows us to make certain measurements much more efficiently, particularly those that require longer measurement time. We get better results from a measurement on 50 antihydrogen atoms than by repeating the same measurement five times on ten antihydrogen atoms. Among other reasons, this is because the background cosmic annihilation rate is a function of measurement time, so the background is fractionally smaller when we do a measurement on a larger number of atoms, and uncertainties due to parameter drifts are minimized.

Accumulation begins with a normal cycle of trapping antihydrogen. We then leave the trap magnets (mirror and octupole magnets) on to continue to trap the antihydrogen atoms while performing the normal steps of a new trapping cycle. Variations in magnetic fields during the trapping cycle and the interaction between the octupole field and the positrons during their preparation stages could have substantial side effects, so accumulation was not obviously going to work. As discussed in section 2.2, the total trap depth is given by $\Delta B = \sqrt{B_r^2 + B_z^2} - B_z$ [36], so increasing the axial field B_z while keeping the radial field B_r constant decreases the trap depth. The 3 T solenoids used in the plasma cooling steps

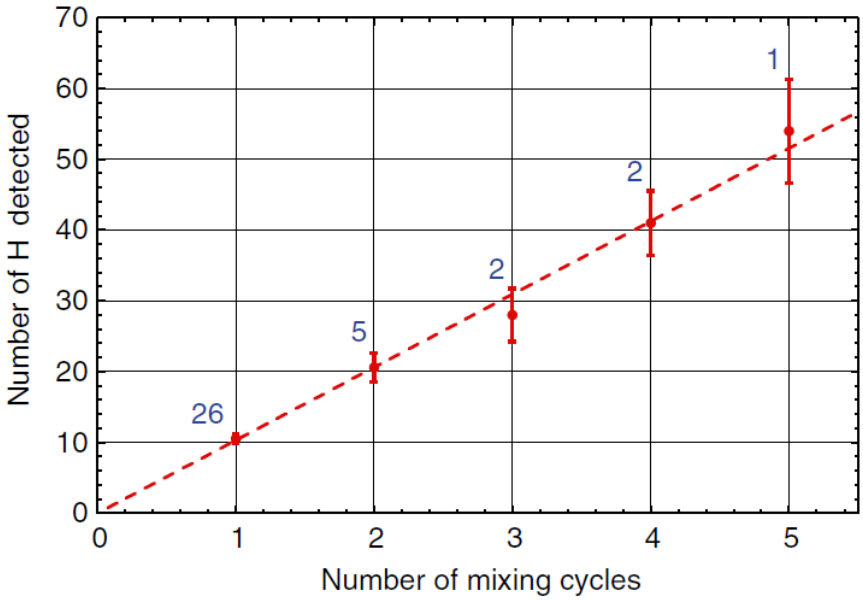

Figure 5.6: Number of accumulated antihydrogen atoms versus number of trapping cycles achieved in 2016. Figure from reference [129].

increase the axial field in the center of the trap by a few hundredths of a Tesla. After some development, though, we found that most of the trapped atoms stayed trapped in the modified well shape during subsequent mixing cycles. We achieved an accumulated trapping rate (trapped atoms averaged over the number of cycles) close to the single cycle trapping rate.

We observe an approximately linear trend in the number of trapped antihydrogen atoms versus stacking cycles, shown in figure 5.6. In general in many different tests, the accumulated trapping rate averaged over the number of stacks is lower than the single-stack average, possibly due to the magnetic field changes, but the ability to perform measurements on dozens of atoms has greatly contributed to our recent measurements of the hyperfine and 1s-2s spectroscopy.

5.4 Efforts towards applying SDREVC on an antiproton plasma

After developing SDREVC on lepton plasmas, we explored whether it was possible to use it to control the number of antiprotons. As an antiproton plasma does not cool quickly by cyclotron radiation and the rotating wall heats up the plasma, this proved to be a difficult project. Including electrons keeps the antiprotons cold, but then the electrons fill in some uncontrolled fraction of the space charge, and the antiproton number is not controlled.

Preliminary results indicated that a fraction of antiprotons could be retained, but not an absolute number independent of the initial number. When we applied SDREVC on a pure antiproton plasma the plasma, even if it was initially cooled to a few hundred Kelvin, it heated up to 3000-4000 K. At a few thousand Kelvin, antiprotons are expected to evaporate at a rate dependent on their temperature and not their density so the attempted SDREVC becomes a RW-heated evaporation process, not evaporation in the strong drive regime. As of now it does not seem that SDREVC will work on an antiproton plasma, but we may still try to continue this study this year.

5.5 Search for a microwave cavity near the trapping region in the atom trap

Section 3.4 discussed a special cavity electrode designed to enhance cooling rates of non-neutral plasmas in Penning traps [95]. This was mainly the thesis work of Alex Povilus while continued studies are being performed as the thesis work of Eric Hunter, both from the Fajans' group at Berkeley, in collaboration with Nathan Evetts from the University of British Columbia. As noted before, ALPHA does not have a special cavity-enhancing electrode, but inherent cavity modes exist naturally inside the trap structure and the resonant frequencies can by accessed by tuning the magnetic field. These inherent cavities will not have as strong of an effect on the cooling rate, but even an enhancement of a factor of two in the positron cooling rate could improve the antihydrogen trapping rate. During the 2017 run, Eric initiated a search for existing cavity modes at ECR frequencies we could access near the normal trap fields in the ALPHA trap, and the author continued the search after he returned to Berkeley. The studies were done by creating a plasma, moving it to a particular location in the trap at a particular magnetic field strength, cooling it for a short time at that field, and dumping the plasma to record its temperature. This process was repeated at different magnetic fields, which we modified by changing the current in one of the mirror magnets, as well as in different regions in the trap. In general we used the reservoir electron load described in section 2.4. We hoped to find an existing cavity mode in the center of the trap which would enhance the positron's cooling rate during smerge and give us colder antihydrogen atoms. We found a couple of locations and magnetic fields that resulted in enhanced cooling rates of an electron plasma with 64 thousand particles, for example in figure 5.7, but did not observe enhanced cooling for plasmas with 3 million particles, so this technique has not been integrated yet in our trapping routines. With more studies we may find a better mode in the existing ALPHA trap, or a future version of the ALPHA trap may include a cavity-enhancing electrode.

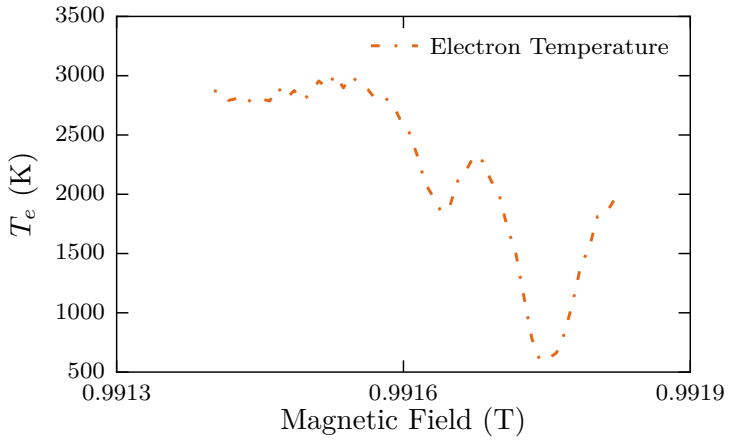

Figure 5.7: Temperature of electrons held for three seconds in the same well location at different magnetic fields.

5.6 Diagnostic check: recorded temperatures as a function of the MCP gain for two different detectors

A new hardware development initiated at the Fajans' group in Berkeley [132] and tested at ALPHA is a silicon photomultiplier (SiPM) detector which detects fluorescence of particles on the MCP. Rather than taking a picture of the amplified charge on the MCP with a camera, it measures the amplitude of light as a function of time. This is an alternative to the temperature measurement where we use an MCP to amplify the charge and a FC to measure the voltage as a function of time. The SiPM was proposed as an alternative detector for the temperature diagnostic. One ongoing question is whether the temperatures recorded have reached a systematic limit or whether the temperatures inside the apparatus are at their limit. To investigate this, we took a series of measurements of the temperature using the FC and the SiPM for different MCP gains, shown in figures 5.8 and 5.9.

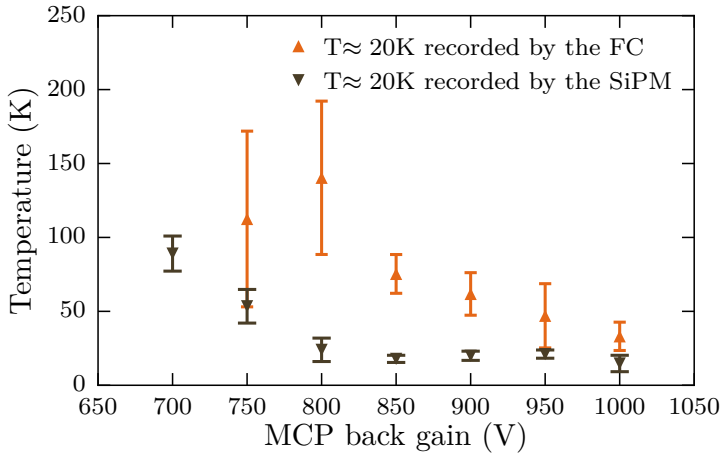

Figure 5.8: Recorded temperatures using the SiPM and FC diagnostics of plasmas with T≈20 K as a function of the MCP gain. The orange markers (▲) show the temperatures recorded by the FC and the brown markers (▼) show the temperature recorded by the SiPM. Error bars show the average of ten measurements, with the exception of a few measurements which were too noisy to analyze.

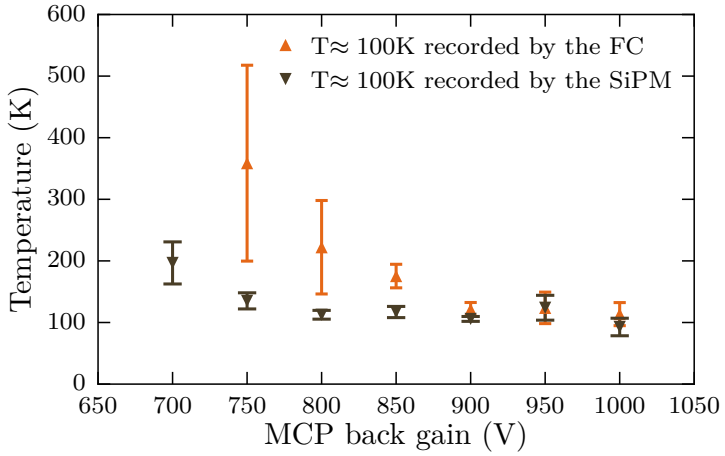

Figure 5.9: Recorded temperatures using the SiPM and FC diagnostics of plasmas with T≈100 K as a function of the MCP gain. The orange markers (▲) show the temperatures recorded by the FC and the brown markers (▼) show the temperature recorded by the SiPM. Error bars show the average of ten measurements, with the exception of a few measurements which were too noisy to analyze.

We observe that the FC measurements as a function of the MCP gain have not reached an equilibrium temperature for cold temperatures even at the normal operating voltage of

1000V. Especially notable is that in figure 5.8, while the SiPM recorded a temperature around 15-20K, the Faraday cup measurement was around 30K but the trend in data points suggests it would record a lower temperature if we could use a higher gain. The measurements at 100K are at an equilibrium value at a gain of 1000V, but these measurements indicate that the SiPM is more suitable for cold temperature measurements. The colder temperature recorded by the SiPM also suggests that perhaps historically our plasmas have been colder than we thought.

5.7 Studies of plasma temperatures and the trapping rate with the flappers

The flappers discussed in section 2.2 were the main hardware component for which the author was responsible. The goal of the flappers was to lower the minimum equilibrium temperature of our lepton plasmas enough to improve the trapping rate, by blocking radiation or warm neutral particles from propagating down the beamline into the trap. Flapper development included assembling one of the flappers, testing it on a bench and in a cryogenic vacuum test apparatus to check its mechanical reliability, setting up and programming a control system with Labview and a National Instruments myRIO device, soldering electrical connections, and finally setting up and running measurements using the flappers. Even though the flappers mechanically worked inside the experiment as designed, the flappers did not lead to significantly colder plasmas. The flappers were tested in the ALPHA apparatus in February 2017 and in December 2017. The test in February was done under less than ideal conditions because the electrons and positrons were heating up substantially due to other uncontrolled reasons. However, the results in Fig. 5.10 indicate that after 20s, the flappers had a substantial effect on the temperature. These measurements were performed by preparing an electron plasma to be as cold as possible, with the flappers either open or closed. For the measurements with the flappers closed, they were kept closed for variable wait times while the electron plasma was held fixed in a potential well. The flapper opening time was measured to be about half a second, so we opened the flappers while continuing to hold the plasma in the potential well and then released the plasma in a temperature measurement. The wait times were kept the same for the measurements with the flappers open.

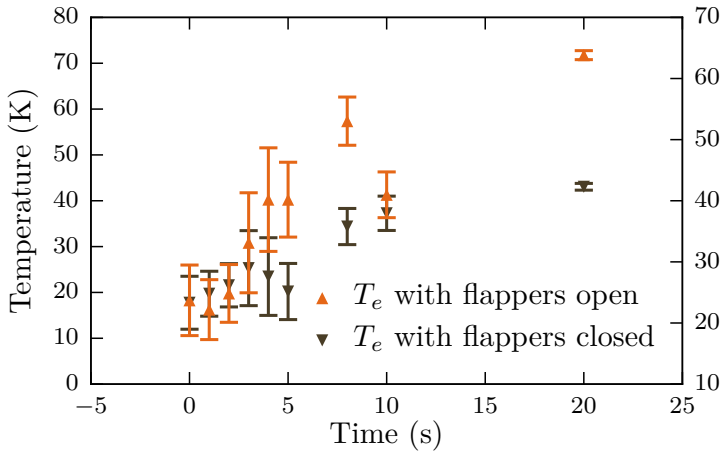

Figure 5.10: Electron temperature measurements made with the flappers open indicated by the orange triangles (▲) and closed indicated by the brown triangles (▼) in February 2017 The error bars show the standard deviation of 8 measurements.

Operating the flappers is inherently risky, because if one flapper got stuck closed, it would take at least two weeks to warm up the experiment, open up the vacuum and physically push the door back open, then close the vacuum, bake the apparatus, and resume measurements. If anything broke during the intervention, the lost time could amount to several weeks or more. The second set of flapper tests were done in December 2017, after the year's physics results had been obtained. The December tests were done on cold and stable plasmas without the extraneous heating problem that was present in February. In this second set of measurements, there was no large difference in temperatures for the flappers being open or closed, although the average temperature was consistently colder.

The most significant flapper effect we observed was that two temperature sensors inside of the cryogenic region, one on an electrode and one on the mount for the laser cavity, recorded equilibrium temperatures 0.15-0.2 K cooler with the flappers closed. These colder temperatures indicate the flappers are indeed blocking some heat that propagates into the trap. However, the measurements of particle temperatures and a few tests of the antihydrogen trapping rate with the flappers closed indicate the shielding effect is too small to benefit ALPHA. We didn't have time to take a large amount of statistics or scans of plasma parameters, so we were unable to fully characterize the effect of the flappers. However, because flapper operation is inherently a risk to the experiment and their operation did not appear to substantially benefit the experiment, it is unlikely we will pursue more studies with the flappers this year.

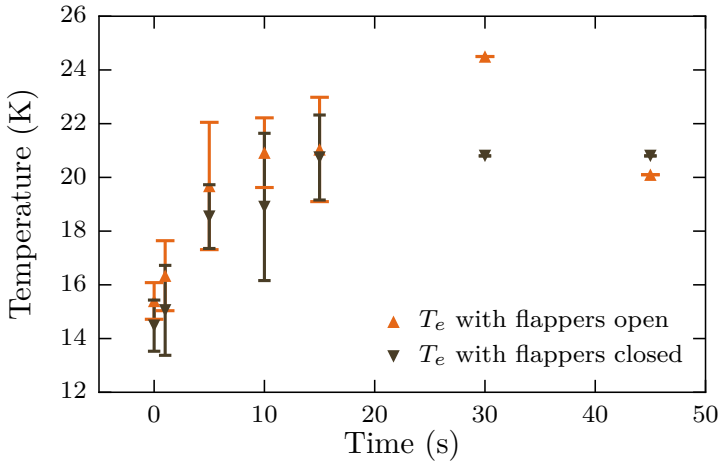

Figure 5.11: Electron temperature measurements made with the flappers open, indicated by the orange triangles (▲), and closed, indicated by the brown triangles (▼), in December 2017. The error bars show the standard deviation of five measurements.

5.8 Charge neutrality of antihydrogen

CPT symmetry requires the magnitude of charge to be exactly the same for a particle and its antiparticle. The ASACUSA collaboration measured the antiproton-to-electron mass ratio and put a low limit on the fractional difference in charge between antiprotons and electrons [133]:

$$\frac{|q_{\bar{p}} - e|}{e} < 7 \times 10^{-10} \tag{5.2}$$

where e is the magnitude of the electron charge, 1.6×10^{-19} C.

The ALPHA collaboration reported a measurement on the charge of antihydrogen in 2014 [134] and improved this measurement 2015 [5], setting an upper limit on the charge of an antihydrogen atom at $7.1 \times 10^{-10} e$. Comparing this value with the measured charge of antiprotons puts a limit on the fractional positron/electron charge difference that is more than an order of magnitude smaller than the previous measurement of $1 \pm 2.5 \times 10^{-8}$ [135].

This precise charge measurement was performed by applying stochastically varying electric fields alternating between approximately +140 V and -140 V to the magnetically trapped atoms, illustrated in Fig. 5.12. The stochastic variation was created by using a uniform distribution with random modulation, and the standard deviation for the time steps was 0.2 ms. After N potential steps, an atom with charge Qe should gain energy of $|Q|e\Delta\phi\sqrt{N}$, analogous to how a particle in a 2D random walk motion with equal step size Δx will be found at a distance $x_{RMS} \approx \sqrt{N}\Delta x$ from the starting point after N steps. A simple estimate is that if an atom gained enough energy to escape its magnetic well, where E_{well} is the depth

of the well, then its normalized charge $|Q|$ must have a lower bound of:

$$|Q| > \frac{E_{\text{well}}}{e\Delta\phi\sqrt{N}}, \tag{5.3}$$

$$\approx \frac{k_B \times 0.54\text{K}}{e100\text{V}\sqrt{84900}} \tag{5.4}$$

$$\approx 1.6 \times 10^{-9}, \tag{5.5}$$

so if the atom does not escape the well, its charge must be less than this value.

Measurements were alternated between stochastic trials and null trials. During the null trials atoms were trapped for the same length of time in grounded electric potentials. The number of atoms remaining at the end of both measurements was the same: out of ten trapping cycles a total of 12 atoms remained for the stochastic and the null trials. Since no antihydrogen atoms were observed to escape the trap due to acceleration by electric fields, the charge of antihydrogen must be less than 1.6×10^{-9}. A more precise calculation taking into account statistical error measured in Monte Carlo simulations reduced this upper limit to 0.71×10^{-9} [5]. Given the previously-stated limit on antiproton charge anomaly, the charge anomaly of a positron is limited to $Q(e^+) < 1 \times 10^{-9}$, a factor of 25 more precise than the previous limit [5].

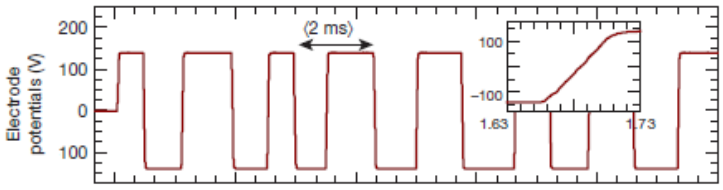

Figure 5.12: Potentials applied at stochastically-varying times to trapped antihydrogen atoms. Figure modified from Ref. [5].

5.9 Hyperfine spectrum of antihydrogen

The interaction between the magnetic moments of a proton and an electron has a slight contribution to the energy levels of an atom, an effect known as "hyperfine splitting." The hyperfine energy levels depend on the spin orientations of the antiproton and positron. In addition, the interaction between an atom's magnetic dipole moment and an externally applied static magnetic field causes the energy levels to split; this is known as Zeeman splitting. Hyperfine splitting was first observed in hydrogen in 1948 [136], and a comparison of the hyperfine energy level transitions of hydrogen and antihydrogen is an important test of CPT symmetry. The ALPHA collaboration first measured the positron spin-flip signature of a few dozen of these quantum transitions in antihydrogen in 2012 [130], but the resonant frequency was bounded only at a broad 100 MHz level and no spectrum was measurable.

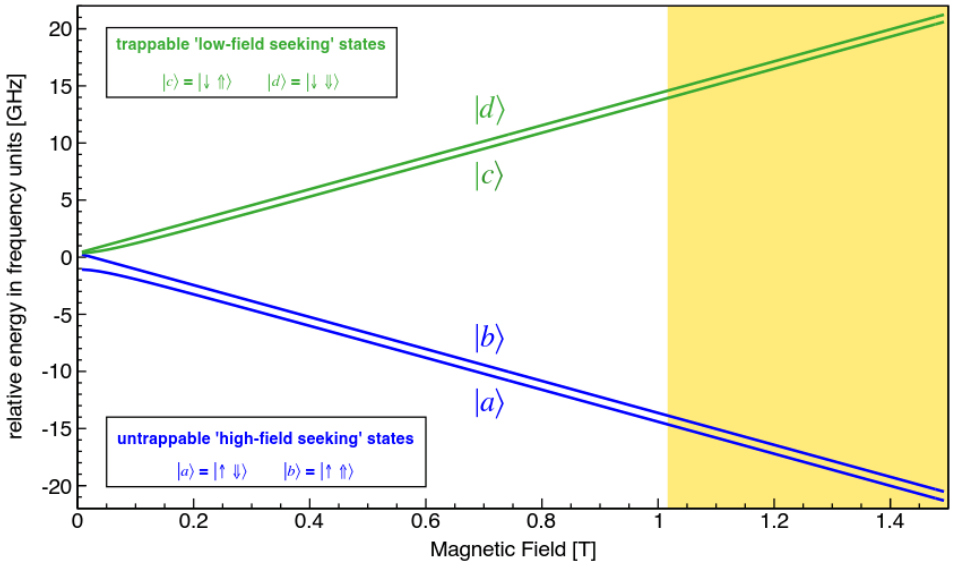

Figure 5.13: Hydrogen's hyperfine energy levels in a magnetic field. The green lines show the trappable states and the blue lines show the untrappable states, and the lower boundary of the yellow region near 1 T corresponds to the lower limit of the trapping field in the ALPHA trap; thus atoms in the atom trap will experience magnetic fields in the yellow region and we must scan over the corresponding relative frequencies. Figure from Ref. [64].

This section summarizes the ALPHA collaborations measurement in 2016 of the hyperfine spectrum of antihydrogen [64].

In Zeeman splitting, a hydrogen or antihydrogen atom in its ground state has a total of four energy levels, each corresponding to one of the four spin states marked on Fig. 5.13: $|a\rangle = |\uparrow\Downarrow\rangle, |b\rangle = |\uparrow\Uparrow\rangle, |c\rangle = |\downarrow\Uparrow\rangle$, and $|d\rangle = |\downarrow\Downarrow\rangle$. The left arrow ($\uparrow$ or $\downarrow$) corresponds to the positron's alignment with the magnetic field and the right arrow ($\Uparrow$ or $\Downarrow$) corresponds to the antiproton's alignment with the magnetic field. An atom is in a lower energy state when the spins are aligned with the magnetic field.

At large magnetic fields near 1 T, the difference in energy between the neighboring hyperfine levels is a nearly constant offset for different magnetic fields, while the energy difference from Zeeman splitting increases linearly with the magnetic field. As indicated on the figure, Zeeman splitting produces two states that are untrappable in a minimum magnetic field, $|a\rangle$ and $|b\rangle$, and two trappable states, $|c\rangle$ and $|d\rangle$. The trappable and untrappable states can be thought of as putting a marble on a concave-down surface where it falls away to a low energy state, compared with putting a marble inside a concave-up surface (like a bowl) where the marble falls inwards to the middle and stays inside. The positron spin points down, meaning in the same direction of the magnetic field, in the trapped $|c\rangle$ and $|d\rangle$ states shown in figure 5.13. In these two states, the potential energy of an atom increases with increasing magnetic field, and they are confined by the minimum-field trap. The $|a\rangle$ and $|b\rangle$

states experience the lowest potential energy at high fields, so they escape the minimum-field trap. To excite an antihydrogen atom from its trapped state to an untrapped state, the positron spin has to be flipped from pointing in the direction of the magnetic field to pointing in the opposite direction, which occurs in the $|d\rangle \rightarrow |a\rangle$ and $|c\rangle \rightarrow |b\rangle$ transitions.

Due to Zeeman splitting, it is necessary to precisely know the minimum value of the magnetic field in the trap, where the trapped atoms are most likely to be, in order to program the microwave synthesizer to produce microwaves in exactly the right frequency range. One challenge is that the exact value of the magnetic field drifts with time, as previously discussed, and this has to be characterized and accounted for during the repeated measurement cycles. Careful magnetic field measurements using ECR were performed daily to a precision of 0.3 mT [64], just prior to beginning the hyperfine measurements.

The microwave frequencies required to drive the $|d\rangle \rightarrow |a\rangle$ transitions are larger than the frequencies required to drive the $|c\rangle \rightarrow |b\rangle$ transitions. To drive both transitions, we first excited the $|c\rangle \rightarrow |b\rangle$ transition, then increased the microwave frequency to 1.4204 GHz to drive the $|d\rangle \rightarrow |a\rangle$ transition. Both transitions were characterized over a range of 4.8 MHz, with data points spaced 300 kHz apart, and the results are shown in Fig. 5.14. The $|c\rangle \rightarrow |b\rangle$ transition appears to have a much sharper peak, which is explained by ECR measurements that indicate the *in situ* magnitude of the microwave electric field is seven times stronger at that frequency than in the $|d\rangle \rightarrow |a\rangle$ transition frequency, due to the specific features of how we inject microwaves into the trap. To partially compensate for this discrepancy, the microwave power driving the $|d\rangle \rightarrow |a\rangle$ transition was set to twice the power applied in the $|c\rangle \rightarrow |b\rangle$ transition; driving it higher would risk heating the trap too much. Each frequency was applied for 4s to allow a number of atoms to pass through a region in the trap where the magnetic field and the microwave frequency are matched to excite the spin flip. The number of annihilations that occur at each frequency are counted, and at the end of the measurements the trap magnets are ramped down and the annihilations of remaining atoms are counted. In this data set only 4% of the total number of atoms were found remaining in the trap after the microwave exposure [64].

The distribution of annihilation events is affected by the number of atoms in the trap and the amplitude of the microwave electric field. Atoms orbit the trap and experience slightly different magnetic fields since the minimum level of the trap is not perfectly flat axially or radially. At the start of each scan there were an average of 14 atoms in the trap, presumably half in the $|c\rangle$ state and half in the $|d\rangle$ state. A large fraction of the trapped atoms will pass through the minimum field point. At the "onset" frequency, the atoms in the minimum field will spin-flip and escape the trap. In Fig. 5.14, this onset frequency is observed as the first sharp increase in annihilations as a function of frequencies. At the subsequent frequencies, fewer and fewer atoms will be in the trap and will be observed annihilating. The frequency corresponding to hyperfine splitting is the difference between onset frequencies, which in this measurement was determined to be $1,420.4 \pm 0.5$ MHz. This value agrees with the most precise measurement of the hyperfine splitting frequency in hydrogen to one part in 10^4 and is consistent with CPT symmetry. This measurement fundamentally requires multiple atoms to be in the trap at the beginning, so it was impossible to perform before we achieved the

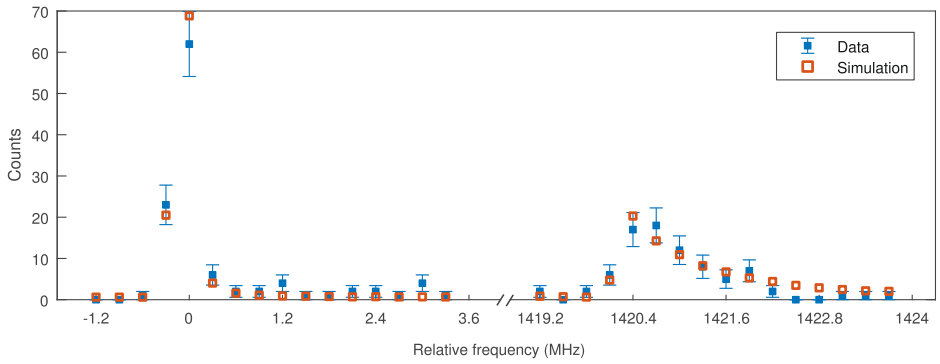

Figure 5.14: Hyperfine spectrum of antihydrogen; counts correspond to individual annihilation events. Figure from reference [64].

higher trapping rate.

5.10 1S-2S spectroscopy of antihydrogen

The difference between hydrogen's 1S and 2S energy levels, its ground state and first excited state, is one of the most precisely measured values of any physical system: the relative uncertainty is 4.5 parts in 10^{-15} [137]. In 2017 the ALPHA collaboration characterized the 1S-2S transition of antihydrogen; this measurement is one of the most precise tests of CPT symmetry. The measurement is discussed in detail in Ref. [63] and is summarized in this section.

An antihydrogen atom is excited from the 1S to the 2S state when two photons at half the transition frequency simultaneously interact with the atom. On opposite ends of the atom trap but still within the cryogenic region, shown in figure 5.15, are a pair of precisely aligned mirrors that form a cavity. As mirrors cannot be mounted exactly centered on the beamline, they are located off-axis and angled slightly, as shown in figure 5.15 to cross the center of the trap. The mirrors are mounted on piezo crystals that expand or contract slightly with an applied voltage, which allows the mirror alignment to be controlled outside of the vacuum and cryogenic environment. The laser power in the cavity is approximately 1W.

The 1S-2S transition cannot be driven directly by a single photon because the transition has no change in angular momentum, and a single photon absorption would necessarily add angular momentum to the atom. For this reason, and also to avoid broadening by the doppler shift, we use a two-photon excitation method where two photons at half the transition frequency can interact with the antihydrogen atom and excite it. This avoids a first-order doppler shift because the sum of the relative photon frequencies the atom experiences will be constant despite the atom's motion inside the trap.

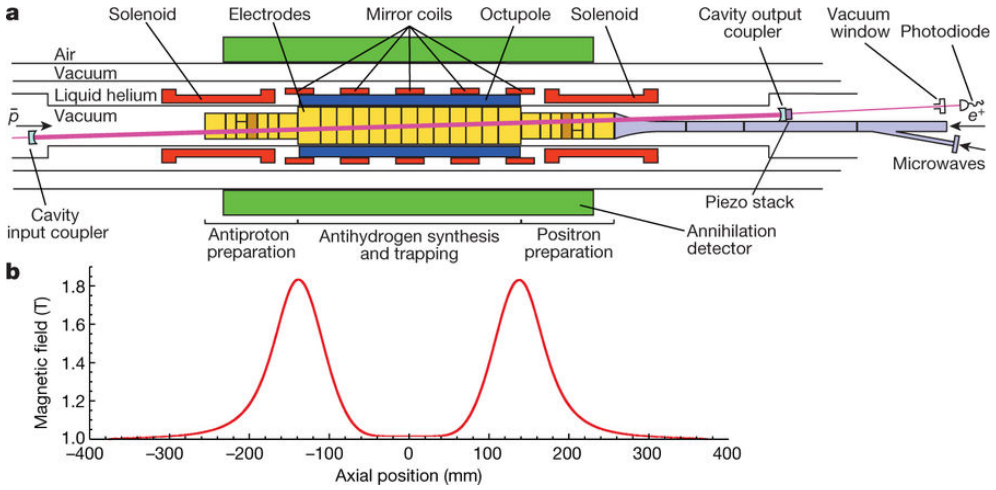

Figure 5.15: Schematic showing the electrodes, trap magnets, laser path and cavity mirrors, and the trap magnetic field. Figure from reference [62].

To characterize the lineshape [63], we accumulated antihydrogen atoms over three mixing cycles, used potential fields in the trap to remove any leftover charged particles, then illuminated the atoms for 300 s at the frequency to excite the $1S_d - 2S_d$ transition. Following the laser excitation, the atoms in the $1S_c$ states were ejected with microwaves as in the hyperfine measurement. Half of the atoms should be in the $1S_c$ state, so we count the number ejected by the microwaves to determine how many atoms were in the trap for that measurement. After exciting the $1S_d - 2S_d$ transition and counting the resulting annihilations, then counting how many atoms were in the $1S_c$ state that annihilated during the microwave kickout, we count how many atoms remain in the trap at the end while ramping down the trap magnets.

This final set of atoms that annihilates when the magnets turn off should be the number of atoms in the $1S_d$ state which did not interact with the laser. This method allows us to count "appearance" and "disappearance" events. "Appearance" events are the annihilations we record during the laser exposure time window. "Disappearance" events are the difference in counts between the no-laser or off-resonance measurements and the on-resonance measurements: at the end of a null measurement, the full number of trapped atoms is counted at the end when the trap magnets ramp down, while in the on-resonance measurement, only atoms that did not interact with the microwaves or the laser will remain and be counted when the trap turns off. Unlike the hyperfine measurement where the transition was measured by scanning microwave frequencies over a set of trapped particles and repeating the same frequency range over multiple accumulation cycles, in the 1s-2s measurement we only tested one laser frequency per accumulation cycle. We repeated measurements at least twenty times so that each frequency was measured on a total of 800-1000 trapped atoms.

The frequencies measured were centered around the calculated transition frequency and detuned by -200 kHz, -100 kHz, -50 kHz, -25 kHz, 0 kHz, 25 kHz, 50 kHz, 100 kHz , and 200 kHz. These measurements were alternated with measurements where the atoms were

prepared and held for the same amount of time but with the laser off. The results and simulated lineshape are shown in Fig. 5.16.

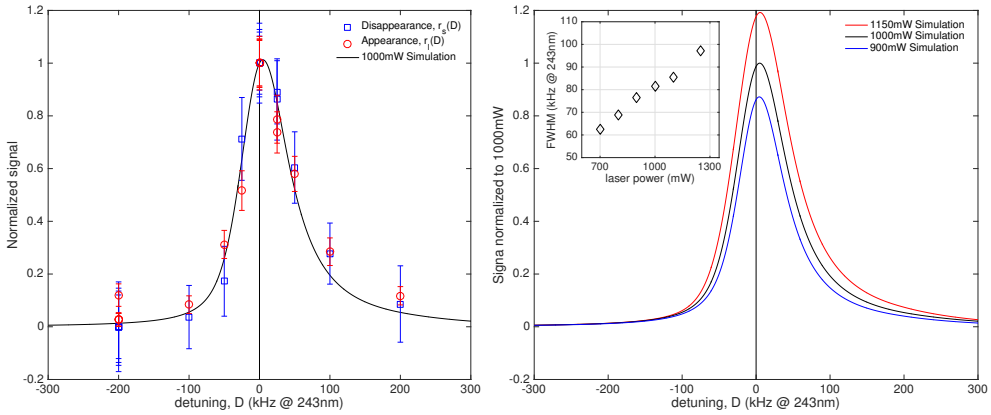

Figure 5.16: The measured and simulated lineshapes of antihydrogen's 1s-2s transition. The plot on the left shows the measurements and the plot on the right shows a simulated lineshape. Figure from Ref. [63].

The asymmetry in the lineshapes is due to Zeeman splitting, and the width is dominated by transit-time broadening with small contributions from the Stark shift and antihydrogen ionization. Transit-time broadening depends on the amount of time an atom spends in the laser beam. High beam intensity increases the probability of an interaction, but the higher the power the narrower the beam for a given input power. An atom will spend more time traversing a wider beam which would reduce the transit-time broadening effect, but the lower beam power correlated to a wider diameter which would reduce the probability of exciting the atom.

Analysis of the data show a precision of 2×10^{-20} GeV, which surpasses the previous CPT-invariance limit of 4×10^{-19} determined by measurements of the mass difference of kaons and antikaons [138]. This spectrum of antihydrogen is now the most precise test (and confirmation) of CPT symmetry in antihydrogen and one of the most precise tests of CPT symmetry. Further studies on antihydrogen in the near future are expected to put an even more precise limit on CPT symmetry.

Chapter 6

Summary and suggested studies for the future

6.1 Review of progress in antihydrogen production and precision studies

The recent plasma-based developments in the ALPHA experiment in the last two years have lead to a dramatically higher trapping rate. Of particular importance was the innovation of SDREVC, which provides a way to control plasma particle numbers and densities during optimization studies and ensures long-term reproducibility. With the new stability in plasma parameters, it was possible to implement the "smerge" trapping method which opened up a new regime of antihydrogen production. We completed a number of optimization studies with smerge, and are able to trap 15-20 atoms per four-minute cycle. The further ability to accumulate antihydrogen in the trap allows us to do measurements on more than 50 atoms at a time. The larger number of trapped atoms enables more precise measurements than we could obtain by repeating measurements on one atom at a time as we did before. Within a few months of developing the high trapping rate in 2016 we performed the first measurement of the 1S-2S spectroscopy of antihydrogen, followed by a measurement of the hyperfine transition and a full line-shape measurement of the 1S-2S transition in 2017. The 1S-2S line-shape measurement is now one of the most precise measurement of charge-parity-time invariance. Although three years ago we were unable to trap more than one atom at a time, now, our measurements on trapped antihydrogen test CPT at a similar level of precision achieved by high energy physics experiments.

6.2 Plasma developments to further optimize antihydrogen production

We have observed that the trapping rate using a slow merging of antiprotons and positrons is affected by the number, temperature, and density of the antiproton and positron plasmas just prior to merging, as well as the timing and depth of the merging potentials. Fully characterizing this method is an intensive process. In the actual running of the experiments, there is a natural tension between the desire to increase the trapping rate and the experimental program full of CPT symmetry tests to perform on the atoms we trap. Below I consider what the next steps are in the quest to increase trapping by another factor of 10 or more.

Future prospects for sympathetic cooling via laser cooled ions

As of now, laser cooling of a negative ion has not been achieved, but the AEgIS collaboration proposes to sympathetically cool antiprotons with laser-cooled C_2^- ions [139]. The BASE collaboration proposes to laser-cool beryllium ions and place them in a potential well in a Penning trap separated by an end-cap electrode from the antiprotons, with the end-cap electrode providing a thermalization mechanism through image currents while physically separating the clouds of particles to prevent the antiprotons from annihilating [140]. Sympathetically cooling positrons with laser-cooled Be^+ ions was achieved in 2002 [141], and since the antihydrogen production and trapping rates are highly dependent on the positron temperature, the ALPHA collaboration is in the process of integrating a laser-cooled Be^+ ion source into the experiment. This was the primary focus of M. Sameed's thesis [142]. During the slow merging synthesis of the antiproton and positron plasmas, it is expected that the two plasmas partially thermalize through collisions before trappable antihydrogen is synthesized. We use a large ratio of positrons to antiprotons in order for the positrons to cool the antiprotons. Currently, positron plasma temperatures are normally around 20-30 K and antiproton plasma temperatures are approximately 100K, but we can only trap atoms colder than 0.54K. Around 99.9% of the antihydrogen atoms synthesized are too warm to be trapped [129]. Sympathetically cooled positrons at temperatures in the mK range instead of the 20K range should lead to much colder synthesized antihydrogen, which would significantly increase the trapping rate.

Plasma developments and parameter scans

Additional optimization studies of the number and density of plasmas should yield higher trapping rates. During the 2017 run we started but did not finish a study of the trapping rate as a function of positron number and density. The author proposes to continue working on this optimization study in 2018:

1. Prepare plasmas with the same density but different radii, by using different well depths during SDREVC while keeping the rotating wall frequency the same.

2. Prepare plasmas with the same radius but different densities, by using different well depths during SDREVC and afterwards applying a rotating wall to normalize the radius.
3. Use the waterbag solver to find the right potential well depth for the mixing well.
4. Test the trapping rate for combination of parameters with at least five trapping cycles for each plasma parameter.

CERN's next long shutdown will take place from 2019-2020, during which there will be no antiprotons produced. This time could be partially used for more plasma-specific studies in the apparatus alongside planned experimental upgrades.

SDREVC on laser-cooled Beryllium ion plasmas

An additional development currently unrelated to antihydrogen studies but likely of interest to the non-neutral plasma community would be to implement SDREVC on the Beryllium ion plasma with active laser cooling. As of now, SDREVC has only been successfully achieved in lepton plasmas. Active non-cyclotron cooling is needed to apply it to ion plasmas. The existing hardware is already in place to develop SDREVC on the laser-cooled Beryllium ion so the author proposes this as a potential project for next year.

Cavity cooling during antihydrogen production

Fajans' group at Berkeley has demonstrated substantially increased cooling rates of electron plasmas in a special cavity electrode. Since the success of synthesis and trapping is greatly influenced by the positron plasma temperature, enhanced cooling during the mixing process should increase the antihydrogen trapping rate. A cavity-enhancing electrode would need to be included in the center of the next electrode stack installled and then the cavity modes in the trap structure would need to be characterized.

Antihydrogen trapping in the ELENA era

If ALPHA is able to catch a factor of a hundred more antiprotons after ELENA begins full operations [47], our entire antiproton cooling, compressing, and trapping sequences will need to be substantially modified. Potential wells will need to be deeper and longer, and most likely we can expect to need a proportional increase in the number of electrons and positrons. Creating, manipulating, and then ejecting electron plasmas with 10^{10} electrons will also require some development. SDREVC has been used for up to 10^9 electrons but will need to be established for 10^{10} electrons. Increasing the number of positrons will likely require a higher transfer efficiency from the accumulator into the atom trap and a longer accumulation time, but it is unclear if we will be able to achieve a factor of a hundred increase in the number of positrons. If not, sympathetic cooling and cavity cooling may play more vital roles.

Antihydrogen production is fundamentally limited by the number of slow antiprotons we can catch. While this author believes the ALPHA collaboration will have to make substantial adjustments to make the best use of the lower-energy beam from ELENA, having a factor of 10-100 increase in antiprotons combined with mK-temperature positrons should make it possible for us to achieve yet a factor of 10-100 increase in the antihydrogen trapping rate and perform fundamental physics symmetry measurements to a much higher precision.

Appendix A

Mathematica code used in finite-temperature calculation

Define constants:

```
ClearAll["Global`*"]

(*constants*)

Subscript[k, b] = 1.3807*10^-23 (*Joules/Kelvin*);
Subscript[m, e] = 9.1094*10^-31 (*kg*);
Subscript[q, e] = 1.6022*10^-19 (*Coulomb*);
B = 1 (*Tesla*);
Temp = 30 (*Kelvin*);
Subscript[r, p] = 0.001(*m*);
Subscript[r, w] = 0.0221 (*m*);
Subscript[n, 0] = 10^14 (*/m^3 *);
\[CapitalOmega] = Subscript[q, e]*B/Subscript[m, e]
Subscript[\[Epsilon], 0] =
  8.8542*10^-12 (*Quantity["PermittivityConstant"]; *);
fudge = 0;
fr = 500000;


(*Density as a function of temperature *)
n[ff_] :=
 2*Subscript[\[Epsilon], 0]*
  B*(2*\[Pi]*ff)/Subscript[q, e] (*n as a function of \[Omega]*)
\[Lambda][nn_, TT_] :=
```

```
 Sqrt[Subscript[\[Epsilon], 0]*Subscript[k, b]*
   TT/(nn*Subscript[q, e]^2)]

\[Gamma][ff_, nn_] := (
  2*Subscript[\[Epsilon], 0]*Subscript[m,
   e]*(2*\[Pi]*ff)*(\[CapitalOmega] - 2*\[Pi]*ff))/(
  nn*Subscript[q, e]^2) - 1

(* Define density equation $n(\gamma)$  from Eq. 4.42  *)


ndens[gg_, ff_] := (
 2*Subscript[\[Epsilon], 0]*Subscript[m,
  e]*(2*\[Pi]*ff)*(\[CapitalOmega] - 2*\[Pi]*ff))/((gg + 1)*Subscript[
  q, e]^2)

function4[T_, f_, g_] :=
 Module[{eq4, s4, \[Lambda]D4, \[Rho]W4, density},
  density = ndens[g, f];
  \[Lambda]D4 = \[Lambda][density, T]; \[Rho]W4 =
   Subscript[r, w]/\[Lambda]D4;
  eq4 = {\[Psi]'[\[Rho]] == \[Alpha][\[Rho]], \[Alpha]'[\[Rho]] ==
     Exp[\[Psi][\[Rho]]] - 1 - g - \[Alpha][\[Rho]]/\[Rho], \[Psi][
      10^-30] == 0, \[Alpha][10^-30] == 0};
  s4 = NDSolve[
    eq4, {\[Psi][\[Rho]], \[Alpha][\[Rho]] }, {\[Rho], 10^-10,
     Max[\[Rho]W4, 10^-5]}];
  (*Print[" This is \[Rho]W: ", \[Rho]W4,
  " This is \[Lambda]D: ", \[Lambda]D4,  " This is density: ",
  density , " This is gamma: ", g];*)
  ((\[Psi][\[Rho]] /. s4) /. \[Rho] -> \[Rho]W4)[[1]]
  (*Plot[\[Psi][\[Rho]]/.s4,{\[Rho],0,7}]*)
  ]


(* Solve $\psi_{desired}$  from Eq. 4.46 *)



psiDesired4[T2_, f_, V_] :=
 V*Subscript[q, e]/(Subscript[k, b]*T2) -
  Subscript[m, e]*2*\[Pi]*f*(\[CapitalOmega] - 2*\[Pi]*f)*
```

```
   Subscript[r,
     w]^2/(2*Subscript[k, b]*
      T2) (* the paper specifies that  phi is zero at the origin; phi \
must equal V at the wall, so V must be positive*)
ri4[T2_, f_, V_] := Block[{root, psiTarget},
  psiTarget = psiDesired4[T2, f, V];
  root = FindRoot[
    function4[T2, f, 10^g1] == psiTarget, {g1, -15, 15} ,
    Evaluated -> False(*,PrecisionGoal\[Rule].1*)];
  (10^g1 /. root)]


(*plot density as a function of temperature for different RW frequencies*)
p0 = ListPlot[
   Table[{T3,
     1/(ndens[ri4[30, 100000, 3], 100000])*
      ndens[ri4[T3, 100000, 3], 100000]}, {T3, 30, 3000, 30}],
   PlotLegends -> {"f=100 kHz"}, PlotStyle -> Magenta];
p1 = ListPlot[
   Table[{T3,
     1/(ndens[ri4[30, 500000, 3], 500000])*
      ndens[ri4[T3, 500000, 3], 500000]}, {T3, 30, 3000, 30}],
   PlotLegends -> {"f=500 kHz"}];
p2 = ListPlot[
   Table[{T3,
     1/(ndens[ri4[30, 1000000, 3], 1000000])*
      ndens[ri4[T3, 1000000, 3], 1000000]}, {T3, 30, 3000, 10}],
   PlotLegends -> {"f=1000 kHz"}, PlotStyle -> Yellow];
p3 = ListPlot[
   Table[{T3,
     1/(ndens[ri4[30, 15000000, 3], 15000000])*
      ndens[ri4[T3, 1500000, 3], 1500000]}, {T3, 30, 3000, 10}],
   PlotLegends -> {"f=1500 kHz"}, PlotStyle -> Green];




Show[p0, p1, p2, p3,
 AxesLabel -> {"Temperature (K)",
   "Density (\!\(\*SuperscriptBox[\(m\), \(-3\)]\)) normalized by \
value at T=30K"}, PlotRange -> {{0, 300}, {0.98, 1}}]
```

```
(*Integrate over the density distribution to the wall  to calculate
 the number of particles in the plasma as a function of temperature,
 for  different options of $\phi_c$  being slightly lower
 (by factors of $k_bT$) than the potential well depth. EVClists
 are lists of the integrated number of particles calculated at different
  temperatures. EVClist1 calculates for $phi_c=V_well$, EVClist2
   calculates for $phi_c=V_well-k_bT$ and EVClist3 calculates for
    phi_c-2*k_bT. *)


EVClist1 = {};
Do[
T1 = 30*i; f1 = 500000; V1 = 1.8 - 0*T1*8.61733*10^(-5);
n0 = ndens[ri4[T1, f1, V1], f1]; (*central density *)
\[Lambda]D5 = \[Lambda][ndens[ri4[T1, f1, V1], f1], T1];
\[Rho]W5 = Subscript[r, w]/\[Lambda]D5;
eq5 = {\[Psi]'[\[Rho]] == \[Alpha][\[Rho]], \[Alpha]'[\[Rho]] ==
   Exp[\[Psi][\[Rho]]] - 1 -
    ri4[T1, f1, V1] - \[Alpha][\[Rho]]/\[Rho], \[Psi][10^-30] ==
   0, \[Alpha][10^-30] == 0};
s5 = NDSolve[
 eq5, {\[Psi][\[Rho]], \[Alpha][\[Rho]] }, {\[Rho],
   10^-10, \[Rho]W5}];
points1 =
 Table[{\[Rho],
   2*\[Pi]*\[Rho]*\[Lambda]D5^2*n0*
    Exp[\[Psi][\[Rho]] /. s5][[1]]}, {\[Rho], 0, 30, 0.1}];
intfunc1 = Interpolation[points1, InterpolationOrder -> 3];
t2 = {T1, Integrate[intfunc1[\[Rho]], {\[Rho], 0, 30}]*0.05};
AppendTo[EVClist1, t2], {i, 1, 10}]


EVClist2 = {};
Do[
T1 = 30*i; f1 = 500000; V1 = 1.8 - 1*T1*8.61733*10^(-5);
n0 = ndens[ri4[T1, f1, V1], f1]; (*central density *)
\[Lambda]D5 = \[Lambda][ndens[ri4[T1, f1, V1], f1], T1];
\[Rho]W5 = Subscript[r, w]/\[Lambda]D5;
eq5 = {\[Psi]'[\[Rho]] == \[Alpha][\[Rho]], \[Alpha]'[\[Rho]] ==
```

```
   Exp[\[Psi][\[Rho]]] - 1 -
    ri4[T1, f1, V1] - \[Alpha][\[Rho]]/\[Rho], \[Psi][10^-30] ==
   0, \[Alpha][10^-30] == 0};


s5 = NDSolve[
  eq5, {\[Psi][\[Rho]], \[Alpha][\[Rho]] }, {\[Rho],
   10^-10, \[Rho]W5}];
points1 =
 Table[{\[Rho],
   2*\[Pi]*\[Rho]*\[Lambda]D5^2*n0*
    Exp[\[Psi][\[Rho]] /. s5][[1]]}, {\[Rho], 0, 30, 0.1}];
intfunc1 = Interpolation[points1, InterpolationOrder -> 3];
t2 = {T1, Integrate[intfunc1[\[Rho]], {\[Rho], 0, 30}]*0.05};
AppendTo[EVClist2, t2], {i, 1, 10}]

EVClist3 = {};
Do[
 T1 = 30*i; f1 = 500000; V1 = 1.8 - 3*T1*8.61733*10^(-5);
 n0 = ndens[ri4[T1, f1, V1], f1]; (*central density *)
 \[Lambda]D5 = \[Lambda][ndens[ri4[T1, f1, V1], f1], T1];
 \[Rho]W5 = Subscript[r, w]/\[Lambda]D5;
 eq5 = {\[Psi]'[\[Rho]] == \[Alpha][\[Rho]], \[Alpha]'[\[Rho]] ==
    Exp[\[Psi][\[Rho]]] - 1 -
     ri4[T1, f1, V1] - \[Alpha][\[Rho]]/\[Rho], \[Psi][10^-30] ==
    0, \[Alpha][10^-30] == 0};
 s5 = NDSolve[
   eq5, {\[Psi][\[Rho]], \[Alpha][\[Rho]] }, {\[Rho],
    10^-10, \[Rho]W5}];
 points1 =
  Table[{\[Rho],
    2*\[Pi]*\[Rho]*\[Lambda]D5^2*n0*
     Exp[\[Psi][\[Rho]] /. s5][[1]]}, {\[Rho], 0, 30, 0.1}];
 intfunc1 = Interpolation[points1, InterpolationOrder -> 3];
 t2 = {T1, Integrate[intfunc1[\[Rho]], {\[Rho], 0, 30}]*0.05};
 AppendTo[EVClist3, t2], {i, 1, 10}]

(*prepare plots of number of particles as a function of temperature  *)

plot1 = ListPlot[Table[EVClist1, 1], PlotStyle -> Orange,
   PlotLegends -> {"Space charge=1.8V-0*\!\(\*SubscriptBox[\(k\), \(b\
\)]\)*T"}, AxesLabel -> {"Temperature (K)", "Number of particles"},
```

```
   PlotLabel ->
    "Number of Particles vs. Temperature in a 5 cm long plasma with \
RW_f=100 kHz and V_well=2 Volts/2 Volts-4*\!\(\*SubscriptBox[\(k\), \
\(b\)]\)*T in eV"];
plot2 = ListPlot[Table[EVClist2, 1], PlotStyle -> Brown,
   PlotLegends -> {"Space charge=1.8V-1*\!\(\*SubscriptBox[\(k\), \(b\
\)]\)*T"}, AxesLabel -> {"Temperature (K)", "Number of particles"},
   PlotLabel ->
    "Number of Particles vs. Temperature in a 5 cm long plasma with \
RW_f=100 kHz and V_well=2 Volts/2 Volts-4*\!\(\*SubscriptBox[\(k\), \
\(b\)]\)*T in eV"];
plot3 = ListPlot[Table[EVClist3, 1], PlotStyle -> Blue,
   PlotLegends -> {"Space charge=1.8V-3*\!\(\*SubscriptBox[\(k\), \(b\
\)]\)*T"}, AxesLabel -> {"Temperature (K)", "Number of particles"},
   PlotLabel ->
    "Number of Particles vs. Temperature in a 5 cm long plasma with \
RW_f=100 kHz and V_well=2 Volts/2 Volts-4*\!\(\*SubscriptBox[\(k\), \
\(b\)]\)*T in eV"];
Show[plot1, plot2, plot3, PlotRange -> All]
```

Bibliography

[1] M. Aguilar et al. "First Result from the Alpha Magnetic Spectrometer on the International Space Station: Precision Measurement of the Positron Fraction in Primary Cosmic Rays of 0.5-350 GeV". In: *Phys. Rev. Lett.* 110 (14 2013), p. 141102. DOI: 10.1103/PhysRevLett.110.141102. URL: https://link.aps.org/doi/10.1103/PhysRevLett.110.141102.

[2] Gaëlle Giesen et al. "AMS-02 antiprotons, at last! Secondary astrophysical component and immediate implications for Dark Matter". In: *Journal of Cosmology and Astroparticle Physics* 2015.09 (2015), p. 023. URL: http://stacks.iop.org/1475-7516/2015/i=09/a=023.

[3] K. Abe et al. "The results from BESS-Polar experiment". In: *Advances in Space Research* 60.4 (2017). Solar Energetic Particles, Solar Modulation and Space Radiation: New Opportunities in the AMS-02 Era, pp. 806 –814. ISSN: 0273-1177. DOI: https://doi.org/10.1016/j.asr.2016.11.004. URL: http://www.sciencedirect.com/science/article/pii/S0273117716306305.

[4] G. Bressi et al. "Testing the neutrality of matter by acoustic means in a spherical resonator". In: *Phys. Rev. A* 83 (5 2011), p. 052101. DOI: 10.1103/PhysRevA.83.052101. URL: https://link.aps.org/doi/10.1103/PhysRevA.83.052101.

[5] M. Ahmadi et al. "An improved limit on the charge of antihydrogen from stochastic acceleration". In: *Nature* 529 (2016), p. 373. DOI: doi:10.1038/nature16491.

[6] R.P. Feynman, R.B. Leighton, and M.L. Sands. *The Feynman Lectures on Physics*. The Feynman Lectures on Physics v. 1. Addison-Wesley, 1963. Chap. 52. ISBN: 9780201021165.

[7] A. Einstein. "Die Grundlage der allgemeinen Relativitätstheorie". In: *Annalen der Physik* 354.7 (), pp. 769–822. DOI: 10.1002/andp.19163540702. eprint: https://onlinelibrary.wiley.com/doi/pdf/10.1002/andp.19163540702. URL: https://onlinelibrary.wiley.com/doi/abs/10.1002/andp.19163540702.

[8] B. P. Abbott et al. "GW170814: A Three-Detector Observation of Gravitational Waves from a Binary Black Hole Coalescence". In: *Phys. Rev. Lett.* 119 (14 2017), p. 141101. DOI: 10.1103/PhysRevLett.119.141101. URL: https://link.aps.org/doi/10.1103/PhysRevLett.119.141101.

[9] E. G. Adelberger et al. "Does antimatter fall with the same acceleration as ordinary matter?" In: *Phys. Rev. Lett.* 66 (1991), pp. 850–853. DOI: 10.1103/PhysRevLett.66.850.

[10] R. J. Hughes and M. H. Holzcheiter. "Constraints on the gravitational properties of antiprotons and positrons from cyclotron-frequency measurements." In: *Physics Review Letters* 66 (1991), pp. 854–857.

[11] T. Goldman, M. V. Hynes, and M. M. Nieto. "The gravitational acceleration of antiprotons". In: *General relativity and gravitation* 18.1 (1986), pp. 67–70.

[12] G. Chardin. "Motivations for antigravity in General Relativity." In: *Hyperfine Interact.* 109 (1997), pp. 83–94.

[13] C. Amole et al. "Description and first application of a new technique to measure the gravitational mass of antihydrogen". In: *Nature Communications* 4 (2013), p. 1785. DOI: https://doi.org/10.1038/ncomms2787.

[14] Paul Hamilton et al. "Antimatter Interferometry for Gravity Measurements". In: *Phys. Rev. Lett.* 112 (12 2014), p. 121102. DOI: 10.1103/PhysRevLett.112.121102.

[15] P. A. M. Dirac. "The quantum theory of the electron". In: *Proceedings of the Royal Society A* 117 (1928), p. 778.

[16] C. D. Anderson. "The Positive Electron". In: *Physical Review* 43 (1933), p. 491.

[17] Roy F Schwitters and Karl Strauch. "The Physics of e+ e Collisions". In: *Annual Review of Nuclear Science* 26.1 (1976), pp. 89–149.

[18] S Behrends et al. "Inclusive hadron production in upsilon decays and in nonresonant electron-positron annihilation at 10.49 GeV". In: *Physical Review D* 31.9 (1985), p. 2161.

[19] Kenji Abe et al. "High-Precision Measurement of the Left-Right Z Boson Cross-Section Asymmetry". In: *Phys. Rev. Lett.* 84 (26 2000), pp. 5945–5949. DOI: 10.1103/PhysRevLett.84.5945. URL: https://link.aps.org/doi/10.1103/PhysRevLett.84.5945.

[20] Frédéric Joliot and Irène Curie. "Artificial production of a new kind of radio-element". In: 122 (1934).

[21] ZH Cho, JK Chan, and L Eriksson. "Circular ring transverse axial positron camera for 3-dimensional reconstruction of radionuclides distribution". In: *IEEE Transactions on Nuclear Science* 23.1 (1976), pp. 613–622.

[22] Michael E Phelps et al. "Application of annihilation coincidence detection to transaxial reconstruction tomography". In: *Journal of Nuclear Medicine* 16.3 (1975), pp. 210–224.

[23] Henry N. Wagner. "A brief history of positron emission tomography (PET)". In: *Seminars in Nuclear Medicine* 28.3 (1998). The Coming Age of Pet (Part 1), pp. 213 –220. ISSN: 0001-2998. DOI: https://doi.org/10.1016/S0001-2998(98)80027-5. URL: http://www.sciencedirect.com/science/article/pii/S0001299898800275.

[24] *PET Scan*. https://patient.info/health/pet-scan. Accessed: 2018-05-31.

[25] Owen Chamberlain et al. "Observation of Antiprotons". In: *Phys. Rev.* 100 (3 1955), pp. 947–950. DOI: 10.1103/PhysRev.100.947. URL: http://link.aps.org/doi/10.1103/PhysRev.100.947.

[26] O. Chamberlain et al. "On the observation of an antiproton star in emulsion exposed at the bevatron". In: *Il Nuovo Cimento (1955-1965)* 3.2 (1956), pp. 447–467. ISSN: 1827-6121. DOI: 10.1007/BF02745430. URL: https://doi.org/10.1007/BF02745430.

[27] F. Abe et al. "Evidence for top quark production in $\bar{p}p$ collisions at $\sqrt{s} = 1.8TeV$". In: *Phys. Rev. Lett.* 73 (2 July 1994), pp. 225–231. DOI: 10.1103/PhysRevLett.73.225. URL: https://link.aps.org/doi/10.1103/PhysRevLett.73.225.

[28] F. Abe et al. "Observation of Top Quark Production in $\bar{p}p$ Collisions with the Collider Detector at Fermilab". In: *Phys. Rev. Lett.* 74 (14 1995), pp. 2626–2631. DOI: 10.1103/PhysRevLett.74.2626. URL: https://link.aps.org/doi/10.1103/PhysRevLett.74.2626.

[29] S. Abachi et al. "Observation of the Top Quark". In: *Phys. Rev. Lett.* 74 (14 1995), pp. 2632–2637. DOI: 10.1103/PhysRevLett.74.2632. URL: https://link.aps.org/doi/10.1103/PhysRevLett.74.2632.

[30] by Cian O'Luanaigh. "Protons set to collide at 13 TeV to prepare for physics". In: (2015). URL: http://cds.cern.ch/record/2024983.

[31] "The Low Energy Antiproton Ring". In: (2012). URL: http://cds.cern.ch/record/1997347.

[32] G. Baur et al. "Production of antihydrogen". In: *Physics Letters B* 368.3 (1996), pp. 251 –258. ISSN: 0370-2693. DOI: https://doi.org/10.1016/0370-2693(96)00005-6. URL: http://www.sciencedirect.com/science/article/pii/0370269396000056.

[33] Nina Hall. *FACILITY FOR ANTIPROTON AND ION RESEARCH*. Brochure. 2013. URL: https://fair-center.eu/fileadmin/fair/publications_FAIR/FAIR_Broschuere_autumn2013_V3_72dpi.pdf.

[34] D. Durkin. "Experiments on 2D vortex patterns in a Malmberg-Penning Trap with a photocathode". PhD thesis. University of California, Berkeley, 1998.

[35] V L Galansky et al. "Physical processes in plasma electron emitters based on a hollow-cathode reflected discharge". In: *Journal of Physics D: Applied Physics* 27.5 (1994), p. 953. URL: http://stacks.iop.org/0022-3727/27/i=5/a=012.

[36] C. Amole et al. "The ALPHA antihydrogen trapping apparatus". In: *Nucl. Instr. Meth. Phys. Res. A* 735 (2014), pp. 319 –340. DOI: http://dx.doi.org/10.1016/j.nima.2013.09.043.

[37] G. Gabrielse et al. "Antihydrogen Production within a Penning-Ioffe Trap". In: *Phys. Rev. Lett.* 100 (2008). ATRAP Collaboration, p. 113001.

[38] S. Aghion et al. "Positron bunching and electrostatic transport system for the production and emission of dense positronium clouds into vacuum". In: *Nuclear Instruments and Methods in Physics Research Section B: Beam Interactions with Materials and Atoms* 362 (2015), pp. 86 –92. ISSN: 0168-583X. DOI: https://doi.org/10.1016/j.nimb.2015.08.097. URL: http://www.sciencedirect.com/science/article/pii/S0168583X15008708.

[39] P Perez and Y Sacquin. "The GBAR experiment: gravitational behaviour of antihydrogen at rest". In: *Classical and Quantum Gravity* 29.18 (2012), p. 184008. URL: http://stacks.iop.org/0264-9381/29/i=18/a=184008.

[40] H Saitoh et al. "Recent status of A Positron-Electron Experiment (APEX)". In: *Journal of Physics: Conference Series* 505.1 (2014), p. 012045. URL: http://stacks.iop.org/1742-6596/505/i=1/a=012045.

[41] Christoph Hugenschmidt et al. "The NEPOMUC upgrade and advanced positron beam experiments". In: *New Journal of Physics* 14.5 (2012), p. 055027. URL: http://stacks.iop.org/1367-2630/14/i=5/a=055027.

[42] Hui Chen et al. "Relativistic Positron Creation Using Ultraintense Short Pulse Lasers". In: *Phys. Rev. Lett.* 102 (10 2009), p. 105001. DOI: 10.1103/PhysRevLett.102.105001. URL: https://link.aps.org/doi/10.1103/PhysRevLett.102.105001.

[43] "Linear accelerator 2". In: (2012). URL: http://cds.cern.ch/record/1997427.

[44] "The Proton Synchrotron". In: (2012). URL: http://cds.cern.ch/record/1997189.

[45] by Iva Raynova and Iva Maksimova Raynova. "SPS: last injector back up and running". In: (2017). URL: http://cds.cern.ch/record/2261792.

[46] Esma Anais Mobs. "The CERN accelerator complex. Complexe des accélérateurs du CERN". In: (2016). General Photo. URL: https://cds.cern.ch/record/2225847.

[47] *Main page*. https://espace.cern.ch/elena-project/sitepages/home.aspx. 2018. (Visited on 05/06/2018).

[48] G. Gabrielse et al. "Cooling and slowing of trapped antiprotons below 100meV". In: *Phys. Rev. Lett.* 63 (1989), p. 1360. DOI: 10.1103/PhysRevLett.63.1360.

[49] Tommy Eriksson. "AD: low-energy antiproton production at CERN". In: *Hyperfine Interactions* 194.1 (Oct. 2009), p. 123. ISSN: 1572-9540. DOI: 10.1007/s10751-009-0039-0. URL: https://doi.org/10.1007/s10751-009-0039-0.

[50] *Votre prix de l'électricité dans la commune de Genève*. https://www.prix-electricite.elcom.admin.ch/PriceDetail.aspx?Period=2018&PlaceNumber=6621&OpID=692&CatID=15&ProdID=10&CPeriod=2017&CPlaceNumber=6621&COpID=692&CCatID=15&CProdID=1&DetailData=Comp. 2018. (Visited on 04/21/2018).

[51] G R. Schmidt et al. "Antimatter Requirements and Energy Costs for Near-Term Propulsion Applications". In: 16 (Sept. 2000), pp. 923–928.

[52] by Stefania Pandolfi and Stefania Pandolfi. "The BASE antiprotons celebrate their first birthday". In: (2016). URL: http://cds.cern.ch/record/2239995.

[53] H Nagahama et al. "Sixfold improved single particle measurement of the magnetic moment of the antiproton". In: *Nature communications* 8 (2017), p. 14084.

[54] C Smorra et al. "A parts-per-billion measurement of the antiproton magnetic moment". In: *Nature* 550.7676 (2017), p. 371.

[55] Masaki Hori et al. "Buffer-gas cooling of antiprotonic helium to 1.5 to 1.7 K, and antiproton-to–electron mass ratio". In: *Science* 354.6312 (2016), pp. 610–614. ISSN: 0036-8075. DOI: 10.1126/science.aaf6702. eprint: http://science.sciencemag.org/content/354/6312/610.full.pdf. URL: http://science.sciencemag.org/content/354/6312/610.

[56] G. Blanford et al. "Observation of Atomic Antihydrogen". In: *Phys. Rev. Lett.* 80 (14 1998), pp. 3037–3040. DOI: 10.1103/PhysRevLett.80.3037. URL: http://link.aps.org/doi/10.1103/PhysRevLett.80.3037.

[57] M. Amoretti et al. "Production and Detection of Cold Antihydrogen Atoms". In: *Nature* 419 (2002), pp. 456–459. DOI: 10.1038/nature01096.

[58] G. Gabrielse et al. "Driven Production of Cold Antihydrogen and the First Measured Distribution of Antihydrogen States". In: *Phys. Rev. Lett.* 89 (23 2002), p. 233401. DOI: 10.1103/PhysRevLett.89.233401.

[59] G. B. Andresen et al. "Trapped Antihydrogen". In: *Nature* 468 (2010), pp. 673–676. DOI: 10.1038/nature09610.

[60] G. B. Andresen et al. "Confinement of antihydrogen for 1000 seconds". In: *Nature Phys.* 7 (2011), pp. 558–564. DOI: 10.1038/NPHYS2025.

[61] N Kuroda et al. "A source of antihydrogen for in-flight hyperfine spectroscopy". In: *Nature communications* 5 (2014), p. 3089.

[62] M. Ahmadi et al. "Observation of the 1S-2S transition in trapped antihydrogen". In: *Nature* 541 (2017), p. 506. DOI: doi:10.1038/nature21040.

[63] M. Ahmadi et al. "Characterization of the 1S-2S transition in antihydrogen". In: *Nature* (2018). DOI: doi:10.1038/s41586-018-0017-2.

[64] M. Ahmadi et al. "Observation of the hyperfine spectrum of antihydrogen". In: *Nature* 548 (2017), p. 66. DOI: doi:10.1038/nature23446.

[65] M. Ahmadi et al. "Enhanced Control and Reproducibility of Non-Neutral Plasmas". In: *Phys. Rev. Lett.* 120 (2 2018), p. 025001. DOI: 10.1103/PhysRevLett.120.025001. URL: https://link.aps.org/doi/10.1103/PhysRevLett.120.025001.

[66] C. So. "Antiproton and positron dynamics in antihydrogen production". PhD thesis. University of California, Berkeley, 2014.

[67] G. Gabrielse et al. "Possible antihydrogen production using trapped plasmas". In: *Hyperfine Interactions* 44.1 (Mar. 1989), pp. 287–293. ISSN: 1572-9540. DOI: 10.1007/BF02398677. URL: https://doi.org/10.1007/BF02398677.

[68] J. Stevefelt, J. Boulmer, and J F. Delpech. "Collisional-radiative recombination in cold plasmas". In: *Phys. Rev. A* 12 (4 1975), pp. 1246–1251. DOI: 10.1103/PhysRevA.12.1246. URL: https://link.aps.org/doi/10.1103/PhysRevA.12.1246.

[69] M Amoretti et al. "Antihydrogen production temperature dependence". In: *Physics Letters B* 583.1 (2004), pp. 59 –67. ISSN: 0370-2693. DOI: https://doi.org/10.1016/j.physletb.2004.01.009. URL: http://www.sciencedirect.com/science/article/pii/S0370269304000905.

[70] Michael E. Glinsky and Thomas M. O'Neil. "Guiding center atoms: Three-body recombination in a strongly magnetized plasma". In: *Physics of Fluids B: Plasma Physics* 3.5 (1991), pp. 1279–1293. DOI: 10.1063/1.859820. eprint: https://doi.org/10.1063/1.859820. URL: https://doi.org/10.1063/1.859820.

[71] F. Robicheaux. "Simulations of antihydrogen formation". In: *Phys. Rev. A* 70 (2 2004), p. 022510. DOI: 10.1103/PhysRevA.70.022510. URL: https://link.aps.org/doi/10.1103/PhysRevA.70.022510.

[72] F. Robicheaux. "Three-body recombination for electrons in a strong magnetic field: Magnetic moment". In: *Phys. Rev. A* 73 (3 2006), p. 033401. DOI: 10.1103/PhysRevA.73.033401. URL: https://link.aps.org/doi/10.1103/PhysRevA.73.033401.

[73] Michael H. Holzscheiter, Michael Charlton, and Michael Martin Nieto. "The route to ultra-low energy antihydrogen". In: *Physics Reports* 402.1 (2004), pp. 1 –101. ISSN: 0370-1573. DOI: https://doi.org/10.1016/j.physrep.2004.08.002. URL: http://www.sciencedirect.com/science/article/pii/S037015730400300X.

[74] Robert S. Van Dyck, Paul B. Schwinberg, and Hans G. Dehmelt. "New high-precision comparison of electron and positron g factors". In: *Phys. Rev. Lett.* 59 (1 1987), pp. 26–29. DOI: 10.1103/PhysRevLett.59.26. URL: https://link.aps.org/doi/10.1103/PhysRevLett.59.26.

[75] C. Amole et al. "Experimental and computational study of the injection of antiprotons into a positron plasma for antihydrogen production". In: *Phys. Plasma* 20 (2013), p. 043510. DOI: 10.1063/1.4801067.

[76] Edward A. Estalote and K. G. Ramanathan. "Low-temperature emissivities of copper and aluminum". In: *J. Opt. Soc. Am.* 67.1 (1977), pp. 39–44. DOI: 10.1364/JOSA.67.000039. URL: http://www.osapublishing.org/abstract.cfm?URI=josa-67-1-39.

[77] J. Fajans and A. Schmidt. "Malmberg-Penning and Minimum-B Trap compatibility: the advantages of higher-order multipole traps". In: *Nucl. Instr. Meth. Phys. Res. A* 521 (2004), p. 318. DOI: 10.1016/j.nima.2003.11.194.

[78] WA Bertsche et al. "Physics with antihydrogen". In: *Journal of Physics B: Atomic, Molecular and Optical Physics* 48.23 (2015), p. 232001.

[79] C. Amole et al. "Silicon vertex detector upgrade in the {ALPHA} experiment". In: *Nucl. Inst. Meth. Phys. Res. A* 732.0 (2013). Vienna Conference on Instrumentation 2013, pp. 134 –136. ISSN: 0168-9002. DOI: http://dx.doi.org/10.1016/j.nima.2013.05.188.

[80] C. Baltay et al. "Annihilations of Antiprotons at Rest in Hydrogen. V. Multipion Annihilations". In: *Phys. Rev.* 145 (4 1966), pp. 1103–1111. DOI: 10.1103/PhysRev.145.1103. URL: https://link.aps.org/doi/10.1103/PhysRev.145.1103.

[81] S.J. Orfanidis and V. Rittenberg. "Nucleon-antinucleon annihilation into pions". In: *Nuclear Physics B* 59.2 (1973), pp. 570 –582. ISSN: 0550-3213. DOI: https://doi.org/10.1016/0550-3213(73)90660-3. URL: http://www.sciencedirect.com/science/article/pii/0550321373906603.

[82] C. Amole et al. "Alternative method for reconstruction of antihydrogen annihilation vertices". English. In: *Hyperfine Interactions* 212.1-3 (2012), pp. 101–107. ISSN: 0304-3843. DOI: 10.1007/s10751-012-0588-5.

[83] Ilya Narsky. "StatPatternRecognition: a C++ package for statistical analysis of high energy physics data". In: (2005). arXiv: 0507143 [physics.data-a].

[84] Ilya Narsky. "Optimization of signal significance by bagging decision trees". In: (2005). arXiv: 0507157 [physics.data-a].

[85] G. B. Andresen et al. "Antihydrogen Annihilation Reconstruction with the ALPHA Silicon Detector". In: *Nucl. Instr. Meth. Phys. Res. A* 684 (2012), pp. 73–81. DOI: 10.1016/j.nima.2012.04.082.

[86] "How an MCP works". In: (2018). URL: https://www.photonis.com/how-mcp-works.

[87] G. B. Andresen et al. "Antiproton, positron, and electron imaging with a microchannel plate/phosphor detector". In: *Rev. Sci. Instrum.* 80 (2009). ALPHA Collaboration, p. 123701.

[88] J. L. Wiza. "Microchannel Plate Detectors". In: *Nucl. Instrum. and Methods* 162 (1979), p. 587.

[89] D. L. Eggleston et al. "Parallel Energy Analyzer for Pure Electron Plasma Devices". In: *Phys. Fluids B* 4 (1992), p. 3432.

[90] A. P. Mills Jr. and E. M. Gullikson. "Solid neon moderator for producing slow positrons". In: *Applied Physics Letters* 49.17 (1986), pp. 1121–1123. DOI: 10.1063/1.97441. URL: http://link.aip.org/link/?APL/49/1121/1.

[91] T. J. Murphy and C. M. Surko. "Positron trapping in an electrostatic well by inelastic collisions with nitrogen molecules". In: *Phys. Rev. A* 46 (1992), pp. 5696–5705. DOI: 10.1103/PhysRevA.46.5696.

[92] *Main page*. https://midas.triumf.ca/MidasWiki/index.php/Main_Page. 2018. (Visited on 05/03/2018).

[93] C. Amole et al. "In situ electromagnetic field diagnostics with an electron plasma in a Penning-Malmberg trap". In: *New Journal of Physics* 16 (2014), p. 013037. DOI: doi:10.1088/1367-2630/16/1/013037.

[94] T. Friesen. "Probing Trapped Antihydrogen: In Situ Diagnostics and Observations of Quantum Transitions". PhD thesis. University of Calgary, 2014.

[95] A. P. Povilus et al. "Electron Plasmas Cooled by Cyclotron-Cavity Resonance". In: *Phys. Rev. Lett.* 117 (17 2016), p. 175001. DOI: 10.1103/PhysRevLett.117.175001. URL: https://link.aps.org/doi/10.1103/PhysRevLett.117.175001.

[96] G. B. Andresen et al. "Compression of antiproton clouds for antihydrogen trapping". In: *Phys. Rev. Lett.* 100 (2008). ALPHA Collaboration, p. 203401. DOI: 10.1103/PhysRevLett.100.203401.

[97] G. B. Andresen et al. "Centrifugal Separation and Equilibration Dynamics in an Electron-Antiproton Plasma". In: *Phys. Rev. Lett.* 106.14 (2011), p. 145001. DOI: 10.1103/PhysRevLett.106.145001.

[98] Wolfgang Paul and Helmut Steinwedel. "Ein neues massenspektrometer ohne magnetfeld". In: *Zeitschrift für Naturforschung A* 8.7 (1953), pp. 448–450.

[99] W. Paul, H. P. Reinhard, and U. Von Zahn. "Das elektrische Massenfilter als Massenspektrometer und Isotopentrenner". In: *Zeitschrift für Physik* 152.2 (1958), pp. 143–182. DOI: 10.1007/bf01327353.

[100] "Experiments with an isolated subatomic particle at rest (Nobel Lecture)". In: *Angewandte Chemie International Edition in English* 29 (1990).

[101] Wolfgang Paul. "Electromagnetic traps for charged and neutral particles". In: *Rev. Mod. Phys.* 62 (3 1990), pp. 531–540. DOI: 10.1103/RevModPhys.62.531. URL: https://link.aps.org/doi/10.1103/RevModPhys.62.531.

[102] "The Nobel Prize in Physics 1989". In: *Nobel Media AB* (2014). URL: https://www.nobelprize.org/nobel_prizes/physics/laureates/1989/.

[103] A. G. Marshall. "Milestones in fourier transform ion cyclotron resonance mass spectrometry technique development". In: *Int. J. Mass Spect.* 200 (2000), p. 331. DOI: http://dx.doi.org/10.1016/S1387-3806(00)00324-9.

[104] MG Raizen et al. "Ionic crystals in a linear Paul trap". In: *Physical Review A* 45.9 (1992), p. 6493.

[105] S. Mavadia et al. "Control of the conformations of ion Coulomb crystals in a Penning trap". In: *Nature Communications* 4 (2013), p. 2571. DOI: http://doi.org/10.1038/ncomms3571.

[106] J. J. Bollinger, D. J. Wineland, and Daniel H. E. Dubin. "Non-neutral ion plasmas and crystals, laser cooling, and atomic clocks". In: *Phys. Plasmas* 1 (1994), p. 1403. DOI: 10.1063/1.870690.

[107] M Hellwig et al. "Fabrication of a planar micro Penning trap and numerical investigations of versatile ion positioning protocols". In: *New Journal of Physics* 12.6 (2010), p. 065019. URL: http://stacks.iop.org/1367-2630/12/i=6/a=065019.

[108] A.J. Peurrung, R.T. Kouzes, and S.E. Barlow. "The non-neutral plasma: an introduction to physics with relevance to cyclotron resonance mass spectrometry". In: *International Journal of Mass Spectrometry and Ion Processes* 157-158 (1996), pp. 39 –83. ISSN: 0168-1176. DOI: https://doi.org/10.1016/S0168-1176(96)04395-9. URL: http://www.sciencedirect.com/science/article/pii/S0168117696043959.

[109] R. C. Davidson. *Physics of Nonneutral Plasmas*. Redwood City: Addison-Wesley, 1990.

[110] T. M. O'Neil. "A Confinement Theorem for Nonneutral Plasmas". In: *Phys. Fluids* 23 (1980), p. 2216.

[111] F. Anderegg, E. M. Hollman, and C. F. Driscoll. "Rotating Field Confinement of Pure Electron Plasmas Using Trivelpiece-Gould Modes". In: *Phys. Rev. Lett.* 81 (1998), p. 4875.

[112] X.-P. Huang et al. "Steady-state confinement of non-neutral plasmas by rotating electric fields". In: *Phys. Rev. Lett.* 78 (1997), p. 875.

[113] F. Anderegg, E. M. Hollmann, and C. F. Driscoll. "Steady-state confinement of electron plasmas using trivelpiece-gould modes excited by a "rotating wall"". In: *AIP Conference Proceedings* 457.1 (1999), pp. 277–283. DOI: 10.1063/1.57466. eprint: https://aip.scitation.org/doi/pdf/10.1063/1.57466. URL: https://aip.scitation.org/doi/abs/10.1063/1.57466.

[114] Leon Brillouin. "A Theorem of Larmor and Its Importance for Electrons in Magnetic Fields". In: *Phys. Rev.* 67 (7-8 1945), pp. 260–266. DOI: 10.1103/PhysRev.67.260. URL: https://link.aps.org/doi/10.1103/PhysRev.67.260.

[115] F. Anderegg et al. "Thermally Excited Modes in a Pure Electron Plasma". In: *Phys. Rev. Lett.* 90 (11 2003), p. 115001. DOI: 10.1103/PhysRevLett.90.115001. URL: https://link.aps.org/doi/10.1103/PhysRevLett.90.115001.

[116] AW Trivelpiece and RW Gould. "Space charge waves in cylindrical plasma columns". In: *Journal of Applied Physics* 30.11 (1959), pp. 1784–1793.

[117] J. R. Danielson and C. M. Surko. "Torque-balanced high-density steady states of single-component plasmas". In: *Phys. Rev. Lett.* 94 (2005), p. 035001. DOI: 10.1103/PhysRevLett.94.035001.

[118] J. R. Danielson and C. M. Surko. "Radial compression and torque-balanced steady states of single-component plasmas in Penning-Malmberg traps". In: *Phys. Plasmas* 13.5, 055706 (2006), p. 055706. DOI: 10.1063/1.2179410.

[119] J. Larmor D.Sc. F.R.S. "LXIII. On the theory of the magnetic influence on spectra; and on the radiation from moving ions". In: *The London, Edinburgh, and Dublin Philosophical Magazine and Journal of Science* 44.271 (1897), pp. 503–512. DOI: 10.1080/14786449708621095.

[120] J. H. Malmberg et al. "Experiments with pure electron plasmas". In: *AIP Conference Proceedings* 175.1 (1988), pp. 28–74. DOI: 10.1063/1.37613. eprint: https://aip.scitation.org/doi/pdf/10.1063/1.37613. URL: https://aip.scitation.org/doi/abs/10.1063/1.37613.

[121] E. M. Purcell, H. C. Torrey, and R. V. Pound. "Resonance Absorption by Nuclear Magnetic Moments in a Solid". In: *Phys. Rev.* 69 (1-2 1946), pp. 37–38. DOI: 10.1103/PhysRev.69.37. URL: https://link.aps.org/doi/10.1103/PhysRev.69.37.

[122] N. Evetts et al. "Open microwave cavity for use in a Purcell enhancement cooling scheme". In: *Review of Scientific Instruments* 87.10 (2016), p. 104702. DOI: 10.1063/1.4963856. eprint: https://doi.org/10.1063/1.4963856. URL: https://doi.org/10.1063/1.4963856.

[123] E. D. Hunter et al. "Low magnetic field cooling of lepton plasmas via cyclotron-cavity resonance". In: *Physics of Plasmas* 25.1 (2018), p. 011602. DOI: 10.1063/1.5006700. eprint: https://doi.org/10.1063/1.5006700. URL: https://doi.org/10.1063/1.5006700.

[124] M. H. Anderson et al. "Observation of Bose-Einstein Condensation in a Dilute Atomic Vapor". In: *Science* 269.5221 (1995), pp. 198–201. ISSN: 0036-8075. DOI: 10.1126/science.269.5221.198. eprint: http://science.sciencemag.org/content/269/5221/198.full.pdf. URL: http://science.sciencemag.org/content/269/5221/198.

[125] K. B. Davis et al. "Bose-Einstein Condensation in a Gas of Sodium Atoms". In: *Phys. Rev. Lett.* 75 (22 1995), pp. 3969–3973. DOI: 10.1103/PhysRevLett.75.3969. URL: https://link.aps.org/doi/10.1103/PhysRevLett.75.3969.

[126] G. B. Andresen et al. "Evaporative Cooling of Antiprotons to Cryogenic Temperatures". In: *Phys. Rev. Lett.* 105 (2010), p. 013003. DOI: 10.1103/PhysRevLett.105.013003.

[127] G. Gabrielse et al. "Adiabatic Cooling of Antiprotons". In: *Phys. Rev. Lett.* 106 (7 Feb. 2011), p. 073002. DOI: 10.1103/PhysRevLett.106.073002. URL: https://link.aps.org/doi/10.1103/PhysRevLett.106.073002.

[128] S. A. Prasad and T. M. O'Neil. "Finite length thermal equilibria of a pure electron plasma column". In: *Phys. Fluids* 22 (1979), p. 278. DOI: doi:10.1063/1.862578.

[129] M. Ahmadi et al. "Antihydrogen accumulation for fundamental symmetry tests". In: *Nature Comm.* 8 (2017), p. 681. DOI: doi:10.1038/s41467-017-00760-9.

[130] C. Amole et al. "Resonant quantum transitions in trapped antihydrogen atoms". In: *Nature* 483 (2012), pp. 439–443. DOI: 10.1038/nature10942.

[131] W. A. Bertsche et al. "Antihydrogen formation by autoresonant excitation of antiproton plasmas". In: *Hyperfine Int.* 212 (2012), p. 61. DOI: 10.1007/s10751-011-383-8.

[132] Sabrina Shanman et al. "Improved Temperature Diagnostic for Non-Neutral Plasmas with Single-Electron Resolution". In: *APS DPP*. San Jose, California, 2016. URL: http://meetings.aps.org/link/BAPS.2016.DPP.JP10.38.

[133] Masaki Hori et al. "Two-photon laser spectroscopy of antiprotonic helium and the antiproton-to-electron mass ratio". In: *Nature* 475 (2011), pp. 484–488. DOI: 10.1038/nature10260.

[134] C. Amole et al. "Experimental limit on the charge of antihydrogen". In: *Nat. Commun.* 5 (2014), p. 3955. DOI: 10.1038/ncomms4955.

[135] M. S. Fee et al. "Measurement of the positronium $1\,^3S_1$–$2\,^3S_1$ interval by continuous-wave two-photon excitation". In: *Phys. Rev. A* 48 (1 1993), pp. 192–219. DOI: 10.1103/PhysRevA.48.192.

[136] John E. Nafe and Edward B. Nelson. "The Hyperfine Structure of Hydrogen and Deuterium". In: *Phys. Rev.* 73 (7 1948), pp. 718–728. DOI: 10.1103/PhysRev.73.718. URL: https://link.aps.org/doi/10.1103/PhysRev.73.718.

[137] Arthur Matveev et al. "Precision Measurement of the Hydrogen $1S-2S$ Frequency via a 920-km Fiber Link". In: *Phys. Rev. Lett.* 110 (23 2013), p. 230801. DOI: 10.1103/PhysRevLett.110.230801. URL: https://link.aps.org/doi/10.1103/PhysRevLett.110.230801.

[138] C Patrignani, Particle Data Group, et al. "Review of particle physics". In: *Chinese physics C* 40.10 (2016), p. 100001.

[139] Pauline Yzombard. "Laser cooling and manipulation of Antimatter in the AEgIS experiment". PhD thesis. L'Université Paris-Saclay, 2016.

[140] M. Bohman et al. "Sympathetic cooling of protons and antiprotons with a common endcap Penning trap". In: *Journal of Modern Optics* 65.5-6 (2018), pp. 568–576. DOI: 10.1080/09500340.2017.1404656.

[141] M. R. Natisin, J. R. Danielson, and C. M. Surko. "Sympathetically laser-cooled positrons". In: *Nuclear Instruments and Methods in Physics Research B* 192 (2002), pp. 117–127. DOI: https://doi.org/10.1016/S0168-583X(02)00791-7.

[142] Muhammed Sameed. "Laser-Ablated Beryllium Ions for Cold Antihydrogen in ALPHA". PhD thesis. Swansea University, 2017.